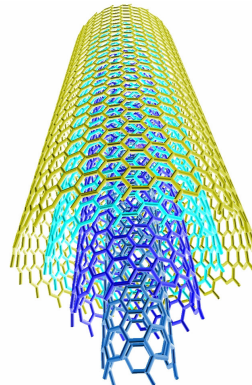


# The Wondrous World of Carbon Nanotubes

‘a review of current carbon nanotube technologies’



*27 February 2003*

The multidisciplinary project group consists of the following people:

M. Daenen (N)  
R.D. de Fouw (ST)  
B. Hamers (ST, Treasurer)  
P.G.A. Janssen (ST)  
K. Schouteden (N)  
M.A.J. Veld (ST, Project Manager)

Tutor:	X.E.E. Reynhout (TU/e)
Coordinator:	Dr. Ir. J.C. Reijenga (TU/e)
Client:	Prof. dr. P.H.L. Notten (Philips)
Advisor:	ir. R.A.H. Niessen (Philips)

# Project description

This report was written as interfaculty project, which was done for Phillips NAT-lab and had to be finished within ten weeks. The main goal of this project was to provide a detailed overview of current nanotube research. The main topics in which Phillips was interested were nanotube synthesis and purification, energy storage and other potential applications. A small limitation on the report was that it should not be too extensive, but comprehensible and convenient to read.

A group of students from the departments of 'Chemical Engineering and Chemistry' and 'Applied Physics' from the Eindhoven University of Technology did a literature search on these topics and this report is the result. All knowledge for the report is gained from articles of scientific magazines, books and the internet.

# Abstract

Since their discovery in 1991 by Iijima, carbon nanotubes have been of great interest, both from a fundamental point of view and for future applications. The most eye-catching features of these structures are their electronic, mechanical, optical and chemical characteristics, which open a way to future applications. These properties can even be measured on single nanotubes. For commercial application, large quantities of purified nanotubes are needed.

Different types of carbon nanotubes can be produced in various ways. The most common techniques used nowadays are: arc discharge, laser ablation, chemical vapour deposition and flame synthesis. Purification of the tubes can be divided into a couple of main techniques: oxidation, acid treatment, annealing, sonication, filtering and functionalisation techniques. Economically feasible large-scale production and purification techniques still have to be developed.

Fundamental and practical nanotube researches have shown possible applications in the fields of energy storage, molecular electronics, nanomechanic devices, and composite materials. Real applications are still under development.

This report provides an overview of current nanotube technology, with a special focus on synthesis and purification, energy storage in nanotubes and molecular electronics. Four types of energy storage known in carbon nanotubes are: electrochemical hydrogen storage, gas phase intercalation, electrochemical lithium storage and charge storage in supercapacitors. Modelling aspects and the characteristics of the storage are studied. CNTs have also proven to be good field emitters and single molecule transistors. The characteristics of and the production techniques for these devices are briefly presented.

# Table of contents

1.	Introduction .....	4
1.1	History of fullerenes .....	4
1.2	Carbon nanotube structure and defects .....	4
1.3	Special properties of carbon nanotubes .....	7
2.	Synthesis.....	8
2.1	Introduction .....	8
2.2	Growth mechanism.....	8
2.3	Arc discharge.....	9
2.3.1	Synthesis of SWNT .....	10
2.3.2	Synthesis of MWNT.....	12
2.4	Laser ablation .....	14
2.4.1	SWNT versus MWNT .....	14
2.4.2	Large scale synthesis of SWNT .....	15
2.4.3	Ultra fast Pulses from a free electron laser (FEL) method .....	15
2.4.4	Continuous wave laser-powder method .....	16
2.5	Chemical vapour deposition.....	17
2.5.1	Plasma enhanced chemical vapour deposition .....	17
2.5.2	Thermal chemical vapour deposition .....	18
2.5.3	Alcohol catalytic chemical vapour deposition.....	18
2.5.4	Vapour phase growth.....	19
2.5.5	Aero gel-supported chemical vapour deposition .....	19
2.5.6	Laser-assisted thermal chemical vapour deposition .....	20
2.5.7	CoMoCat process .....	20
2.5.8	High pressure CO disproportionation process.....	21
2.6	Flame synthesis .....	22
	Summary .....	23
3.	Purification .....	24
3.1	Introduction .....	24
3.2	Techniques .....	24
3.2.1	Oxidation.....	24
3.2.2	Acid treatment .....	25
3.2.3	Annealing .....	25
3.2.4	Ultrasonication .....	25
3.2.5	Magnetic Purification.....	25
3.2.6	Micro filtration .....	26
3.2.7	Cutting.....	27
3.2.8	Functionalisation .....	27
3.2.9	Chromatography.....	27
3.3	Conclusion.....	27
4.	Potential applications of CNTs.....	30
4.1	Energy storage.....	30
4.1.1	Hydrogen storage .....	30
4.1.2	Lithium intercalation .....	30
4.1.3	Electrochemical supercapacitors .....	30
4.2	Molecular electronics with CNTs.....	31
4.2.1	Field emitting devices .....	31
4.2.2	Transistors .....	31
4.3	Nanoprobes and sensors .....	31
4.4	Composite materials <sup>10</sup> .....	32
4.5	Templates <sup>10</sup> .....	33
5.	Energy storage .....	34
5.1	Electrochemical storage of hydrogen .....	34

5.1.1	Experimental studies .....	34
5.1.2	Modelling .....	38
5.2	Electrochemical storage of lithium.....	43
5.2.1	Experimental studies .....	43
5.2.2	Modelling <sup>97-98</sup> .....	45
5.3	Gas phase intercalation of hydrogen .....	51
5.3.1	Experimental studies .....	51
5.3.2	Modelling .....	53
5.4	Supercapacitors .....	57
5.4.1	Introduction .....	57
5.4.2	Basic principles of supercapacitors .....	57
5.4.3	Determination of supercapacitor properties .....	59
5.4.4	Modification of CNTs .....	59
6.	Determination of single nanotube properties .....	63
6.1	Catalytic growth on a support .....	63
6.2	Positioning by AFM techniques .....	64
6.3	Electronic property measurements of single SWNTs.....	65
6.4	Measuring charge transfer to single CNTs in electrolytes .....	66
6.5	Identification of single nanotubes by Raman spectroscopy .....	66
7.	Molecular electronics .....	67
7.1	Field Emitting Devices.....	67
7.1.1	Fabrication of CNT electron field emitters.....	67
7.1.2	Field emission from CNT films.....	68
7.1.3	Degradation of CNT films.....	72
7.1.4	Field emission from single CNTs.....	72
7.2	Transistors .....	72
7.2.1	Principles of the MOSFET and CNTFET .....	73
7.2.2	Manufacturing of a CNTFET .....	73
7.2.3	CNTFET physics .....	74
7.2.4	Switching mechanism of a MOSFET and CNTFET .....	75
7.2.5	Characteristics of a CNTFET .....	75
7.2.6	Optimisation of CNTFETs .....	75
7.2.7	Future outlook .....	76
7.3	Single electron transistor.....	76
7.3.1	Construction of SET on SWNT.....	76
7.3.2	Working mechanism of a SET .....	77
Appendix A:	List of abbreviations.....	79
Appendix B:	Overview of purification techniques .....	81
B.1	Method for purifying single wall carbon nanotubes <sup>54</sup> .....	81
B.2	Reduced diameter distribution of SWNTs by selective oxidation <sup>55</sup> .....	81
B.3	Plasma etching for purification and controlled opening of aligned carbon nanotubes <sup>56</sup> .....	82
B.4	Purification and characterisation of SWNTs <sup>57</sup> .....	82
B.5	Purification of SWNTs by selective microwave heating of catalyst particles <sup>58</sup> .....	83
B.6	Length sorting cut SWNTs by high performance liquid chromatography <sup>59</sup> .....	83
B.7	Purification of SWNTs synthesised by the hydrogen arc-discharge method <sup>60</sup> .....	84
B.8	High-quality SWNTs from arc-produced soot <sup>61</sup> .....	84
B.9	High-yield purification process of SWNTs <sup>62</sup> .....	84
B.10	Purification and characterisation of SWNTs obtained from the gas-phase decomposition of CO (HiPco process) <sup>63</sup> .....	85
B.11	Ultrasonic reflux system for one-step purification of carbon nanostructures <sup>64</sup> .....	85
B.12	Purification of SWNTs by microfiltration <sup>65</sup> .....	86
B.13	Purification of HiPco carbon nanotubes via organic functionalisation <sup>66</sup> .....	86
B.14	Purification of SWNTs by ultrasonically assisted filtration <sup>67</sup> .....	87
B.15	Mechanical purification of SWNT bundles from catalytic particles <sup>68</sup> .....	87
B.16	Cutting SWNTs by fluorination <sup>69</sup> .....	88

B.17	Enhanced saturation lithium composition in ball-milled single-walled carbon nanotubes <sup>70</sup>	88
B.18	Chromatographic purification of soluble SWNTs <sup>71</sup> .....	88
B.19	Chromatographic purification and properties of soluble SWNTs <sup>72</sup> .....	89

# 1. Introduction

## 1.1 History of fullerenes

Fullerenes are large, closed-cage, carbon clusters and have several special properties that were not found in any other compound before. Therefore, fullerenes in general form an interesting class of compounds that surely will be used in future technologies and applications. Before the first synthesis and detection of the smaller fullerenes  $C_{60}$  and  $C_{70}$ , it was generally accepted that these large spherical molecules were unstable. However, some Russian scientists<sup>1,2</sup> already had calculated that  $C_{60}$  in the gas phase was stable and had a relatively large band gap.

As is the case with numerous, important scientific discoveries, fullerenes were accidentally discovered. In 1985, Kroto and Smalley<sup>3</sup> found strange results in mass spectra of evaporated carbon samples. Herewith, fullerenes were discovered and their stability in the gas phase was proven. The search for other fullerenes had started.

Since their discovery in 1991 by Iijima and coworkers<sup>4</sup>, carbon nanotubes have been investigated by many researchers all over the world. Their large length (up to several microns) and small diameter (a few nanometres) result in a large aspect ratio. They can be seen as the nearly one-dimensional form of fullerenes. Therefore, these materials are expected to possess additional interesting electronic, mechanic and molecular properties. Especially in the beginning, all theoretical studies on carbon nanotubes focused on the influence of the nearly one-dimensional structure on molecular and electronic properties.

## 1.2 Carbon nanotube structure and defects

Many exotic structures of fullerenes exist: regular spheres, cones, tubes and also more complicated and strange shapes. Here we will describe some of the most important and best-known structures.

Single Walled Nanotubes (SWNT) can be considered as long wrapped graphene sheets. As stated before, nanotubes generally have a length to diameter ratio of about 1000 so they can be considered as nearly one-dimensional structures.

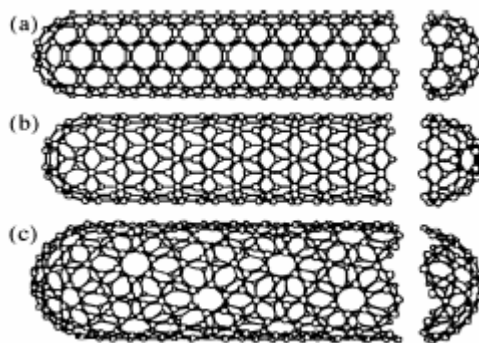


Figure 1-1: Some SWNTs with different chiralities. The difference in structure is easily shown at the open end of the tubes. a) armchair structure b) zigzag structure c) chiral structure

More detailed, a SWNT consists of two separate regions with different physical and chemical properties. The first is the sidewall of the tube and the second is the end cap of the tube. The end cap structure is similar to or derived from a smaller fullerene, such as  $C_{60}$ .

C-atoms placed in hexagons and pentagons form the end cap structures. It can be easily derived from Euler's theorem that twelve pentagons are needed in order to obtain a closed cage structure which

consists of only pentagons and hexagons.<sup>5</sup> The combination of a pentagon and five surrounding hexagons results in the desired curvature of the surface to enclose a volume. A second rule is the isolated pentagon rule that states that the distance between pentagons on the fullerene shell is maximised in order to obtain a minimal local curvature and surface stress, resulting in a more stable structure. The smallest stable structure that can be made this way is C<sub>60</sub> the one just larger is C<sub>70</sub> and so on. Another property is that all fullerenes are composed of an even number of C-atoms because adding one hexagon to an existing structure means adding two C-atoms.

The other structure of which a SWNT is composed is a cylinder. It is generated when a graphene sheet of a certain size that is wrapped in a certain direction. As the result is cylinder symmetric we can only roll in a discrete set of directions in order to form a closed cylinder. (Figure 1-2). Two atoms in the graphene sheet are chosen, one of which serves the role as origin. The sheet is rolled until the two atoms coincide. The vector pointing from the first atom towards the other is called the chiral vector and its length is equal to the circumference of the nanotube. (Figure 1-1) The direction of the nanotube axis is perpendicular to the chiral vector.

SWNTs with different chiral vectors have dissimilar properties such as optical activity, mechanical strength and electrical conductivity.

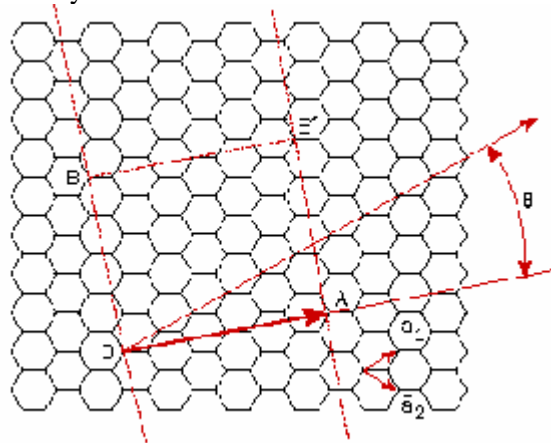


Figure 1-2: Vector  $OA$  is called the chiral vector. It can be defined by the vector  $C_n = na_1 + ma_2$  and the chiral angle with the zigzag axis. Vectors  $a_1$  and  $a_2$  are the lattice vectors.<sup>5</sup>

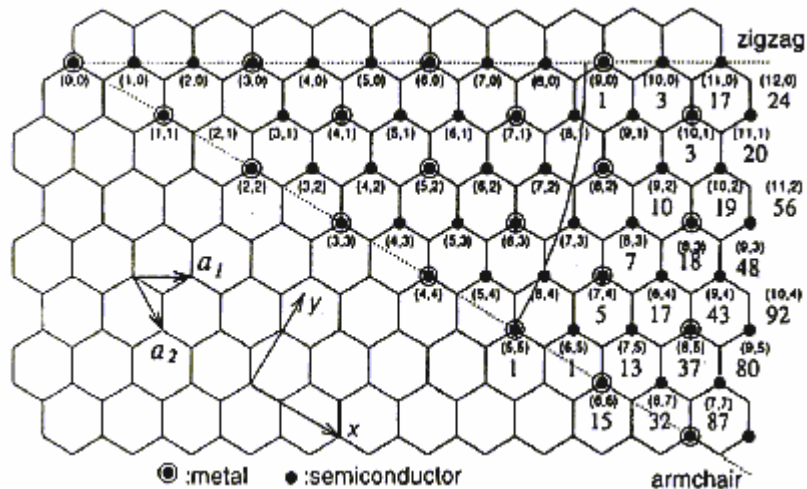


Figure 1-3: All possible structures of SWNTs can be formed from chiral vectors lying in the range given by this figure.  $(n, m)$  with  $n, m$  integer and  $m \leq n$  or  $\theta < 30^\circ$ .<sup>5</sup>

After ideal structures without flaws, we discuss the possible desirable or undesirable defects. Deformations, such as bends and nanotube junctions, are introduced by replacing a hexagon with a heptagon or pentagon. Deformations can be inward or outward and, among others, electrical properties are seriously changed by these deformations. Another class of defects is caused by impurities that are built in during or after the nanotube growth process; Compounds that can be incorporated into the structure are for example catalyst particles.

Multi Walled Nanotubes (MWNT) can be considered as a collection of concentric SWNTs with different diameters. The length and diameter of these structures differ a lot from those of SWNTs and, of course, their properties are also very different. (Figure 1-4)

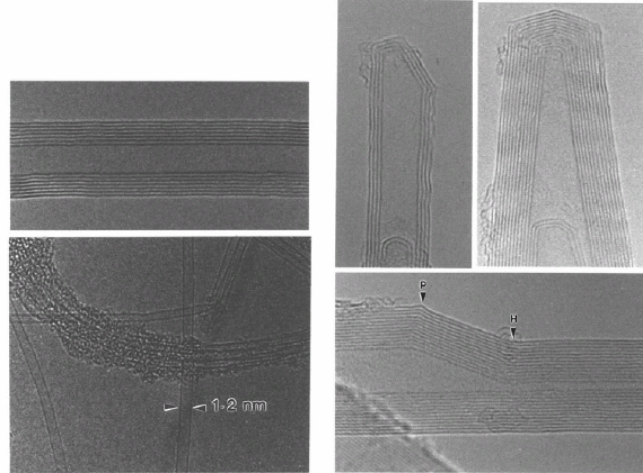


Figure 1-4: Different structures of MWNTs. Top-left: cross-section of a MWNT the different walls are obvious, they are separated by 0.34nm. Rotation around the symmetry axis gives us the MWNT. Top-right: Symmetrical or non-symmetrical cone shaped end caps of MWNTs. Bottom-left: A SWNT with a diameter of 1,2nm and a bundle of SWNTs covered with amorphous carbon. Bottom-right: A MWNT with defects. In point P a pentagon defect and in point H a heptagon defect.<sup>6</sup>

In Figure 1-4 carbon cones are also shown. It can be considered as a gradual transition from a large diameter to a smaller one without defects in the wall of the cone but with fewer pentagons in the end cap.

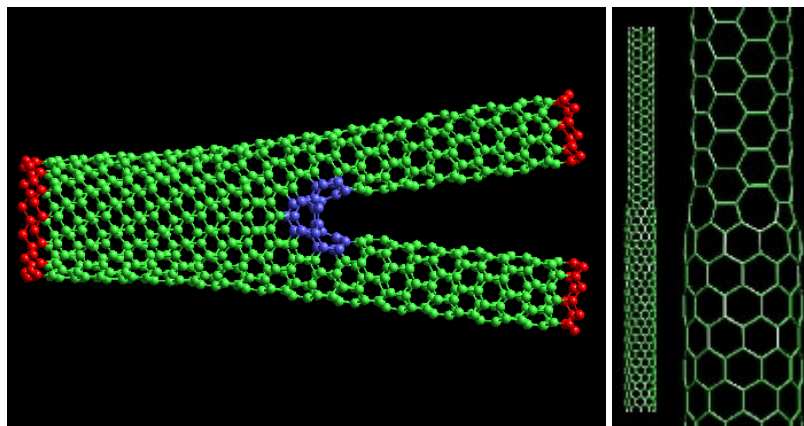


Figure 1-5: Left: A Y-branch, the defects are marked in blue. Right: A transition from a metallic to a semi-conducting SWNT. The change is made by insertion of pentagons and heptagons.

Introduction of defects can also result in various new structures such as Y-branches T-branches or SWNT junctions. (Figure 1-5) Under certain circumstances, these defects can be introduced in a ‘controlled’ way.

These defects result in special structures that will have other, but even more interesting, properties than their original forms. Defects are also being studied with great effort, but they will not be treated in this report.

A final type of interesting structures is the so-called peapods, carbon nanotubes with C<sub>60</sub> molecules enclosed in the nanotube.

### 1.3 Special properties of carbon nanotubes

Electronic, molecular and structural properties of carbon nanotubes are determined to a large extent by their nearly one dimensional structure. The most important properties of CNTs and their molecular background are stated below.

- **Chemical reactivity.**<sup>7</sup> The chemical reactivity of a CNT is, compared with a graphene sheet, enhanced as a direct result of the curvature of the CNT surface. Carbon nanotube reactivity is directly related to the pi-orbital mismatch caused by an increased curvature. Therefore, a distinction must be made between the sidewall and the end caps of a nanotube. For the same reason, a smaller nanotube diameter results in increased reactivity. Covalent chemical modification of either sidewalls or end caps has shown to be possible. For example, the solubility of CNTs in different solvents can be controlled this way. Though, direct investigation of chemical modifications on nanotube behaviour is difficult as the crude nanotube samples are still not pure enough.

- **Electrical conductivity.** Depending on their chiral vector, carbon nanotubes with a small diameter are either semi-conducting or metallic. The differences in conducting properties are caused by the molecular structure that results in a different band structure and thus a different band gap. The differences in conductivity can easily be derived from the graphene sheet properties.<sup>8</sup> It was shown that a  $(n,m)$  nanotube is metallic as accounts that:  $n=m$  or  $(n-m) = 3i$ , where  $i$  is an integer and  $n$  and  $m$  are defining the nanotube. The resistance to conduction is determined by quantum mechanical aspects and was proved to be independent of the nanotube length.<sup>9</sup> For more, general information on electron conductivity is referred to a review by Ajayan and Ebbesen<sup>10</sup>.

- **Optical activity.** Theoretical studies have revealed that the optical activity of chiral nanotubes disappears if the nanotubes become larger<sup>11</sup>. Therefore, it is expected that other physical properties are influenced by these parameters too. Use of the optical activity might result in optical devices in which CNTs play an important role.

- **Mechanical strength.** Carbon nanotubes have a very large Young modulus in their axial direction. The nanotube as a whole is very flexible because of the great length. Therefore, these compounds are potentially suitable for applications in composite materials that need anisotropic properties.

## 2. Synthesis

### 2.1 Introduction

In this section, different techniques for nanotube synthesis and their current status are briefly explained. First, the growth mechanism is explained, as it is almost general for all techniques. However, typical conditions are stated at the sections of all the different techniques. The largest interest is in the newest methods for each technique and the possibilities of scaling up.

Carbon nanotubes are generally produced by three main techniques, arc discharge, laser ablation and chemical vapour deposition. Though scientists are researching more economic ways to produce these structures. In arc discharge, a vapour is created by an arc discharge between two carbon electrodes with or without catalyst. Nanotubes self-assemble from the resulting carbon vapour. In the laser ablation technique, a high-power laser beam impinges on a volume of carbon –containing feedstock gas (methane or carbon monoxide). At the moment, laser ablation produces a small amount of clean nanotubes, whereas arc discharge methods generally produce large quantities of impure material. In general, chemical vapour deposition (CVD) results in MWNTs or poor quality SWNTs. The SWNTs produced with CVD have a large diameter range, which can be poorly controlled. But on the other hand, this method is very easy to scale up, what favours commercial production.

### 2.2 Growth mechanism

The way in which nanotubes are formed is not exactly known. The growth mechanism is still a subject of controversy, and more than one mechanism might be operative during the formation of CNTs. One of the mechanisms consists out of three steps. First a precursor to the formation of nanotubes and fullerenes,  $C_2$ , is formed on the surface of the metal catalyst particle. From this metastable carbide particle, a rodlike carbon is formed rapidly. Secondly there is a slow graphitisation of its wall. This mechanism is based on in-situ TEM observations<sup>12</sup>.

The exact atmospheric conditions depend on the technique used, later on, these will be explained for each technique as they are specific for a technique. The actual growth of the nanotube seems to be the same for all techniques mentioned.

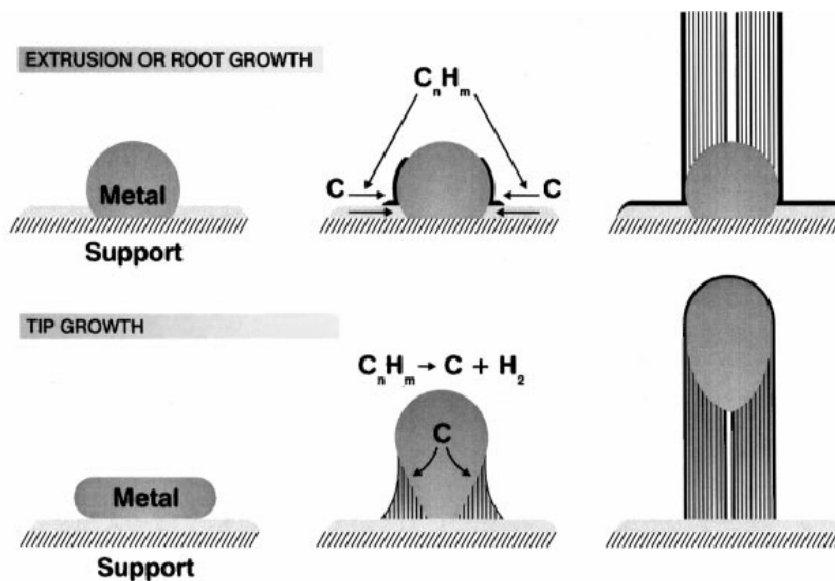


Figure 2-1: Visualisation of a possible carbon nanotube growth mechanism.

There are several theories on the exact growth mechanism for nanotubes. One theory<sup>13</sup> postulates that metal catalyst particles are floating or are supported on graphite or another substrate. It presumes that the catalyst particles are spherical or pear-shaped, in which case the deposition will take place on only one half of the surface (this is the lower curvature side for the pear shaped particles). The carbon diffuses along the concentration gradient and precipitates on the opposite half, around and below the bisecting diameter. However, it does not precipitate from the apex of the hemisphere, which accounts for the hollow core that is characteristic of these filaments. For supported metals, filaments can form either by 'extrusion (also known as base growth)' in which the nanotube grows upwards from the metal particles that remain attached to the substrate, or the particles detach and move at the head of the growing nanotube, labelled 'tip-growth'. Depending on the size of the catalyst particles, SWNT or MWNT are grown. In arc discharge, if no catalyst is present in the graphite, MWNT will be grown on the C<sub>2</sub>-particles that are formed in the plasma.

## 2.3 Arc discharge

The carbon arc discharge method, initially used for producing C<sub>60</sub> fullerenes, is the most common and perhaps easiest way to produce carbon nanotubes as it is rather simple to undertake. However, it is a technique that produces a mixture of components and requires separating nanotubes from the soot and the catalytic metals present in the crude product.

This method creates nanotubes through arc-vaporisation of two carbon rods placed end to end, separated by approximately 1mm, in an enclosure that is usually filled with inert gas (helium, argon) at low pressure (between 50 and 700 mbar). Recent investigations have shown that it is also possible to create nanotubes with the arc method in liquid nitrogen<sup>14</sup>. A direct current of 50 to 100 A driven by approximately 20 V creates a high temperature discharge between the two electrodes. The discharge vaporises one of the carbon rods and forms a small rod shaped deposit on the other rod. Producing nanotubes in high yield depends on the uniformity of the plasma arc and the temperature of the deposit form on the carbon electrode<sup>15</sup>.

Insight in the growth mechanism is increasing and measurements have shown that different diameter distributions have been found depending on the mixture of helium and argon. These mixtures have different diffusion coefficients and thermal conductivities. These properties affect the speed with which the carbon and catalyst molecules diffuse and cool, affecting nanotube diameter in the arc process. This implies that single-layer tubules nucleate and grow on metal particles in different sizes depending on the quenching rate in the plasma and it suggests that temperature and carbon and metal catalyst densities affect the diameter distribution of nanotubes<sup>15</sup>.

Depending on the exact technique, it is possible to selectively grow SWNTs or MWNTs, which is shown in Figure 2-2. Two distinct methods of synthesis can be performed with the arc discharge apparatus.

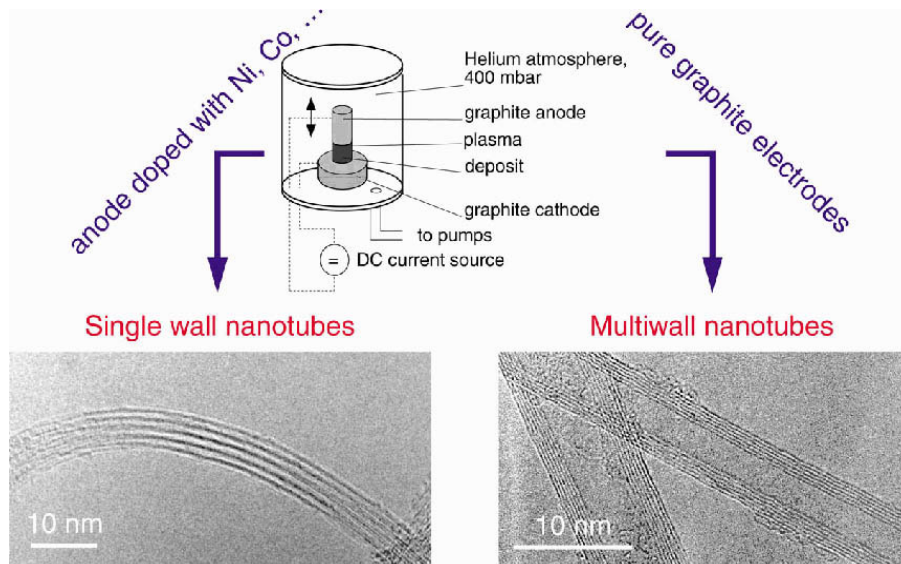


Figure 2-2: Experimental set-up of an arc discharge apparatus.

### 2.3.1 Synthesis of SWNT

If SWNTs are preferable, the anode has to be doped with metal catalyst, such as Fe, Co, Ni, Y or Mo. A lot of elements and mixtures of elements have been tested by various authors<sup>16</sup> and it is noted that the results vary a lot, even though they use the same elements. This is not surprising as experimental conditions differ. The quantity and quality of the nanotubes obtained depend on various parameters such as the metal concentration, inert gas pressure, kind of gas, the current and system geometry. Usually the diameter is in the range of 1.2 to 1.4 nm. A couple of ways to improve the process of arc discharge are stated below.

#### a) Inert gas

The most common problems with SWNT synthesis are that the product contains a lot of metal catalyst, SWNTs have defects and purification is hard to perform. On the other hand, an advantage is that the diameter can slightly be controlled by changing thermal transfer and diffusion, and hence condensation of atomic carbon and metals between the plasma and the vicinity of the cathode can control nanotube diameter in the arc process. This was shown in an experiment in which different mixtures of inert gases were used<sup>17</sup>.

It appeared that argon, with a lower thermal conductivity and diffusion coefficient, gave SWNTs with a smaller diameter of approximately 1.2 nm. A linear fit of the average nanotube diameter showed a 0.2 nm diameter decrease per 10 % increase in argon helium ratio, when nickel/yttrium was used (C/Ni/Y was 94.8:4.2:1) as catalyst.

#### b) Optical plasma control

A second way of control is plasma control by changing the anode to cathode distance (ACD). The ACD is adjusted in order to obtain strong visible vortices around the cathode. This enhances anode vaporisation, which improves nanotubes formation. Combined with controlling the argon-helium mixture, one can simultaneously control the macroscopic and microscopic parameters of the nanotubes formed<sup>18</sup>.

With a nickel and yttrium catalyst (C/Ni/Y is 94.8:4.2:1) the optimum nanotube yield was found at a pressure of 660 mbar for pure helium and 100 mbar for pure argon. The nanotube diameter ranges from 1.27 to 1.37 nanometre.

### c) Catalyst

Knowing that chemical vapour deposition (CVD) could give SWNTs with a diameter of 0.6–1.2 nm, researchers tried the same catalyst as used in CVD on arc discharge. Not all of the catalysts used appeared to result in nanotubes for both methods. But there seemed to be a correlation of diameter of SWNTs synthesised by CVD and arc discharge

As a result, the diameter can be controllably lowered to a range of 0.6-1.2 nm with arc-discharge. Using a mixture of Co and Mo in high concentrations as catalyst resulted in this result. These diameters are considerably smaller than 1.2-1.4 nm<sup>16</sup>, which is the usual size gained from arc-discharge.<sup>19</sup>

### d) Improvement of oxidation resistance

There is also progress in developing methods to improve the oxidation resistance of the SWNTs, which is a consequence of the defects present in nanotubes. A strong oxidation resistance is needed for the nanotubes if they have to be used for applications such as field emission displays. Recent research has indicated that a modified arc-discharge method using a bowl-like cathode (see Figure 2-3), decreases the defects and gives cleaner nanotubes, and thus improves the oxidation resistance<sup>20</sup>.

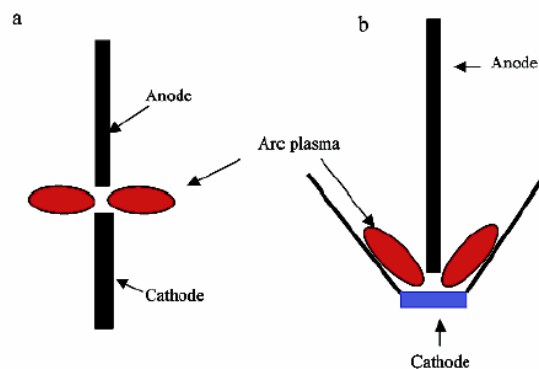


Figure 2-3: Schematic drawings of the electrode set-ups for (a) the conventional and (b) the new arc discharge electrodes.

The Raman spectrum of the newly synthesised nanotubes shows that the nanotubes formed are cleaner and less defective compared with those synthesised by conventional methods. The anode rod contained Ni and Y catalyst (C/Ni/Y is 94.8:4.2:1). No information is given about the diameter size.

### e) Open air synthesis with welding arc torch

Only a couple of years ago, researchers discovered that it was possible to form MWNTs in open air<sup>21</sup>. A welding arc torch was operated in open air and the process was shielded with an argon gas flow. The anode and cathode were made of graphite containing Ni and Y (Ni/Y is 4.2:1 at. %).

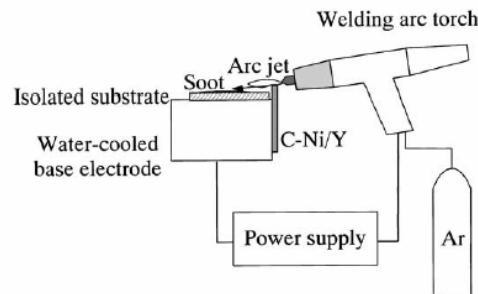


Figure 2-4: Experimental set-up of the torch arc method in open air.

This method was modified for preparing SWNTs<sup>22</sup>. A plate target made of graphite containing metal catalyst Ni and Y (Ni/Y is 3.6:0.8 at. per cent), was fixed at the sidewall of a water-cooled, steel based electrode. The torch arc aimed at the edge of the target and the soot was deposited on the substrate

behind the target (see Figure 2-4). The arc was operated at a direct current of 100 A. and shielding argon gas flowed through the torch, enhancing the arc jet formation beyond the target.

In the soot, carbon nanohorns (CNHs) and bundles of SWNT with an average diameter of 1.32 nm were found. However, the yield was much lower than for the conventional low-pressure arc discharge method. There are two reasons for this fact. At first, because of the open air, the lighter soot will escape into the atmosphere. Secondly, the carbon vapour might be oxidised and emitted as carbon dioxide gas. In order to improve the yield in this method, contrivances for collecting soot and development of an appropriate target are required.

This method promises to be convenient and inexpensive once the conditions for higher yield are optimised. With a Ni/Y catalyst (Ni/Y is 3.6:0.8), SWNT bundles and CNHs are formed. In this case the SWNTs have a diameter of approximately 1.32 nm<sup>22</sup>.

### 2.3.2 Synthesis of MWNT

If both electrodes are graphite, the main product will be MWNTs. But next to MWNTs a lot of side products are formed such as fullerenes, amorphous carbon, and some graphite sheets. Purifying the MWNTs, means loss of structure and disorders the walls. However scientist are developing ways to gain pure MWNTs in a large-scale process without purification.

Typical sizes for MWNTs are an inner diameter of 1-3 nm and an outer diameter of approximately 10 nm. Because no catalyst is involved in this process, there is no need for a heavy acidic purification step. This means, the MWNT, can be synthesised with a low amount of defects.

#### a) Synthesis in liquid nitrogen

A first, possibly economical route to highly crystalline MWNTs is the arc-discharge method in liquid nitrogen<sup>14</sup>, with this route mass production is also possible. For this option low pressures and expensive inert gasses are not needed.

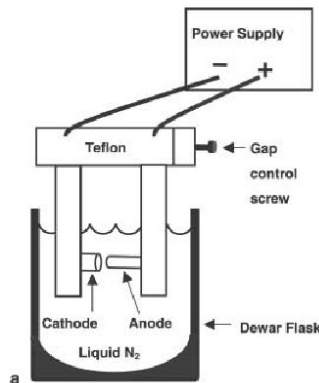


Figure 2-5: Schematic drawings of the arc discharge apparatus in liquid nitrogen.

The content of the MWNTs can be as high as 70 % of the reaction product. Analysis with Auger-spectroscopy revealed that no nitrogen was incorporated in the MWNTs. There is a strong possibility that SWNTs can be produced with the same apparatus under different conditions.

#### b) Magnetic field synthesis

Synthesis of MWNTs in a magnetic field<sup>23</sup> gives defect-free and high purity MWNTs that can be applied as nanosized electric wires for device fabrication. In this case, the arc discharge synthesis was controlled by a magnetic field around the arc plasma.

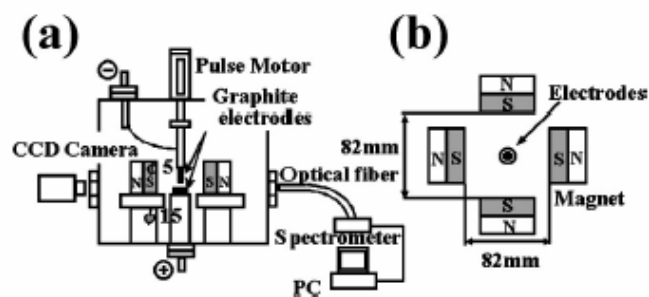


Figure 2-6: Schematic diagram of the synthesis system for MWNTs in a magnetic field.

Extremely pure graphite rods (purity > 99.999 %) were used as electrodes. Highly pure MWNTs (purity > 95 %) were obtained without further purification, which disorders walls of MWNTs.

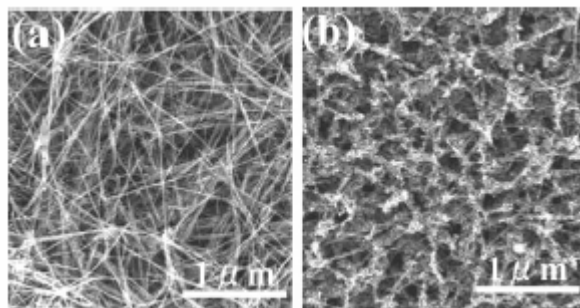


Figure 2-7: SEM images of MWNTs synthesised with (a) and without (b) the magnetic field.

### c) Plasma rotating arc discharge

A second possibly economical route to mass production of MWNTs is synthesis by plasma rotating arc discharge technique<sup>24</sup>. The centrifugal force caused by the rotation generates turbulence and accelerates the carbon vapour perpendicular to the anode. In addition, the rotation distributes the micro discharges uniformly and generates a stable plasma. Consequently, it increases the plasma volume and raises the plasma temperature.

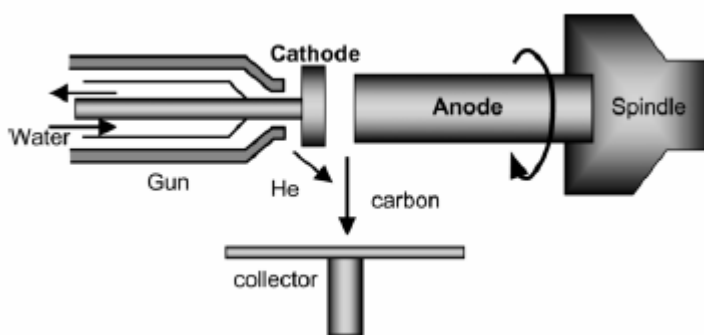


Figure 2-8: Schematic diagram of plasma rotating electrode system.

At a rotation speed of 5000 rpm a yield of 60 % was found at a formation temperature of 1025 °C without the use of a catalyst. The yield increases up to 90% after purification if the rotation speed is increased and the temperature is enlarged to 1150 °C. The diameter size was not mentioned in this publication.

## 2.4 Laser ablation

In 1995, Smalley's group<sup>25</sup> at Rice University reported the synthesis of carbon nanotubes by laser vaporisation. The laser vaporisation apparatus used by Smalley's group is shown in Figure 2-9. A pulsed<sup>26,27</sup>, or continuous<sup>28,29</sup> laser is used to vaporise a graphite target in an oven at 1200 °C. The main difference between continuous and pulsed laser, is that the pulsed laser demands a much higher light intensity (100 kW/cm<sup>2</sup> compared with 12 kW/cm<sup>2</sup>). The oven is filled with helium or argon gas in order to keep the pressure at 500 Torr. A very hot vapour plume forms, then expands and cools rapidly. As the vaporised species cool, small carbon molecules and atoms quickly condense to form larger clusters, possibly including fullerenes. The catalysts also begin to condense, but more slowly at first, and attach to carbon clusters and prevent their closing into cage structures.<sup>30</sup> Catalysts may even open cage structures when they attach to them. From these initial clusters, tubular molecules grow into single-wall carbon nanotubes until the catalyst particles become too large, or until conditions have cooled sufficiently that carbon no longer can diffuse through or over the surface of the catalyst particles. It is also possible that the particles become that much coated with a carbon layer that they cannot absorb more and the nanotube stops growing. The SWNTs formed in this case are bundled together by van der Waals forces<sup>30</sup>.

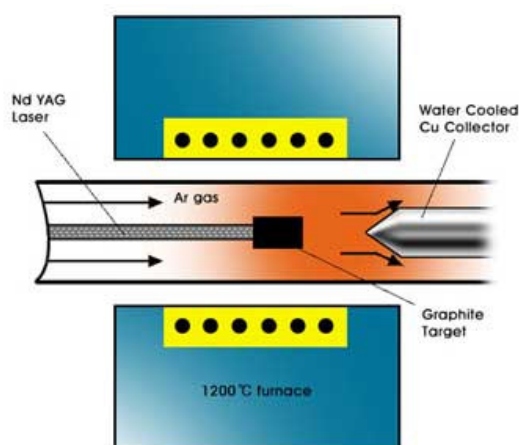


Figure 2-9: Schematic drawings of a laser ablation apparatus.

There are some striking, but not exact similarities, in the comparison of the spectral emission of excited species in laser ablation of a composite graphite target with that of laser-irradiated C<sub>60</sub> vapour. This suggests that fullerenes are also produced by laser ablation of catalyst-filled graphite, as is the case when no catalysts are included in the target. However, subsequent laser pulses excite fullerenes to emit C<sub>2</sub> that adsorbs on catalyst particles and feeds SWNT growth. However, there is insufficient evidence to conclude this with certainty<sup>30</sup>

Laser ablation is almost similar to arc discharge, since the optimum background gas and catalyst mix is the same as in the arc discharge process. This might be due to very similar reaction conditions needed, and the reactions probably occur with the same mechanism.

### 2.4.1 SWNT versus MWNT

The condensates obtained by laser ablation are contaminated with carbon nanotubes and carbon nanoparticles. In the case of pure graphite electrodes, MWNTs would be synthesised, but uniform SWNTs could be synthesised if a mixture of graphite with Co, Ni, Fe or Y was used instead of pure graphite. SWNTs synthesised this way exist as 'ropes', see Figure 2-10<sup>28,30</sup>. Laser vaporisation results in a higher yield for SWNT synthesis and the nanotubes have better properties and a narrower size distribution than SWNTs produced by arc-discharge.

Nanotubes produced by laser ablation are purer (up to about 90 % purity) than those produced in the arc discharge process. The Ni/Y mixture catalyst (Ni/Y is 4.2/1) gave the best yield.



Figure 2-10: TEM images of a bundle of SWNTs catalysed by Ni/Y (2:0.5 at. %) mixture, produced with a continuous laser.

The size of the SWNTs ranges from 1-2 nm, for example the Ni/Co catalyst with a pulsed laser at 1470 °C gives SWNTs with a diameter of 1.3-1.4 nm<sup>26</sup>. In case of a continuous laser at 1200 °C and Ni/Y catalyst (Ni/Y is 2:0.5 at. %), SWNTs with an average diameter of 1.4 nm were formed with 20-30 % yield, see Figure 2-10.<sup>28</sup>

## 2.4.2 Large scale synthesis of SWNT

Because of the good quality of nanotubes produced by this method, scientists are trying to scale up laser ablation. However the results are not yet as good as for the arc-discharge method, but they are still promising. In the next two sections, two of the newest developments on large-scale synthesis of SWNTs will be discussed. The first is the ‘ultra fast Pulses from a free electron laser<sup>27</sup>’ method, the second is ‘continuous wave laser-powder’ method<sup>29</sup>. Scaling up is possible, but the technique is rather expensive due to the laser and the large amount of power required.

## 2.4.3 Ultra fast Pulses from a free electron laser (FEL) method

Usually the pulses in an Nd:YAG system have width of approximately 10 ns, in this FEL system the pulse width is ~ 400 fs. The repetition rate of the pulse is enormously increased from 10 Hz to 75 MHz. To give the beam the same amount of energy as the pulse in an Nd:YAG system, the pulse has to be focused. The intensity of the laser bundle behind the lens reaches ~5 x 10<sup>11</sup> W/cm<sup>2</sup>, which is about 1000 times greater than in Nd:YAG systems.<sup>27</sup>

A jet of preheated (1000 °C) argon through a nozzle tip is situated close to the rotating graphite target, which contains the catalyst. The argon gas deflects the ablation plume approximately 90° away from the incident FEL beam direction, clearing away the carbon vapour from the region in front of the target. The produced SWNT soot, is collected in a cold finger. This process can be seen in Figure 2-11. The yield at this moment is 1,5 g/h, which is at 20 % of the maximum power of the not yet upgraded FEL. If the FEL is upgraded to full power and is working at 100 % power, a yield of 45 g/h could be reached since the yield was not limited by the laser power.

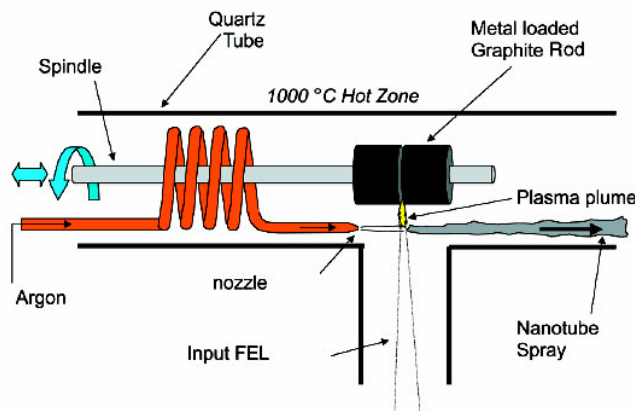


Figure 2-11: Schematic drawings of the ultra fast-pulsed laser ablation apparatus.

With this method the maximum achievable yield with the current lasers is 45 g/h, with a NiCo or NiY catalyst, in argon atmosphere at 1000 °C and a wavelength of ~3000 nm. The SWNTs produced in bundles of 8-200 nm and a length of 5-20 microns has a diameter range 1-1.4 nm.<sup>27</sup>

#### 2.4.4 Continuous wave laser-powder method

This method is a novel continuous, highly productive laser-powder method of SWNT synthesis based on the laser ablation of mixed graphite and metallic catalyst powders by a 2-kW continuous wave CO<sub>2</sub> laser in an argon or nitrogen stream. Because of the introduction of micron-size particle powders, thermal conductivity losses are significantly decreased compared with laser heating of the bulk solid targets in known laser techniques. As a result, more effective utilisation of the absorbed laser power for material evaporation was achieved. The set-up of the laser apparatus is shown in Figure 2-12<sup>29</sup>.

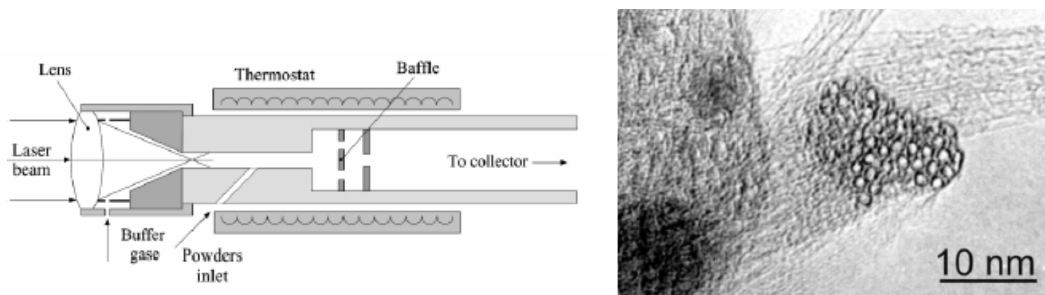


Figure 2-12: (Left) The principle scheme of the set-up for carbon SWNT production by continuous wave laser-powder method (Right) HRTEM of a SWNT-bundle cross-section.

The established yield of this technique was 5 g/h. A Ni/Co mixture (Ni/Co is 1:1) was used as catalyst, the temperature was 1100 °C. In the soot a SWNT abundance of 20-40% w as found with a mean diameter of 1.2-1.3 nm. An HRTEM-picture of this sample is shown in Figure 2-12.

## 2.5 Chemical vapour deposition

Chemical vapour deposition (CVD) synthesis is achieved by putting a carbon source in the gas phase and using an energy source, such as a plasma or a resistively heated coil, to transfer energy to a gaseous carbon molecule. Commonly used gaseous carbon sources include methane, carbon monoxide and acetylene. The energy source is used to “crack” the molecule into reactive atomic carbon. Then, the carbon diffuses towards the substrate, which is heated and coated with a catalyst (usually a first row transition metal such as Ni, Fe or Co) where it will bind. Carbon nanotubes will be formed if the proper parameters are maintained. Excellent alignment<sup>31</sup>, as well as positional control on nanometre scale<sup>32</sup>, can be achieved by using CVD. Control over the diameter, as well as the growth rate of the nanotubes can also be maintained. The appropriate metal catalyst can preferentially grow single rather than multi-walled nanotubes<sup>13</sup>.

CVD carbon nanotube synthesis is essentially a two-step process consisting of a catalyst preparation step followed by the actual synthesis of the nanotube. The catalyst is generally prepared by sputtering a transition metal onto a substrate and then using either chemical etching or thermal annealing to induce catalyst particle nucleation. Thermal annealing results in cluster formation on the substrate, from which the nanotubes will grow. Ammonia may be used as the etchant<sup>31,32,33,34</sup>. The temperatures for the synthesis of nanotubes by CVD are generally within the 650–900 °C range<sup>31,32,33,34</sup>. Typical yields for CVD are approximately 30%.

These are the basic principles of the CVD process. In the last decennia, different techniques for the carbon nanotubes synthesis with CVD have been developed, such as plasma enhanced CVD, thermal chemical CVD, alcohol catalytic CVD, vapour phase growth, aero gel-supported CVD and laser-assisted CVD. These different techniques will be explained more detailed in this chapter.

### 2.5.1 Plasma enhanced chemical vapour deposition

The plasma enhanced CVD method generates a glow discharge in a chamber or a reaction furnace by a high frequency voltage applied to both electrodes. Figure 2-13 shows a schematic diagram of a typical plasma CVD apparatus with a parallel plate electrode structure.

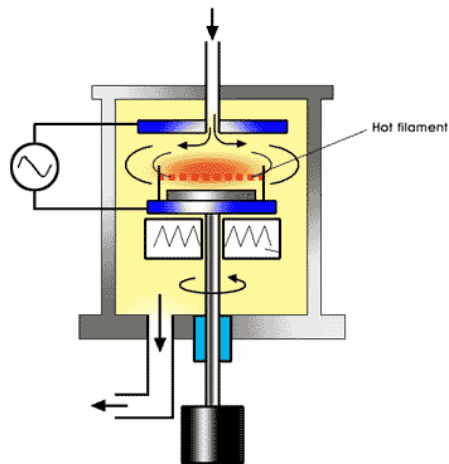


Figure 2-13: Schematic diagram of plasma CVD apparatus.

A substrate is placed on the grounded electrode. In order to form a uniform film, the reaction gas is supplied from the opposite plate. Catalytic metal, such as Fe, Ni and Co are used on for example a Si, SiO<sub>2</sub>, or glass substrate using thermal CVD or sputtering. After nanoscopic fine metal particles are formed, carbon nanotubes will be grown on the metal particles on the substrate by glow discharge generated from high frequency power. A carbon containing reaction gas, such as C<sub>2</sub>H<sub>2</sub>, CH<sub>4</sub>, C<sub>2</sub>H<sub>4</sub>, C<sub>2</sub>H<sub>6</sub>, CO is supplied to the chamber during the discharge<sup>35</sup>.

The catalyst has a strong effect on the nanotube diameter, growth rate, wall thickness, morphology and microstructure. Ni seems to be the most suitable pure-metal catalyst for the growth of aligned multi-walled carbon nanotubes (MWNTs)<sup>36</sup>. The diameter of the MWNTs is approximately 15 nm. The highest yield of carbon nanotubes achieved was about 50% and was obtained at relatively low temperatures (below 330° C)<sup>35</sup>.

### 2.5.2 Thermal chemical vapour deposition

In this method Fe, Ni, Co or an alloy of the three catalytic metals is initially deposited on a substrate. After the substrate is etched in a diluted HF solution with distilled water, the specimen is placed in a quartz boat. The boat is positioned in a CVD reaction furnace, and nanometre-sized catalytic metal particles are formed after an additional etching of the catalytic metal film using NH<sub>3</sub> gas at a temperature of 750 to 1050° C. As carbon nanotubes are grown on these fine catalytic metal particles in CVD synthesis, forming these fine catalytic metal particles is the most important process. Figure 2-14 shows a schematic diagram of thermal CVD apparatus in the synthesis of carbon nanotubes.

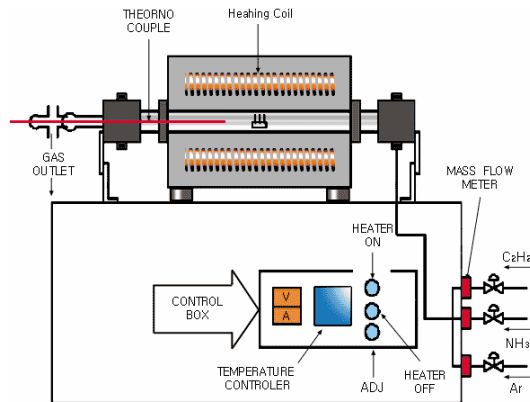


Figure 2-14: Schematic diagram of thermal CVD apparatus.

When growing carbon nanotubes on a Fe catalytic film by thermal CVD, the diameter range of the carbon nanotubes depends on the thickness of the catalytic film. By using a thickness of 13 nm, the diameter distribution lies between 30 and 40 nm. When a thickness of 27 nm is used, the diameter range is between 100 and 200 nm. The carbon nanotubes formed are multiwalled<sup>37</sup>.

### 2.5.3 Alcohol catalytic chemical vapour deposition

Alcohol catalytic CVD (ACCVD) is a technique that is being intensively developed for the possibility of large-scale production of high quality single wall nanotubes SWNTs at low cost. In this technique, evaporated alcohols, methanol and ethanol, are being utilised over iron and cobalt catalytic metal particles supported with zeolite. Generation is possible at a relatively low minimum temperature of about 550 °C. It seems that hydroxyl radicals, who come from reacting alcohol on catalytic metal particles, remove carbon atoms with dangling bonds, which are obstacles in creating high-purity SWNTs. The diameter of the SWNTs is about 1 nm. Figure 2-15 shows the ACCVD experimental apparatus.

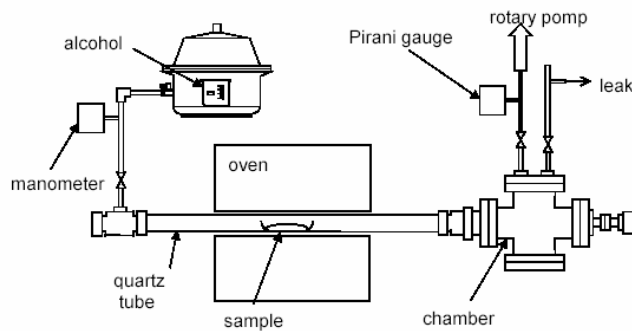


Figure 2-15: ACCVD experimental apparatus<sup>38</sup>.

The lower reaction temperature and the high-purity features of this ACCVD technique guarantee an easy possibility to scale production up at low cost. Furthermore, the reaction temperature, which is lower than 600 °C, ensures that this technique is easily applicable for the direct growth of SWNTs on semiconductor devices already patterned with aluminium<sup>38</sup>.

## 2.5.4 Vapour phase growth

Vapour phase growth is a synthesis method of carbon nanotubes, directly supplying reaction gas and catalytic metal in the chamber without a substrate<sup>39</sup>.<sup>39</sup>

Figure 2-16 shows a schematic diagram of a vapour phase growth apparatus. Two furnaces are placed in the reaction chamber. Ferrocene is used as catalyst. In the first furnace, vaporisation of catalytic carbon is maintained at a relatively low temperature. Fine catalytic particles are formed and when they reach the second furnace, decomposed carbons are absorbed and diffused to the catalytic metal particles. Here, they are synthesised as carbon nanotubes. The diameter of the carbon nanotubes by using vapour phase growth are in the range of 2 – 4 nm for SWNTs<sup>40</sup> and between 70 and 100 nm for MWNTs.<sup>39</sup>

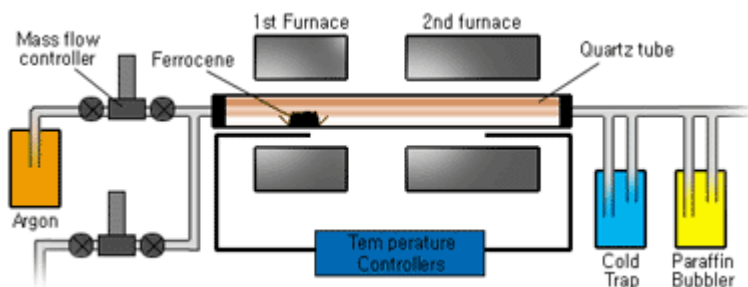


Figure 2-16: Schematic diagram of a vapour phase growth apparatus.<sup>39</sup>

## 2.5.5 Aero gel-supported chemical vapour deposition

In this method SWNTs are synthesised by disintegration of carbon monoxide on an aero gel-supported Fe/Mo catalyst. There are many important factors that affect the yield and quality of SWNTs, including the surface area of the supporting material, reaction temperature and feeding gas. Because of the high surface area, the porosity and ultra-light density of the aero gels, the productivity of the catalyst is much higher than in other methods<sup>41</sup>. After a simple acidic treatment and a oxidation process high purity (>99%) SWNTs can be obtained.

When using CO as feeding gas the yield of the nanotubes is lower but the overall purity of the materials is very good. The diameter distribution of de nanotubes is between 1,0 nm and 1,5 nm. The optimal reaction temperature is approximately 860 °C<sup>42</sup>.

## 2.5.6 Laser-assisted thermal chemical vapour deposition

In laser-assisted thermal CVD (LCVD) a medium power, continuous wave CO<sub>2</sub> laser, which was perpendicularly directed onto a substrate, pyrolyses sensitised mixtures of Fe(CO)<sub>5</sub> vapour and acetylene in a flow reactor. The carbon nanotubes are formed by the catalysing action of the very small iron particles. Figure 2-17 shows the experimental set-up for laser-assisted CVD<sup>43</sup>.

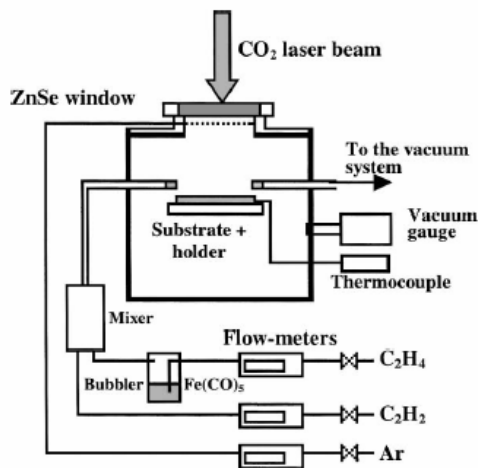


Figure 2-17: Experimental set-up for laser-assisted CVD<sup>43</sup>.

By using a reactant gas mixture of iron pentacarbonyl vapour, ethylene and acetylene both single- and multi-walled carbon nanotubes are produced. Silica is used as substrate. The diameters of the SWNTs range from 0.7 to 2.5 nm. The diameter range of the MWNTs is 30 to 80 nm<sup>43</sup>.

## 2.5.7 CoMoCat process

In this method, SWNTs are grown by CO disproportionation at 700 – 950 °C. The technique is based on a unique Co-Mo catalyst formulation that inhibits the sintering of Co particles and therefore inhibits the formation of undesired forms of carbon that lower the selectivity. During the SWNT reaction, cobalt is progressively reduced from the oxidic state to the metallic form. Simultaneously Molybdenum is converted to the carbidic form (Mo<sub>2</sub>C). Co acts as the active species in the activation of CO, while the role of the Mo is possibly dual. It would stabilise Co as a well-dispersed Co<sup>2+</sup> avoiding its reduction and would act as a carbon sink to moderate the growth of carbon inhibiting the formation of undesirable forms of carbon<sup>44</sup>.

It is found that one of the critical conditions for an effective reactor operation is that the space velocity has to be high enough to keep the CO conversion as low as possible. Figure 2-18 shows a fluidised bed reactor for a CoMoCat process. The most important advantage of fluidised bed reactors is that they permit continuous addition and removal of solid particles from the reactor, without stopping the operation.

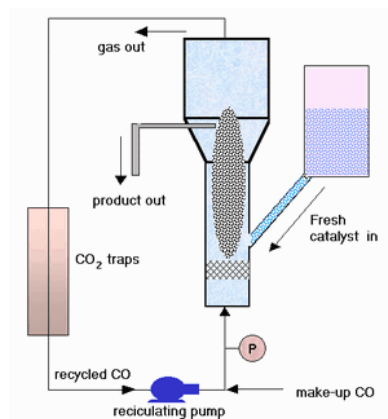


Figure 2-18: Schematic diagram of a CoMoCat apparatus

This method can be scaled-up without losses in SWNT quality. By varying the operation conditions, SWNTs can be produced with different diameter ranges.

In Table 2-1 several diameter ranges at different temperatures are given.<sup>45</sup>

<i>Temperature ( °C)</i>	<i>Diameter range</i>
750	0,9 ± 0,05
850	0,9 – 1,25
950	1,00 – 1,40

Table 2-1: Diameter range versus temperature

The CoMoCat catalyst has a high selectivity towards SWNTs, namely 80 – 90 %<sup>46</sup>.

## 2.5.8 High pressure CO disproportionation process

The High pressure CO disproportionation process (HiPco) is a technique for catalytic production of SWNTs in a continuous-flow gas phase using CO as the carbon feedstock and Fe(CO)<sub>5</sub> as the iron-containing catalyst precursor. SWNTs are produced by flowing CO, mixed with a small amount of Fe(CO)<sub>5</sub> through a heated reactor. Figure 2-19 shows the layout of CO flow-tube reactor. Size and diameter distribution of the nanotubes can be roughly selected by controlling the pressure of CO. This process is promising for bulk production of carbon nanotubes.

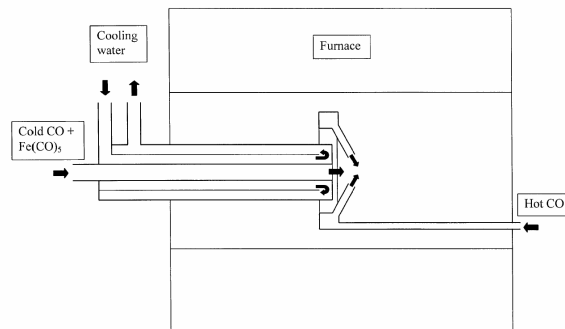


Figure 2-19: Layout of CO flow-tube reactor<sup>47</sup>.

Nanotubes as small as 0.7 nm in diameter, which are expected to be the smallest achievable chemically stable SWNTs<sup>48</sup>, have been produced by this method. The average diameter of HiPco SWNTs is approximately 1.1 nm. The yield that could be achieved is approximately 70%. The highest yields and narrowest tubes can be produced at the highest accessible temperature and pressure<sup>47</sup>. SWNT material with 97% purity can be produced at rates of up to 450 mg/h with this process<sup>49</sup>.

## 2.6 Flame synthesis

This method is based on the synthesis of SWNTs in a controlled flame environment, that produces the temperature, forms the carbon atoms from the inexpensive hydrocarbon fuels and forms small aerosol metal catalyst islands<sup>50,51,52</sup>. SWNTs are grown on these metal islands in the same manner as in laser ablation and arc discharge.

These metal catalyst islands can be made in three ways. The metal catalyst (cobalt) can either be coated on a mesh<sup>50</sup>, on which metal islands resembling droplets were formed by physical vapour deposition. These small islands become aerosol after exposure to a flame. The second way<sup>52</sup>, is to create aerosol small metal particles by burning a filter paper that is rinsed with a metal-ion (e.g. iron nitrate) solution. The third way, is the thermal evaporating technique in which metal powder (e.g. Fe or Ni) is inserted in a trough and heated<sup>51</sup>.

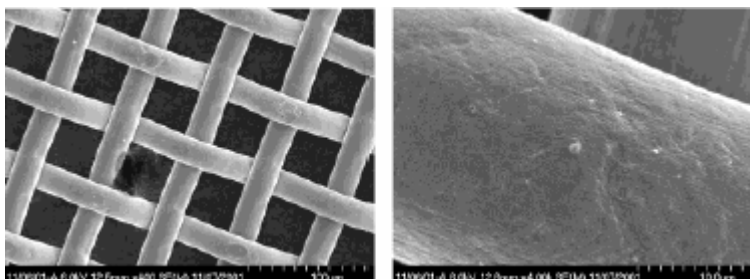


*Figure 1.1 Meshes on which the metal catalyst is coated, used in flame synthesis*

In a controlled way a fuel gas is partially burned to gain the right temperature of  $\sim 800$  °C and the carbon atoms for SWNT production. On the small metal particles the SWNTs are then formed. As optimisation parameters the fuel gas composition, catalyst, catalyst carrier surface and temperature can be controlled<sup>50</sup>. In the literature found, the yield, typical length and diameters are not stated.

## Summary

In Table 2-2, a short summary of the three most common techniques used nowadays is given.

Method	Arc discharge method	Chemical vapour deposition	Laser ablation (vaporization)
Who	Ebbesen and Ajayan, NEC, Japan 1992 <sup>15</sup>	Endo, Shinshu University, Nagano, Japan <sup>53</sup>	Smalley, Rice, 1995 <sup>14</sup>
How	Connect two graphite rods to a power supply, place them a few millimetres apart, and throw the switch. At 100 amps, carbon vaporises and forms a hot plasma.	Place substrate in oven, heat to 600 °C, and slowly add a carbon-bearing gas such as methane. As gas decomposes it frees up carbon atoms, which recombine in the form of NTs	Blast graphite with intense laser pulses; use the laser pulses rather than electricity to generate carbon gas from which the NTs form; try various conditions until hit on one that produces prodigious amounts of SWNTs
Typical yield	30 to 90%	20 to 100 %	Up to 70%
SWNT	Short tubes with diameters of 0.6 - 1.4 nm	Long tubes with diameters ranging from 0.6-4 nm	Long bundles of tubes (5-20 microns), with individual diameter from 1-2 nm.
MWNT	Short tubes with inner diameter of 1-3 nm and outer diameter of approximately 10 nm	Long tubes with diameter ranging from 10-240 nm	Not very much interest in this technique, as it is too expensive, but MWNT synthesis is possible.
Pro	Can easily produce SWNT, MWNTs. SWNTs have few structural defects; MWNTs without catalyst, not too expensive, open air synthesis possible	Easiest to scale up to industrial production; long length, simple process, SWNT diameter controllable, quite pure	Primarily SWNTs, with good diameter control and few defects. The reaction product is quite pure.
Con	Tubes tend to be short with random sizes and directions; often needs a lot of purification	NTs are usually MWNTs and often riddled with defects	Costly technique, because it requires expensive lasers and high power requirement, but is improving

Table 2-2: A summary of the major production methods and their efficiency

## 3. Purification

### 3.1 Introduction

A large problem with nanotube application is next to large-scale synthesis also the purification. In this chapter the purification of SWNTs will be discussed. The as-produced SWNT soot contains a lot of impurities. The main impurities in the soot are graphite (wrapped up) sheets, amorphous carbon, metal catalyst and the smaller fullerenes. These impurities will interfere with most of the desired properties of the SWNTs. Also in the fundamental research, it is preferred to obtain SWNTs or the impurities, as pure as possible without changing them. In order to understand the measurements better, the SWNT samples also have to be as homogeneous as possible. The common industrial techniques use strong oxidation and acid refluxing techniques, which have an effect on the structure of the tubes.

In this chapter several purification techniques of the SWNT will be discussed. Basically, these techniques can be divided into two mainstreams, structure selective and size selective separations. The first one will separate the SWNTs from the impurities; the second one will give a more homogeneous diameter or size distribution. The techniques will be briefly explained in this chapter and if possible, the selectivity will be discussed. The techniques that will be discussed are oxidation, acid treatment, annealing, ultrasonication, micro filtration, ferromagnetic separation, cutting, functionalisation and chromatography techniques.

Because most of the techniques used, are combined with other techniques, the purification methods, as mentioned in the references, will be summarised in chronological order. A short summary of these references used can be found in Appendix B.

At the end of this chapter, an overview-table Table 3-1 will be given of the most important characteristics of the techniques stated in this report. With this table, it should be easy to see what procedures must be chosen in order to gain the wanted grade of SWNTs and the consequences of the technique on the sample.

### 3.2 Techniques

#### 3.2.1 Oxidation

Oxidative treatment of the SWNTs is a good way to remove carbonaceous impurities<sup>54,55,56,57,58,59</sup> or to clear the metal surface<sup>54,57,60,61,62,63,58</sup>. The main disadvantages of oxidation are that not only the impurities are oxidised, but also the SWNTs. Luckily the damage to SWNTs is less than the damage to the impurities. These impurities have relatively more defects or a more open structure. Another reason why impurity oxidation is preferred, is that these impurities are most commonly attached to the metal catalyst, which also acts as oxidising catalyst<sup>54,64,55,60,57</sup>. Altogether, the efficiency and the yield of the procedure are highly dependable on a lot of factors, such as metal content, oxidation time, environment, oxidising agent and temperature.

The fact that metal acts as oxidising catalyst, the metal content should certainly be taken into consideration, when looking at the oxidising time. For example, when the temperature is raised above 600 °C, SWNTs will also oxidise, even without catalyst<sup>60</sup>. This is the case with thermal<sup>54</sup>, fixed air<sup>57,60,61,62</sup> and pure oxygen oxidations<sup>56,55,57</sup>. These can easily oxidise all the components, so the temperature and the time should be in good control.

There are a couple of examples for clearing the metal surface, to prepare the sample for a metal removal step. The first one is (mild) oxidising in a wet environment with soluble oxidising agents, such as  $\text{H}_2\text{O}_2$  and  $\text{H}_2\text{SO}_4$ <sup>59</sup>. These will only oxidise the defects and will clear the surface of the metal.

Most commonly, the metal catalyst stays intact during these processes, but when oxygen is used in a wet atmosphere, the outer layer of the metal will be oxidised<sup>63</sup>. Then, the density of this surface increases and the surface covering carbon layer ruptures. Not only the carbon impurities are oxidised now, but also the metal is partially oxidised and exposed.

Quite different from the oxidative techniques above is microwave heating. The microwaves will heat up the metal and will catalytically oxidise the carbon attached to the metal.

### **3.2.2 Acid treatment**

In general the acid treatment will remove the metal catalyst. First of all, the surface of the metal must be exposed by oxidation or sonication. The metal catalyst is then exposed to acid and solvated. The SWNTs remain in suspended form. When using a treatment in  $\text{HNO}_3$ , the acid only has an effect on the metal catalyst. It has no effect on the SWNTs and other carbon particles<sup>54,55,61,59</sup>. If a treatment in  $\text{HCl}$  is used, the acid has also a little effect on the SWNTs and other carbon particles<sup>54,57,62,63</sup>. The mild acid treatment<sup>65</sup> (4 M  $\text{HCl}$  reflux) is basically the same as the  $\text{HNO}_3$  reflux, but here the metal has to be totally exposed to the acid to solvate it.

### **3.2.3 Annealing**

Due to high temperatures (873 – 1873 K) the nanotubes will be rearranged and defects will be consumed<sup>55,57,63,66</sup>. The high temperature also causes the graphitic carbon and the short fullerenes to pyrolyse. When using high temperature vacuum treatment<sup>61</sup> (1873 K) the metal will be melted and can also be removed.

### **3.2.4 Ultrasonication**

In this technique particles are separated due to ultrasonic vibrations. Agglomerates of different nanoparticles will be forced to vibrate and will become more dispersed. The separation of the particles is highly dependable on the surfactant, solvent and reagent used.

The solvent influences the stability of the dispersed tubes in the system. In poor solvents the SWNTs are more stable if they are still attached to the metal. But in some solvents, such as alcohols, mono-dispersed particles are relatively stable<sup>54,60,64,65,67</sup>.

When an acid is used, the purity of the SWNTs depends on the exposure time. When the tubes are exposed to the acid for a short time, only the metal solvates, but for a longer exposure time, the tubes will also be chemically cut<sup>63,57,59</sup>.

### **3.2.5 Magnetic Purification**

In this method ferromagnetic (catalytic) particles are mechanically removed from their graphitic shells<sup>68</sup>. The SWNTs suspension is mixed with inorganic nanoparticles (mainly  $\text{ZrO}_2$  or  $\text{CaCO}_3$ ) in an ultrasonic bath to remove the ferromagnetic particles. Then, the particles are trapped with permanent magnetic poles. After a subsequent chemical treatment, a high purity SWNT material will be obtained. Figure 3-1 shows a schematic diagram of the apparatus for magnetic purification<sup>68</sup>.

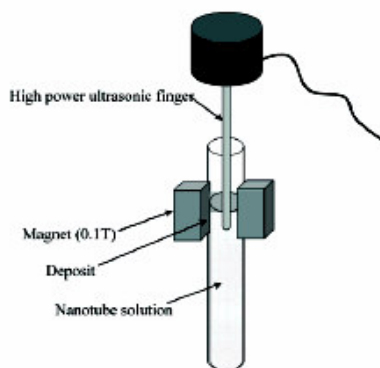


Figure 3-1: Schematic diagram of the apparatus for magnetic purification <sup>68</sup>.

This process does not require large equipment and enables the production of laboratory-sized quantities of SWNTs containing no magnetic impurities.

### 3.2.6 Micro filtration

Micro filtration is based on size or particle separation. SWNTs and a small amount of carbon nanoparticles are trapped in a filter. The other nanoparticles (catalyst metal, fullerenes and carbon nanoparticles) are passing through the filter. Figure 3-2 shows a schematic diagram of a micro filtration cell <sup>55,63,64,65,67,62</sup>.

One way of separating fullerenes from the SWNTs by micro filtration is to soak the as-produced SWNTs first in a CS<sub>2</sub> solution. The CS<sub>2</sub> insolubles are then trapped in a filter. The fullerenes which are solvated in the CS<sub>2</sub>, pass through the filter <sup>65</sup>.

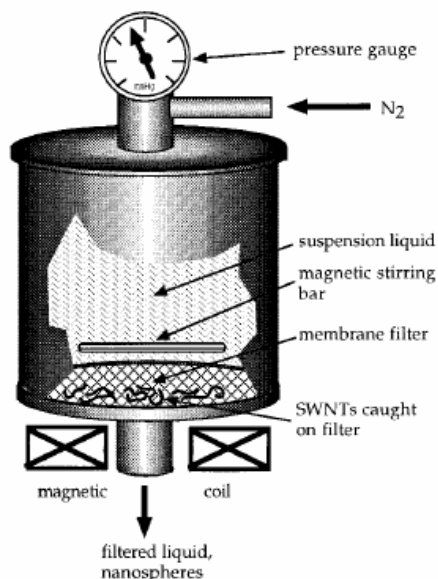


Figure 3-2: Schematic diagram of a micro filtration cell <sup>65</sup>.

A special form of filtration is cross flow filtration. In cross flow filtration the membrane is a hollow fibre. The membrane is permeable to the solution. The filtrate is pumped down the bore of the fibre at some head pressure from a reservoir and the major fraction of the fast flowing solution which does not permeate out the sides of the fibre is fed back into the same reservoir to be cycled through the fibre repeatedly. A fast hydrodynamic flow down the fibre bore (cross flow) sweeps the membrane surface preventing the build-up of a filter cake <sup>55,59</sup>.

### **3.2.7 Cutting**

Cutting of the SWNTs can either be induced chemically<sup>69</sup>, mechanically<sup>70</sup> or as a combination of these<sup>59</sup>.

SWNTs can be chemically cut by partially functionalising the tubes, for example with fluor<sup>69</sup>. Then, the fluorated carbon will be driven off the sidewall with pyrolysis in the form of CF<sub>4</sub> or COF<sub>2</sub>. This will leave behind the chemically cut nanotubes.

Mechanical<sup>70</sup> cutting of the nanotubes can be induced by ball-milling. Here, the bonds will break due to the high friction between the nanoparticles and the nanotubes will be disordered.

A combination of mechanical and chemical cutting of the nanotubes<sup>59</sup>, is ultrasonic induced cutting in an acid solution. In this way the ultrasonic vibration will give the nanotubes sufficient energy to leave the catalyst surface. Then, in combination with acid the nanotubes will rupture at the defect sites.

### **3.2.8 Functionalisation**

Functionalisation is based on making SWNTs more soluble than the impurities by attaching other groups to the tubes. Now it is easy to separate them from insoluble impurities, such as metal, with filtration<sup>71,72</sup>.

Another functionalisation technique also leaves the SWNT structure intact and makes them soluble for chromatographic size separation<sup>66</sup>.

For recovery of the purified SWNTs, the functional groups can be simply removed by thermal treatment, such as annealing.

### **3.2.9 Chromatography**

This technique is mainly used to separate small quantities of SWNTs into fractions with small length and diameter distribution. The SWNTs are run over a column with a porous material, through which the SWNTs will flow. The columns used are GPC (Gel Permeation Chromatography) and HPLC-SEC (High Performance Liquid Chromatography - Size Exclusion Chromatography) columns. The number of pores the SWNTs will flow through, depends on their size. This means that, the smaller the molecule, the longer the pathway to the end of the column will be and that the larger molecules will come off first. The pore size will control what size distribution can be separated. However, a problem is that the SWNTs have to be either dispersed<sup>59</sup> or solvated<sup>71,72</sup>. This can be done by ultrasonication<sup>59</sup> or functionalisation with soluble groups<sup>71,72</sup>.

## **3.3 Conclusion**

With the different techniques for purification as described above, there will be different results achieved. Care should be taken when the technique is chosen, as the effect on the entire sample will also depend on the composition and the amount of the sample. What is desired are techniques that only tear down the carbon impurities and the metals, without changing the nanotubes. But only few techniques are capable of this. Most techniques have a (sometimes devastating) influence on the SWNTs, such as cutting the SWNTs or oxidation reactions. Here extra care should be taken in adjusting the process variables such as temperature, scale and time. Table 3-1 on the next page, shows several techniques used in purification. How the techniques effect the SWNTs and other particles, is stated in this table. Also given is how these techniques effect the yield and purity.

<i>Technique</i>	SWNT	<i>Carbon particles, graphite</i>	<i>Short fullerenes C<sub>60</sub>, C<sub>70</sub>, etc</i>	<i>Metal catalyst</i>	<i>Yield</i>	<i>Purity</i>	<i>Short description of the technique and literature</i>
Thermal Oxidation	0	-	-	+	No Record	No Record	Heating from 350 – 600 °C. Metal is used as oxidation catalyst.  Ref: <sup>54</sup>
Wet Oxidation (H <sub>2</sub> O <sub>2</sub> )	0	0	0	+	No Record	No Record	Reflux in hydrogen peroxide. Process makes it easier to remove metal catalyst  Ref: <sup>54</sup>
Pure Oxygen Oxidation (Size Selective)	-	-	-	+	Poor	Very few carbon impurities	Preferentially burns SWNT with smaller diameter. P = 1,5 – 5 · 10 <sup>-6</sup> mbar; T = 723 – 873 K  Ref: <sup>56,55,57</sup>
Fixed Air Oxidation	0	-	-	+	Good	Very few carbon impurities	The metal catalyst will be exposed. Process makes it easier to remove metal catalyst  Ref: <sup>57,60,61,62</sup>
Wet Air Oxidation (HiPco)	0	-	-	+	Good	Very few carbon impurities, metal exposed	Air bubbled through water oxidises and exposes the metal.  Ref: <sup>63</sup>
Microwave Treatment	0	-	-	-	Very good	Very few carbon impurities, metal exposed	Oxidation and rupturing of the carbon passivation layer.  Ref: <sup>58,85</sup>
Mild Oxidation	0	-	-	+	Good	Less defects	Oxidation in H <sub>2</sub> SO <sub>4</sub> and H <sub>2</sub> O <sub>2</sub> . Shortens the tubes and consume sidewall defects.  Ref: <sup>59</sup>
HNO <sub>3</sub> Treatment	+	+	+	-	Good	Up to < 0.1 wt% metal	Reflux or sonication in nitric acid. Catalyst will solvate.  Ref: <sup>54,55,61,59</sup>
HCl Treatment	0	0	0	-	Good	Up to < 0.1 wt% metal	Reflux or sonication in hydrochloric acid. Catalyst will solvate.  Ref: <sup>54,57,62,63</sup>
Mild Acid Treatment	+	+	+	-	Very good	Up to < 0.2 wt% metal	Removes most of the metal, when the metal surface is totally exposed to the acid. (4 M HCl reflux)  Ref: <sup>58</sup>
Functionalisation (In diethylether)	+	+	+	+	SWNTs ~100 %	~ 0,4 % Metal	Functionalised with 1,3 dipolar cycloaddition and then solvated.  Ref: <sup>66</sup>
Functionalisation (GPC)	+	+	+	+	SWNTs ~74 %	Very pure	Functionalised with octadecylamine. Size separation by GPC.  Ref: <sup>71,72</sup>

+	=	<i>no effect on particle</i>
0	=	<i>effects particle slightly</i>
-	=	<i>effects particle</i>

<i>Technique</i>	SWNT	<i>Carbon particles, graphite</i>	<i>Short fullerenes C<sub>60</sub>, C<sub>70</sub>, etc</i>	<i>Metal catalyst</i>	<i>Yield</i>	<i>Purity</i>	<i>Short description of the technique and literature</i>
Magnetic Purification	+	+	+	-	Very good	Metal hardly detectable	Magnetic particles are trapped with permanent magnetic poles. Ref: <sup>68</sup>
Vacuum Annealing	+	-	-	+	Increases	Increases Less defects	Rearranges the tubes and consumes defects. P = 5.10 <sup>-6</sup> mbar; T = 873 K Ref: <sup>55</sup>
High Temperature Annealing	+	-	-	+	Increases	Increases Less defects	Rearranges the tubes and consumes defects. Annealing in Ar at T = up to 1073 K. Ref: <sup>55,63,66,57</sup>
High Temperature Vacuum Treatment	+	-	-	-	Increases	Increases Less defects	Rearrangement of SWNT walls, removal of graphitic carbon and metals T = 1873 K; p = 10 <sup>-3</sup> Pa. Ref: <sup>61</sup>
HPLC (Size Separation)	+	+	+	+	SWNTs 100 %	Very pure	Size separation. SWNTs must be cut and purified in advance. Ref: <sup>59</sup>
(Ultra)sonication (in alcohol)	+	+	+	+	SWNTs ~100 %	Enhances purification techniques	Enlarges reactive surface, often in combination with other techniques. Suspends particles. Mass separation. Ref: <sup>54,60,64,65,67</sup>
Ultrasonication (in acid)	-	+	+	-	decreases with time	First increases, then decreases	For short times, solvates metal. For longer times, also cuts the tubes. Ref: <sup>63,57,59</sup>
Cutting through Fluorization	-	+	+	+	SWNTs ~ 55 %	Shorter tubes, good purity	Cutting SWNTs with initial length of 1 um. Average length: less than 50 um. Ref: <sup>69</sup>
Ball-milling or grinding	-	-	-	+	decreases with time	SWNTs shorten and more carbon impurities	The SWNTs are mechanically shortened and disordered carbon is formed. Ref: <sup>70</sup>
Filtration	+	+	+	+	Good	Enhances purification techniques	Size or particle separation. Often in combination with other techniques. Ref: <sup>62,55,63,64,65,67</sup>
Cross Flow Filtration	+	+	+	+	Very good	Enhances purification techniques	Size or particle separation, with cross flow. Often in combination with other techniques. Continuous process. Ref: <sup>55,59</sup>
CS <sub>2</sub> Filtration	+	+	-	+	SWNTs ~100 %	No more fullerenes	Easy way to separates fullerenes without harming them. Ref: <sup>66</sup>

Table 3-1: Several techniques for purification of SWNTs

+	=	<i>no effect on particle</i>
0	=	<i>effects particle slightly</i>
-	=	<i>effects particle</i>

## 4. Potential applications of CNTs

### 4.1 Energy storage

Graphite, carbonaceous materials and carbon fibre electrodes are commonly used in fuel cells, batteries and other electrochemical applications. Advantages of considering nanotubes for energy storage are their small dimensions, smooth surface topology and perfect surface specificity. The efficiency of fuel cells is determined by the electron transfer rate at the carbon electrodes, which is the fastest on nanotubes following ideal Nernstian behaviour.<sup>10</sup> Electrochemical energy storage and gas phase intercalation will be described more thoroughly in the following chapters of the report.

#### 4.1.1 Hydrogen storage

The advantage of hydrogen as energy source is that its combustion product is water. In addition, hydrogen can be easily regenerated. For this reason, a suitable hydrogen storage system is necessary, satisfying a combination of both volume and weight limitations. The two commonly used means to store hydrogen are gas phase and electrochemical adsorption.

Because of their cylindrical and hollow geometry, and nanometre-scale diameters, it has been predicted that carbon nanotubes can store a liquid or a gas in the inner cores through a capillary effect. As a threshold for economical storage, the Department of Energy has set storage requirements of 6.5 % by weight as the minimum level for hydrogen fuel cells. It is reported that SWNTs were able to meet and sometimes exceed this level by using gas phase adsorption (physisorption). Yet, most experimental reports of high storage capacities are rather controversial so that it is difficult to assess the applications potential. What lacks, is a detailed understanding of the hydrogen storage mechanism and the effect of materials processing on this mechanism.

Another possibility for hydrogen storage is electrochemical storage. In this case not a hydrogen molecule but an H atom is adsorbed. This is called chemisorption.

#### 4.1.2 Lithium intercalation

The basic principle of rechargeable lithium batteries is electrochemical intercalation and de-intercalation of lithium in both electrodes. An ideal battery has a high-energy capacity, fast charging time and a long cycle time. The capacity is determined by the lithium saturation concentration of the electrode materials. For Li, this is the highest in nanotubes if all the interstitial sites (inter-shell van der Waals spaces, inter-tube channels and inner cores) are accessible for Li intercalation. SWNTs have shown to possess both highly reversible and irreversible capacities. Because of the large observed voltage hysteresis, Li-intercalation in nanotubes is still unsuitable for battery application. This feature can potentially be reduced or eliminated by processing, i.e. cutting, the nanotubes to short segments.

#### 4.1.3 Electrochemical supercapacitors

Supercapacitors have a high capacitance and potentially applicable in electronic devices. Typically, they are comprised two electrodes separated by an insulating material that is ionically conducting in electrochemical devices. The capacity of an electrochemical supercap inversely depends on the separation between the charge on the electrode and the counter charge in the electrolyte. Because this separation is about a nanometre for nanotubes in electrodes, very large capacities result from the high nanotube surface area accessible to the electrolyte. In this way, a large amount of charge injection occurs if only a small voltage is applied. This charge injection is used for energy storage in nanotube supercapacitors.<sup>73</sup> Generally speaking, there is most interest in the double-layer supercapacitors and redox supercapacitors with different charge-storage modes.

## 4.2 Molecular electronics with CNTs

### 4.2.1 Field emitting devices

If a solid is subjected to a sufficiently high electric field, electrons near the Fermi level can be extracted from the solid by tunnelling through the surface potential barrier. This emission current depends on the strength of the local electric field at the emission surface and its work function (which denotes the energy necessary to extract an electron from its highest bounded state into the vacuum level). The applied electric field must be very high in order to extract an electron. This condition is fulfilled for carbon nanotubes, because their elongated shape ensures a very large field amplification.<sup>10</sup>

For technological applications, the emissive material should have a low threshold emission field and large stability at high current density. Furthermore, an ideal emitter is required to have a nanometre size diameter, a structural integrity, a high electrical conductivity, a small energy spread and a large chemical stability. Carbon nanotubes possess all these properties. However, a bottleneck in the use of nanotubes for applications is the dependence of the conductivity and emission stability of the nanotubes on the fabrication process and synthesis conditions.

Examples of potential applications for nanotubes as field emitting devices are flat panel displays, gas-discharge tubes in telecom networks, electron guns for electron microscopes, AFM tips and microwave amplifiers.

### 4.2.2 Transistors

The field-effect transistor – a three-terminal switching device – can be constructed of only one semi-conducting SWNT. By applying a voltage to a gate electrode, the nanotube can be switched from a conducting to an insulating state.<sup>73</sup> A schematic representation of such a transistor is given in Figure 4-1.

Such carbon nanotube transistors can be coupled together, working as a logical switch, which is the basic component of computers.<sup>74</sup>

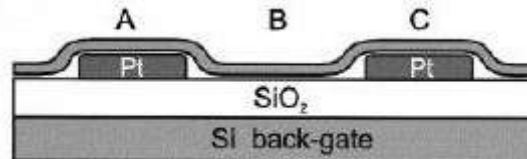


Figure 4-1: A single semi-conducting nanotube is contacted by two electrodes. The Si substrate, which is covered by a layer of SiO<sub>2</sub> 300nmthick, acts as a back-gate.

## 4.3 Nanoprobes and sensors

Because of their flexibility, nanotubes can also be used in scanning probe instruments. Since MWNT-tips are conducting, they can be used in STM and AFM instruments (Figure 4-2). Advantages are the improved resolution in comparison with conventional Si or metal tips and the tips do not suffer from crashes with the surfaces because of their high elasticity. However, nanotube vibration, due to their large length, will remain an important issue until shorter nanotubes can be grown controllably.

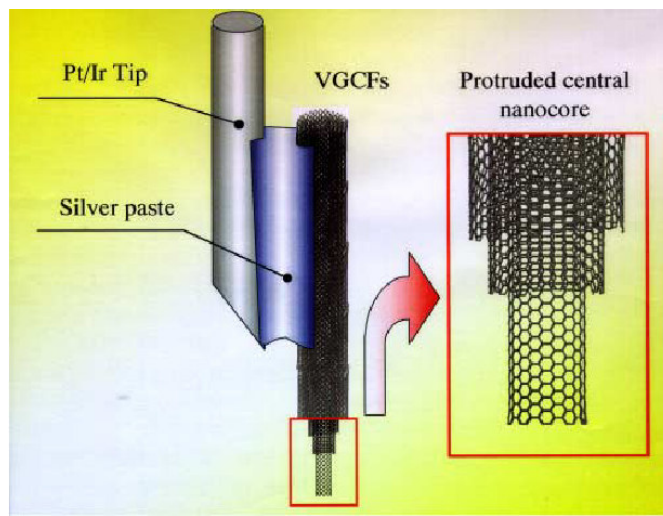


Figure 4-2: Use of a MWNT as AFM tip. VGCF stands for Vapour Grown Carbon Fibre. At the centre of this fibre the MWNT forms the tip.<sup>10</sup>

Nanotube tips can be modified chemically by attachment of functional groups. Because of this, nanotubes can be used as molecular probes, with potential applications in chemistry and biology.

Other applications are the following:

- A pair of nanotubes can be used as tweezers to move nanoscale structures on surfaces.<sup>73</sup>
- Sheets of SWNTs can be used as electromechanical actuators, mimicking the actuator mechanism present in natural muscles.
- SWNTs may be used as miniaturised chemical sensors. On exposure to environments, which contain NO<sub>2</sub>, NH<sub>3</sub> or O<sub>2</sub>, the electrical resistance changes.

## 4.4 Composite materials<sup>10</sup>

Because of the stiffness of carbon nanotubes, they are ideal candidates for structural applications. For example, they may be used as reinforcements in high strength, low weight, and high performance composites.

Theoretically, SWNTs could have a Young's Modulus of 1 TPa. MWNTs are weaker because the individual cylinders slide with respect to each other. Ropes of SWNTs are also less strong. The individual tubes can pull out by shearing and at last the whole rope will break. This happens at stresses far below the tensile strength of individual nanotubes. Nanotubes also sustain large strains in tension without showing signs of fracture. In other directions, nanotubes are highly flexible.<sup>10</sup>

One of the most important applications of nanotubes based on their properties will be as reinforcements in composite materials. However, there have not been many successful experiments that show that nanotubes are better fillers than the traditionally used carbon fibres. The main problem is to create a good interface between nanotubes and the polymer matrix, as nanotubes are very smooth and have a small diameter, which is nearly the same as that of a polymer chain. Secondly, nanotube aggregates, which are very common, behave different to loads than individual nanotubes do. Limiting factors for good load transfer could be sliding of cylinders in MWNTs and shearing of tubes in SWNT ropes. To solve this problem the aggregates need to be broken up and dispersed or cross-linked to prevent slippage.

A main advantage of using nanotubes for structural polymer composites is that nanotube reinforcements will increase the toughness of the composites by absorbing energy during their highly flexible elastic behaviour. Other advantages are the low density of the nanotubes, an increased electrical conduction and better performance during compressive load.

Another possibility, which is an example of a non-structural application, is filling of photoactive polymers with nanotubes. PPV (Poly-p-phenylenevinylene) filled with MWNTs and SWNTs is a composite, which has been used for several experiments. These composites show a large increase in conductivity with only a little loss in photoluminescence and electro-luminescence yields. Another benefit is that the composite is more robust than the pure polymer.

Of course, nanotube-polymer composites could be used also in other areas. For instance, they could be used in the biochemical field as membranes for molecular separations or for osteointegration (growth of bone cells). However, these areas are less explored. The most important thing we have to know about nanotubes for efficient use of them as reinforcing fibres is knowledge on how to manipulate the surfaces chemically to enhance interfacial behaviour between the individual nanotubes and the matrix material.

## 4.5 Templates<sup>10</sup>

Because of the small channels, strong capillary forces exist in nanotubes. These forces are strong enough to hold gases and fluids in nanotubes. In this way, it may be possible to fill the cavities of the nanotubes to create nanowires. The critical issue here is the wetting characteristic of nanotubes. Because of their smaller pore sizes, filling of SWNTs is more difficult than filling of MWNTs.

If it becomes possible to keep fluids inside nanotubes, it could also be possible to perform chemical reactions inside their cavities. Especially organic solvents wet nanotubes easily. In this case we could speak of a nanoreactor.

One of the problems in these cases is that nanotubes are normally closed. For the latter applications we have to open the nanotubes. This is possible through a simple chemical reaction: oxidation. The pentagons in the end cap of the nanotubes are more reactive than the sidewall. So, during oxidation, the caps are easily removed while the sidewall stays intact.

## 5. Energy storage

Two elements that can be electrochemically stored in CNTs are hydrogen and lithium. Hydrogen can also be stored in CNTs by gas phase intercalation. Three units are commonly used to describe the hydrogen and lithium contents of storage materials with:

1. [H/C] ([Li/C]) as the ratio of hydrogen (lithium) atoms per atom of storage material, in this case carbon;
2. [wt%] as the ratio of the mass of hydrogen (lithium) to the mass of storage material (the gravimetric density);
3. [ $\text{kgH}_2\text{m}^{-3}$ ] as the ratio of the mass of molecular hydrogen to the volume of storage material (volumetric density).<sup>75</sup>

### 5.1 Electrochemical storage of hydrogen

#### 5.1.1 Experimental studies

There are two methods to store hydrogen atoms reversibly in CNTs. One method is called gas phase intercalation and it is explained in section 5.3. The second method described in this section is based on a electrochemical charge-discharge process, in which the hydrogen absorption is controlled by the potential.<sup>76</sup>

The hydrogen storage capacity of the CNT samples is analysed by means of electrochemical galvanostatic measurement in a 6 M KOH electrolyte. There are commonly three electrodes in the set-up: a work electrode (negative), often made of a mixture of gold or nickel with the nanotube material pressed into a pellet, a reference electrode (Hg/HgO/OH<sup>-</sup>) and a counter electrode, usually made of nickel. In Figure 5-1, the reference electrode is left out. Instead, a polymer separator separates the working and the counter electrode.

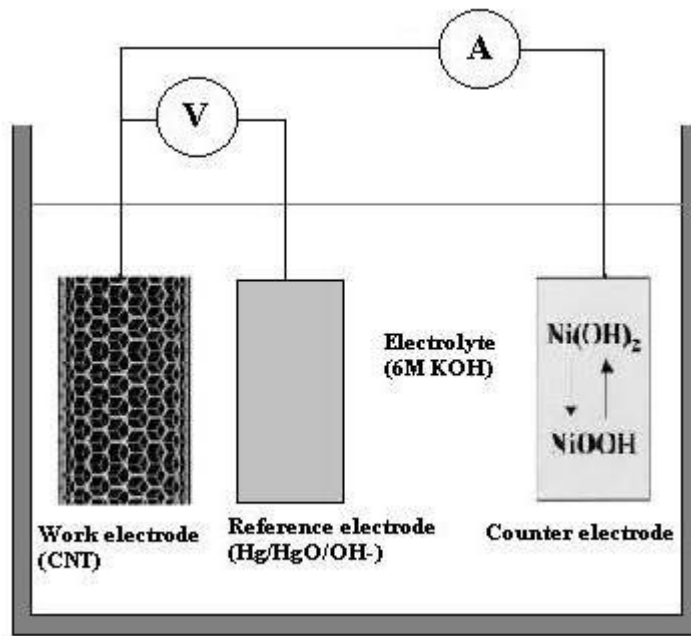


Figure 5-1: A schematic diagram of a charge-discharge cycling apparatus.<sup>76</sup>

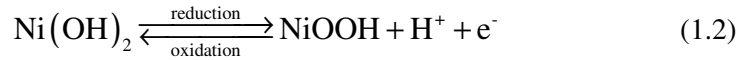
During the charging process, the water in the electrolyte dissociates at the work electrode. The adsorbed atomic hydrogen may be absorbed or intercalate in the electrode or recombine at the surface to molecular hydrogen and diffuse into the electrode or form gas bubbles at the surface of the electrode. During the discharge process, the hydrogen in the electrode recombines with the OH<sup>-</sup> ions in

the electrolyte to form water molecules. The amount of hydrogen desorbed from the electrode can therefore be measured by measuring the electric charge, which is equal to the product of current and time in a galvanostatic setup.<sup>77</sup>

The following equation gives the reaction in the working electrode:



The reaction at the counter electrode, in the case of a Ni-electrode is given by:



When measuring the electrochemical hydrogen storage capacity of a CNT sample, a double-layer capacitance is measured too. This effect has to be taken into account when looking at the experimental results of the capacity measurements.

Measurement methods are charge-discharge measurements, cyclic voltammetry, constant current measurements, electrochemical impedance measurements and chrono amperometry. The charge/discharge experiments are commonly performed at a constant current. During the discharge, the cell resistance leads to an overpotential. With cyclic voltammetry, different voltages are applied at a certain sweep rate and the current is measured. From the thus obtained oxidation and reduction peaks it can be speculated if the hydrogen adsorption is due to the CNTs or not. With chrono amperometry the current behaviour is studied after applying a voltage step. From impedance spectra, performed by applying sinusoidal voltage over a certain frequency range, a 'complex' resistance of the CNT-sample can be calculated. These spectra commonly consist of two semicircles and a slope, similar to a metal hydride.<sup>78,79</sup> The smaller semicircle in the high frequency region is probably due to the double-layer capacitance. The semicircle in the low frequency region is attributed to an electrochemical reaction. *Gao et al.* have studied these spectra of CNTs decorated with metallic nickel as a function of cycling and found that the smaller semicircle hardly changed upon cycling, while the larger semicircle remarkably increased, indicating an increase in surface reaction resistance upon cycling.<sup>78</sup>

Several experiments have been performed in this research area with often differing conclusions. An overview of most of these results up to 2002 is given in Table 5-1. Note that 1 Ah/g corresponds to 3.54 wt% hydrogen stored in carbon. (References to the articles of the cited results are all in the reference list at the end of the report.)

Material	Process	Purity	Discharge capacity (mAh/g)	Stored hydrogen (wt%)	Reference	Year
SWNT	Arc	a few %	110	0.39	Nutzenadel	1999
MWNT	CVD	?	200	0.8	Qin	2000
SWNT	Arc	80%	800	2.9	Rajalakshmi	2000
SWNT	LA	90%	440	1.616	Fazle Kibria	2001
SWNT (Li)	LA	90%	640	2.333	Fazle Kibria	2001
MWNT	CVD	?	297	1.051	Gao	2001
SWNT	?	?	<141	< 0.5	Frackowiak	2002
SWNT-ropes	Arc	60-70 %	503	1.84	Dai	2002
SWNT	Arc	50%	552	2	Zuttel	2002
SWNT	Arc	70%	550	2	Zuttel	2002

Table 5-1: Overview of reported storage capacities of hydrogen in carbon nanotubes up to 2002, investigated in an electrochemical system.<sup>80</sup>

*Nutzenadel et al.* demonstrated in 1999 that SWNTs could electrochemically store hydrogen, in which SWNT soot containing a few percent of 0.7 – 1.2 nm diameter SWNTs was mixed with gold as a compacting powder (to stabilise the electrodes) in a 1:4 ratio to form electrodes. Gold was used because it is noble and does not participate in any electrochemical reaction. In the nanotubes-sample, nickel, iron and C<sub>60</sub> were present too. Pure samples of both nickel and iron did not hydride during cycling and C<sub>60</sub> only showed a low capacity of 14 mAh/g. For the nanotubes-sample they found a maximum capacity of 110 mAh/g, indicating that the nanotubes are responsible for the hydrogen uptake. This result corresponds to ~0.39 wt% hydrogen. Only slight capacity loss was observed after many cycles.<sup>81</sup>

*Dai et al.* investigated the electrochemical hydrogen storage behaviour of ropes of aligned SWNTs (up to 100 mm in length and 50  $\mu\text{m}$  in diameter) with a large sample quantity of 200 mg (with a purity in the range 60-70%) at 298 K under normal atmosphere. The work electrode was made without compacting powder by pressing the sample to a sheet of nickel foam. With a constant current density of 25 mA/g, the plateau of the discharge potential was observed around  $-0.6\text{ V}$  (vs Hg/HgO) and a discharge capacity of 503 mAh/g was obtained, corresponding to a hydrogen storage capacity of 1.84 wt% in SWNTs. They observed the same maximum discharge capacity for three different samples, so the results appeared reproducible. After 100 cycles the electrode still retained 80% of the maximal capacity. The loss is believed to be due to the mechanical instability of the electrode. The investigators explain the higher capacity (in comparison to the 110 mAh/g obtained by *Nutzenadel et al.*) as due to the purity and larger mean diameter of the SWNTs (1.72 nm, resulting in larger micropores). Furthermore, no compacting powder was used, resulting in a higher percentage of SWNTs in unit volume in the work electrode.<sup>82</sup>

*Fazle Kibria et al.* compared the electrochemical hydrogen storage behaviours of CNTs grown by chemical vapour deposition (CVD), arc-discharge (AD) and laser ablation (LA). The latter were purified (90 wt%). The charge capacities of the electrodes remained unchanged with increasing cycle number, but the reversible capacity behaviour decreased with cycling. The samples with the LA grown CNTs stored the highest amount of hydrogen, 1.6 wt% (corresponding to 400 mAh/g), which was 16 times that of CVD and AD grown CNTs. During purification, besides the elimination of metals and amorphous carbon, CNTs may separate partially from their bundles, resulting in an increase in active sites for hydrogen storage for the LA grown CNTs. They also investigated the charge-discharge behaviours for Li-, Na- and K-doped sample electrodes. Each sample obtained a higher hydrogen capacity. The Li-doped CVD electrode showed a unique discharge behaviour during cycling. With increasing cycle number, the sample showed a large capacity reversibility. The investigators concluded from cyclic voltammetric measurements that the high hydrogen storage capacity of the alkali metal-doped CNTs originated from an increase in hydrogen adsorption sites. This is suggested to be due to the introducing of the metals in the CNT bundles and separation of tubes, but not from their chemical effect.<sup>83</sup>

More recently, *Zuttel et al.* investigated several nanotubes samples at room temperature, fabricated of a mixture of 10 mg of SWNT material with 90 mg of gold powder to form a mechanically stable and conducting electrode. Figure 5-2 shows the charge-discharge equilibrium curves measured with the SWNT/gold electrode. The shape of the curves is different than the shape of an equilibrium curve for a metal hydride, in which there is a wide plateau due to a phase transition occurring at a specific potential. In nanotubes, there are no well-defined interstitial sites and no phase transition is expected.<sup>81</sup>

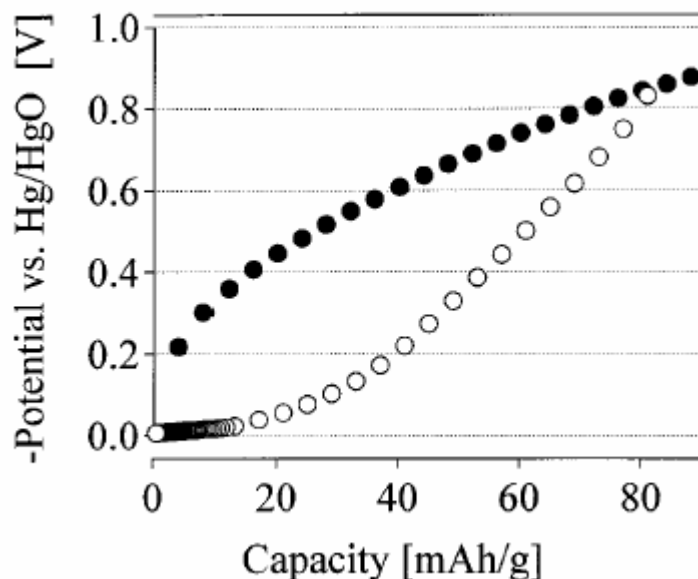


Figure 5-2: Equilibrium charge-discharge curves of an electrode of SWNTs with gold as compacting powder (full circle: charge; open circle: discharge). The shape of the curve is different from that for metal hydrides where a plateau occurs.<sup>81</sup>

A few SWNT samples showed hydrogen storage capacities in the range of 0.7-0.9 wt%. The fact that this reaction was reversible is a good indication that the measured capacity is due to hydrogen storage. An additional discharge from the oxidation of impurities in the nanotubes would not necessarily be reversible. The electrochemically measured discharge capacity at 293 K of the nanotube samples correlated with the surface area. The linear relationship is shown in Figure 5-3. Note that only the round markers in the graph represent the surface area of CNT-samples, the fitted line corresponds to this data (the data from gas phase experiments, indicated by triangular markers, were found by *Nijkamp et al.* and are not included in this fit). The line intercepts the axis at the origin and the slope is 1.5 wt%/1000 m<sup>2</sup>/g. Theoretically, the maximum specific surface area is 2630 m<sup>2</sup>g<sup>-1</sup>. From this, they extrapolated a maximum discharge capacity of 2 wt%.<sup>77</sup>

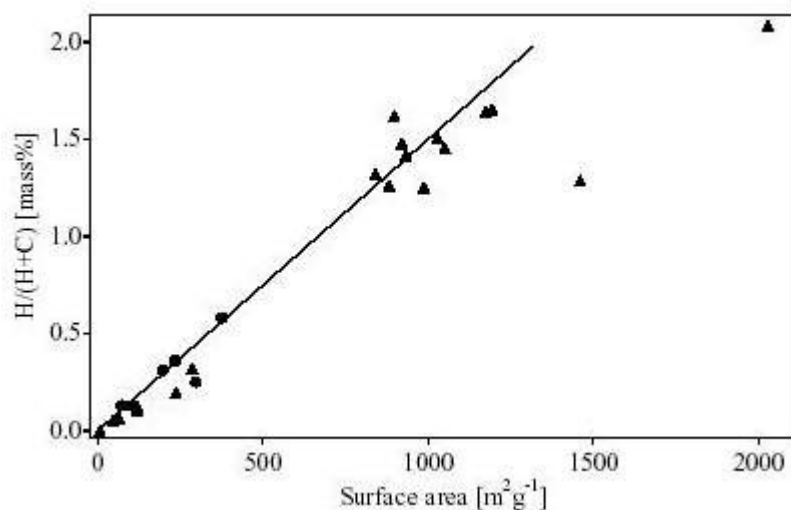


Figure 5-3: Desorbed amount of hydrogen versus the surface area (round markers, corresponding to the electrochemical experiments) of several CNT samples with a linear fit (corresponding to the data of the round markers). The triangular markers correspond to gas phase experiments, carried out by *Nijkamp et al.*<sup>77</sup>

Less encouraging results are from *Frackowiak et al.* who investigated the accumulation of hydrogen by the electrochemical decomposition of aqueous alkaline medium on a negatively polarised carbon electrode under ambient conditions. For several SWNTs the reversible hydrogen storage capacity never exceeded 0.5 wt%. They compared several published data and found no systematic relationship

between the indicated purity and the maximum discharge capacity, suggesting that SWNTs are probably not responsible for the values of sorption observed. Their final conclusion is that hydrogen storage capacity of SWNTs under a high pressure at room temperature is negligible.<sup>84</sup>

### 5.1.2 Modelling

In this section, a review of the modelling studies on the chemisorption of hydrogen is given, but it must be mentioned that all these studies involve modelling of storage in the gas phase.

Simultaneously to experimental studies of hydrogen storage in CNTs, model calculations of chemisorption and physisorption by the nanotubes were performed. These are very useful for understanding the elementary steps of the adsorption procedure and give insight in the phenomenon. From 2001, the quantum picture was introduced into the molecular dynamics study of hydrogen either by quantum molecular dynamics algorithms or by minimal *ab initio* calculations in parts of classically optimised tube geometries. The main reason that *ab initio* calculations on CNTs have appeared only lately is the system size. In order to take into account a large enough model of a SWNT, you need approximately 200 atoms. The problem is then how to treat a large system using an accurate *ab initio* method without ending up with a prohibitively large calculation.

There are two different ways to deal with this dilemma. One can use the periodicity of the CNTs and combine an *ab initio* method with periodic boundary conditions. The advantage is that the total system is treated with *ab initio* techniques, while the disadvantage is that an external periodicity is forced on the system. The second solution involves a two-level quantum mechanics/molecular mechanics (QM/MM) approach, in which the tube is divided into two different parts treated with different methods. For this model there is no periodic constraint, but its disadvantage is that only a relatively small part of the system is treated quantum mechanically, while the rest is used for constraining the boundaries. Both approaches have although the disadvantage of excluding temperature from the calculations.<sup>85</sup>

*Cracknell* has simulated the hydrogen adsorption in MWNTs and SWNTs. The gas-solid interaction was modelled as pure dispersion forces and with a hypothetical model for chemisorption. The method used for modelling dispersion forces is based on integrating the Lennard-Jones interaction between the adsorbent and adsorbate over the surface of the pore walls and ignoring the detailed surface structure. The hydrogen molecule is modelled as a dumbbell molecule with two Lennard-Jones sites. The standard equation for the Lennard-Jones interaction between the potential is<sup>86</sup>:

$$U_{LJ}(r) = 4\epsilon_{H-H} \left[ \left( \frac{\sigma_{H-H}}{r} \right)^{12} - \left( \frac{\sigma_{H-H}}{r} \right)^6 \right] \quad (1.3)$$

where  $r$  is the distance between the centres of mass of two hydrogen atoms. The cross parameters for the Lennard-Jones interaction between the hydrogen site and the graphitic surface were calculated using the Lorentz-Berthelot rules<sup>86</sup>:

$$\sigma_{HC} = \frac{1}{2} [\sigma_{CC} + \sigma_{HH}] , \quad \epsilon_{HC} = (\epsilon_{CC} \epsilon_{HH})^{1/2} \quad (1.4)$$

For modelling the hypothetical chemisorption within the nanotubes, the chemisorption minimum from a model by *Jeloaica et al.*<sup>86</sup> (called chemisorption2, see Figure 5-4) was combined with the dispersion minimum (10-4-3) calculated from the Lennard-Jones interactions between a hydrogen site and the wall.

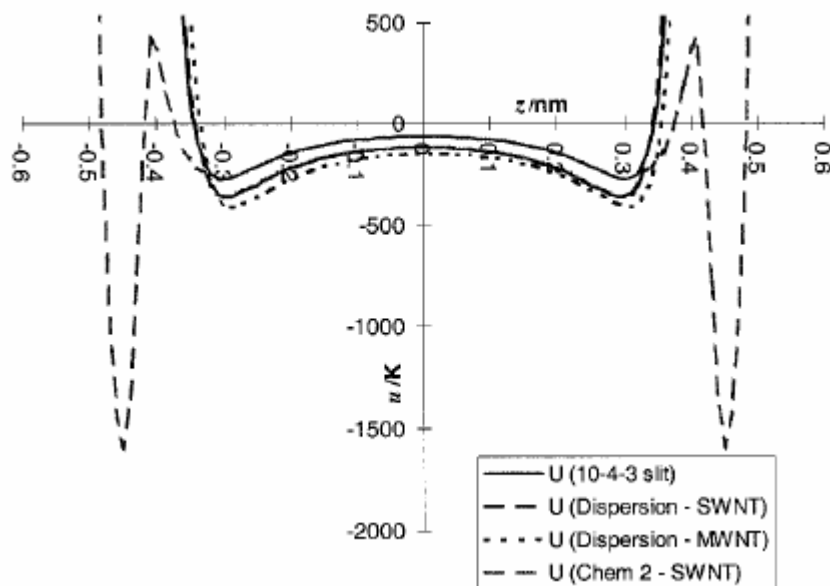


Figure 5-4: Comparison of 10-4-3 potential for interaction of a single hydrogen site with a graphitic surface and two hypothetical models for chemisorption ( $z$  = distance from wall).<sup>87</sup>

For each possible nanotube wall-hydrogen distance  $z$ , this combined potential was calculated by comparing the energy of the chemisorption potential in a planar system and the potential calculated from the integration of the Lennard-Jones potential over the surface of the pore wall. The minimum of the two values was then taken. Uptake of hydrogen in the internal space of a CNT is predicted to be lower than in the optimal graphitic nanofibre with slitlike pores. An uptake of 3.2 wt% is measured in pores of diameter 1.2 nm (see Figure 5-5).

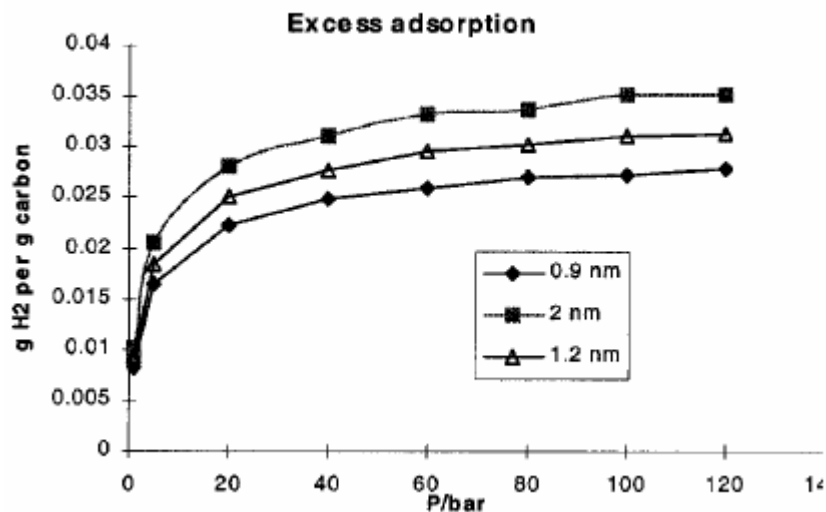


Figure 5-5: Simulated adsorption isotherms for hydrogen in SWNTs of differing diameters at 298 K. The SWNT adsorption refers only to the internal pore space and ignores any interstitial adsorption.<sup>87</sup>

The majority of the differences can be attributed to the curvature of the pore. This reduces the uptake of hydrogen in spite of deepening the potential minimum inside the pore associated with dispersion forces. It is concluded that for uptake of hydrogen of 5-10 wt% gas-solid forces other than dispersion forces are required and most of the adsorption must occur in the interstices between the SWNTs.<sup>87</sup>

A mixed quantum mechanics/molecular mechanics (QM/MM) model is used by *Froudakis* for investigating the nature of hydrogen adsorption in a 200-atom (4,4) SWNT, treating up to 64 carbon atoms and 32 hydrogen atoms with the higher level of theory. The tube was divided into three cylindrical parts (see Figure 5-6).

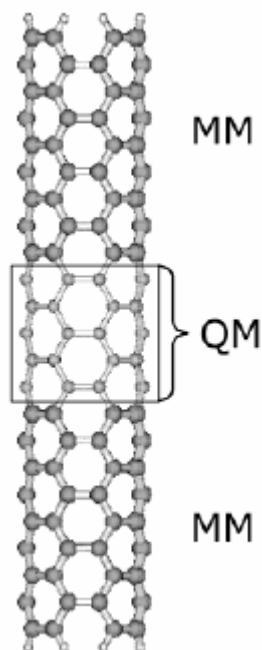


Figure 5-6: A QM/MM model simulating a (4,4) SWNT. The tube is separated into three cylindrical parts. The inner part is treated with DFT (40 carbon atoms) while the two outer parts are treated with MM. The dangling bonds at the ends of the tube were saturated with hydrogen atoms.<sup>88</sup>

The inner part was treated with DFT, while the two outer parts were treated with molecular mechanics. The three-parameter hybrid functional of Becke was employed for the higher theoretical level. The two outer cylindrical parts were treated with the universal force field (UFF), while the dangling bonds at the ends of the tube were saturated with hydrogen atoms. It was investigated what potential the hydrogen atom feels as it approaches the CNT. A combined interpretation of the potential curves during the hydrogen approach to a CNT in two different pathways (towards a carbon atom and towards the centre of a C-hexagon) shows that despite the approaching direction, the H will feel an attraction from the C atoms of the tube and finally will bind to the wall of the tube and will not enter inside. Two forces compete in the approaching procedure. The more hydrogen atoms are in the C-hexagon, the larger the hexagon is and the easier a hydrogen atom enters the tube. On the other hand, the hydrogen atoms in the hexagon are screening the attraction of the carbon atom to the external hydrogen. As a result, the energetically favourable H-approach is when the tube wall is half-filled with hydrogen atoms. Furthermore, it was shown that the binding will take place in zigzag rings around the tube walls and not in lines toward the tube axis, changing the tube shape and causing an enlargement of the tube volume by 15 %.<sup>88</sup>

By Yang *et al.* *ab initio* molecular orbital (MO) calculations are performed to study the adsorption of H atoms on three faces of graphite: basal plane, zigzag edge and armchair edge. It is thought that the adsorption on nanotubes is comparable to that on graphite. Clear indications of chemisorption are the slow uptake of hydrogen and the necessity to heat up the sample to desorb the adsorbed hydrogen completely. The edge sites of graphite may play a significant role in hydrogen storage, as they are abundant in GNFs as well as in nanotubes after acid and heat treatments. Hence it is important to study edge sites where hydrogen dissociation can take place.

For the calculations the unrestricted Hartree-Fock method was used for geometric optimisation and the self-consistent field energy. B3LYP/6-31G (method and used basis set) was used for the single point energy and bond population calculations for the more accurate results. The geometry-optimised structures were used to calculate the energy of chemisorption ( $E_{\text{ads}}$ ):  $E_{\text{ads}} = E_{\text{graphite-hydrogen}} - E_{\text{graphite}} - E_{\text{hydrogen}}$ . A higher negative value of  $E_{\text{ads}}$  in kcal/mole corresponds to a stronger adsorption. The different used models are given in Figure 5-7 and Figure 5-8.

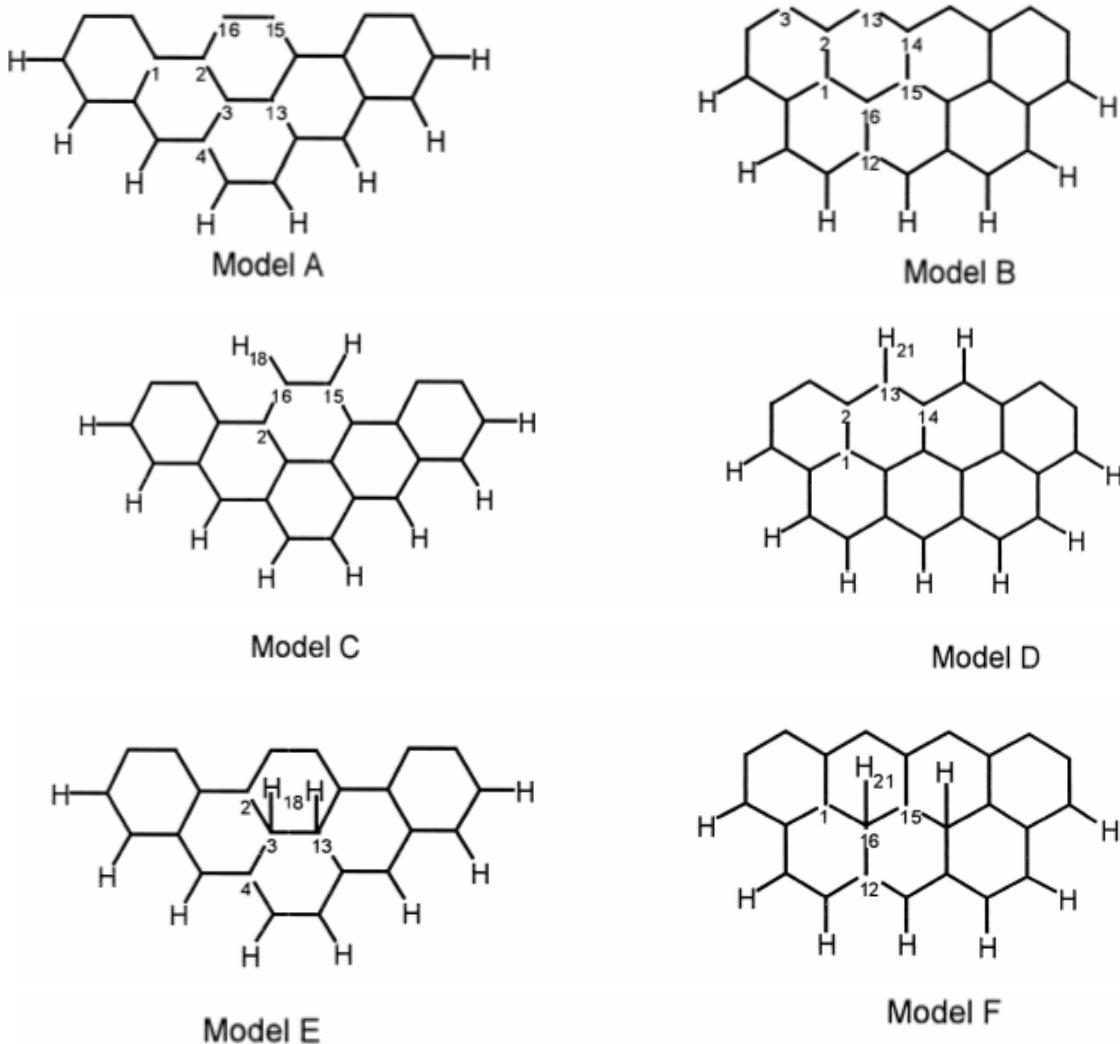


Figure 5-7(A-F): Model A is the armchair graphite model. Model B is the zigzag graphite model. Models C and D represent the structure of one H atom chemisorbed per edge carbon on these graphite planes. The models E and F represent H atoms adsorbed on the basal plane sites.<sup>89</sup>

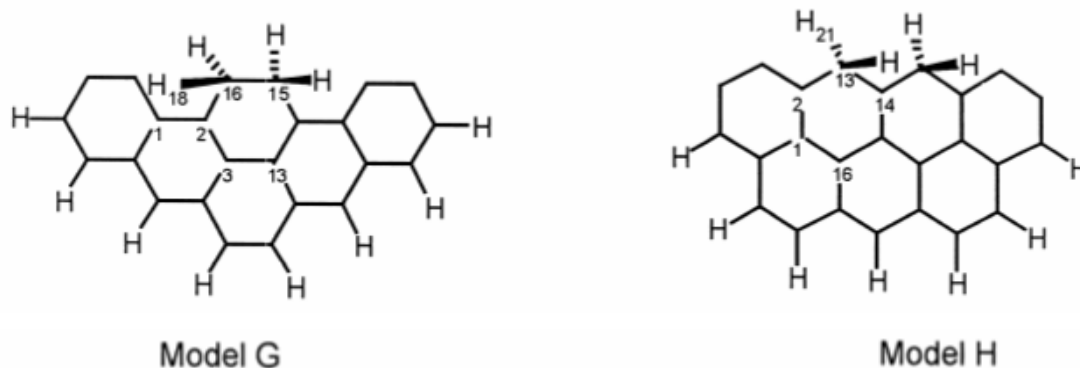


Figure 5-8 (G-H): Model G represents the structure of two H atoms chemisorbed per edge carbon of the armchair face of graphite. Model H represents the same, but for the zigzag face of graphite.<sup>89</sup>

Model C represents the structure of one hydrogen atom chemisorbed per edge carbon on the armchair plane of graphite. Model D represents the same, but for the zigzag edge of graphite. For chemisorption

on the edge sites, no significant changes in bond length or bond population are seen. Only the C(15)-C(16) bond is weakened by H adsorption.

The models E and F represent hydrogen atoms adsorbed on the basal plane sites. In model E, two hydrogen atoms are bonded to two adjacent carbons as in model F they are further apart. There are, in both cases, significant increases in C-C and C-H bond lengths where hydrogen is directly involved. Also, the bond population decreases, which indicates weaker C-C and C-H bonds. The *ab initio* results from this work show that the adsorption of an H atom on the basal plane is exothermic and stable.

Another possibility is the chemisorption of two hydrogen atoms per edge carbon. For the armchair face of graphite this is shown in model G and for the zigzag face this is represented by model H. In this case, the C-C bonds are weakened where H atoms are directly involved. This bond weakening is significantly higher with two hydrogen atoms bonded on each carbon. The same holds for the C-H bond.

In this study with *ab initio* MO calculations, it is found that both edge planes and basal planes in graphite can chemisorb hydrogen. The strength of this chemisorption is higher on the edge planes than on the basal planes. The order of this chemisorption strength is as follows:

zigzag edge > armchair edge > basal plane

For adsorption on both edge planes, the bond energy decreases when two H atoms are adsorbed on each carbon site as compared with one H per site. For adsorption on the basal plane sites, the energy of adsorption is substantially lower when the H atoms are occupying adjacent sites.

*Bauschlicher* studied the bonding of H atoms on the exterior wall of SWNTs. He calculated the bond energies for the tube with 1 H, 2 H, 24 %, 50 % and 100 % coverages. The average C-H bond for the first H was 21.6 kcal/mole and 40.6 kcal/mole for the first two H atoms. For 50 % coverage this average bond energy was 57.3 kcal/mole, decreasing to 38.6 kcal/mole for 100 % coverage.<sup>90</sup>

The C-H bond energies on the tube are in general agreement with that on the basal plane of graphite. The experimental results are thus in agreement with the results from *Yang et al.* So, it is unlikely that the adsorption of H atoms would be significantly different on the basal plane of graphite than on the exterior wall of the nanotube.<sup>89</sup>

## 5.2 Electrochemical storage of lithium

### 5.2.1 Experimental studies

Lithium intercalated graphite and other carbonaceous materials are commercially used in Li-ion batteries. In this case, the specific energy capacity is partially limited by the thermodynamically determined equilibrium saturation composition of  $\text{LiC}_6$ . During intercalation (discharging) the following adsorption takes place:



Or written in a different way:



During de-intercalation (charging) the process is reversed. In graphite this adsorption could be visualised as in Figure 5-9.<sup>91</sup>

Carbon nanotubes are interesting intercalation hosts because of their structure and chemical bonding. Nanotubes might have a higher saturation composition than graphite as guest species can intercalate in the interstitial sites and between the nanotubes. Therefore, carbon nanotubes are expected to be suitable high energy density anode materials for rechargeable Li-ion batteries.<sup>92</sup>

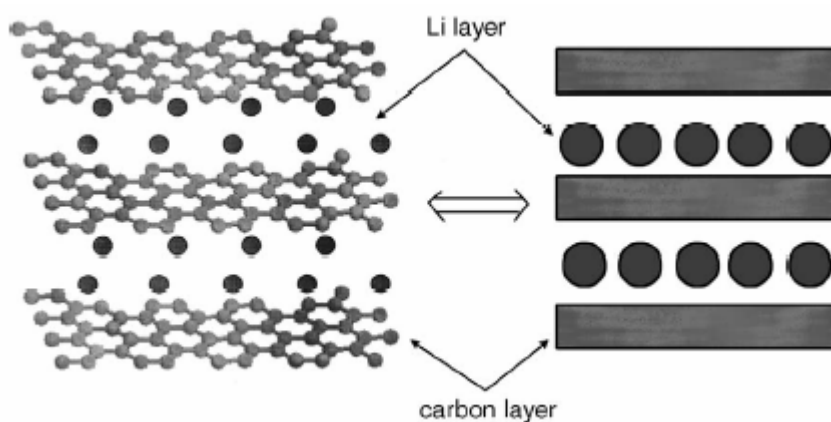


Figure 5-9: Structure of graphite intercalated with lithium.<sup>91</sup>

SWNTs spontaneously form bundles that are called nanoropes. These bundles are kept together by Van der Waals forces. Reversible, electrochemical intercalation of SWNT bundles with lithium has been demonstrated in the past few years. If SWNTs have been purified, they show a reversible saturation composition of  $\text{Li}_{1.7}\text{C}_6$  (632 mAh/g). In any case, this is higher than  $\text{LiC}_6$ , which is the ideal value for graphite this corresponds to a capacity of 372 mAh/g. This  $\text{LiC}_6$  value also holds for MWNTs. However, ball-milling can further increase the reversible saturation Li composition of SWNTs. This process induces disorder within the SWNT bundles and fractures the individual nanotubes. After ball-milling the saturation composition can be as high as  $\text{Li}_{2.7}\text{C}_6$  which corresponds to a capacity of 1000 mAh/g.<sup>93,70,94</sup>

*B. Gao et al.*<sup>70</sup> use SWNT bundles synthesised by laser ablation. The crude materials were purified by filtering off the impurities over a micro-pore membrane while keeping the nanotubes in suspension. The purified material existed for 80% of SWNT bundles with a bundle diameter varying between 10 and 40 nm. The individual nanotube diameter in the bundles was between 1.3 and 1.6 nm. The purified SWNTs from the same batch were divided into several groups. Every group was treated differently by impact ball-milling in air for up to 20 minutes. The charge-discharge data of each group are now being observed.

A composition of  $\text{Li}_{5.4}\text{C}_6$  was obtained after the first discharge with the untreated purified SWNTs. The reversible capacity,  $C_{\text{rev}}$ , is  $\text{Li}_{1.6}\text{C}_6$ . A large voltage hysteresis between discharge and charge cycle was observed in all samples measured. This hysteresis is related to the kinetics of the occurring electrochemical reaction. Preliminary experiments have shown that cutting nanotubes to smaller segments can reduce hysteresis.

The ball-milled samples showed a better performance.  $C_{\text{rev}}$  increased with increasing processing time showing a maximum after 10 minutes of ball-milling. In this case,  $C_{\text{rev}}$  equals  $\text{Li}_{2.7}\text{C}_6$ . Further processing of the nanotubes led to a lower  $C_{\text{rev}}$ . The for 10 minutes ball-milled samples showed very little capacity decay after 5 discharge-charge cycles at a current of 500 mA/g.

It was suggested that SWNTs were fractured and shortened by ball-milling. With Raman spectroscopy, different samples (before and after ball-milling) were analysed (Figure 5-10). The peak around  $1600\text{ cm}^{-1}$  is associated with some of the SWNT vibrational modes. The peak at  $1340\text{ cm}^{-1}$  is associated with disordered carbon. One can see that the major phase in the sample ball-milled for 10 minutes still consists of SWNTs. This is in contrast with the 20 minutes ball-milled sample. It seems that ball-milling increases the  $C_{\text{rev}}$  of SWNTs, but ball-milling too long gives the opposite effect. Ball-milling the SWNTs for 10 minutes gives the best results for Li intercalation.

However, the exact mechanism for the enhanced Li intercalation capacity in ball-milled SWNTs is not clear. It is suggested that the enhanced capacity is related to the degree of disorder within the bundle, and lithium diffusion into the inner cores of the fractured nanotubes.

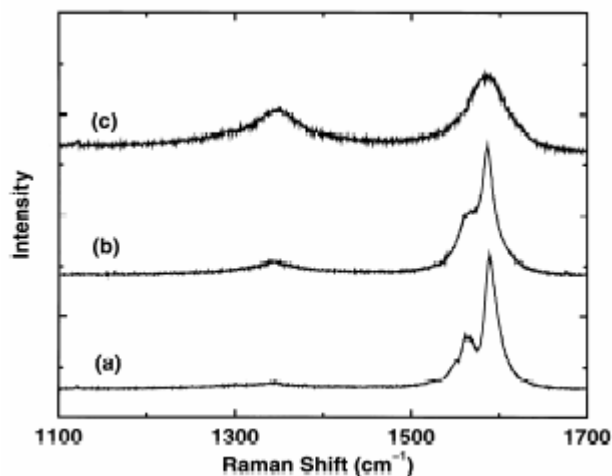


Figure 5-10: Raman spectra of purified [a], 10 minute [b] and 20 minute [c] ball-milled SWNT materials.<sup>70</sup>

H. Shimoda *et al.*<sup>95</sup> also used SWNT bundles synthesised by laser ablation. Their purified samples contain over 90% SWNT bundles with a length of  $10\text{ }\mu\text{m}$  and a bundle diameter of  $30\text{-}50\text{ nm}$ , while the average diameter of an individual nanotube was estimated at  $1.4\text{ nm}$ . The purified bundles were processed to shorter ones by sonication in a solution of  $\text{H}_2\text{SO}_4$  and  $\text{HNO}_3$  for 10-24 hours. The average lengths of the bundles were reduced to  $4\text{ }\mu\text{m}$  after 10 hours and to  $0.5\text{ }\mu\text{m}$  after 24 hours of processing. After chemical etching, the samples (the purified sample, A, also) were electrochemically reacted with lithium. Then, the reversible capacity of the samples was analysed. This capacity turned out to be  $\text{Li}_2\text{C}_6$  ( $744\text{ mAh/g}$ ) for the sample with a bundle length of  $4\text{ }\mu\text{m}$  (sample B) and  $\text{Li}_{2.1}\text{C}_6$  ( $781\text{ mAh/g}$ ) for the sample with a bundle length of  $0.5\text{ }\mu\text{m}$  (sample C). This is an increase of a factor 2 with regard to sample C (Figure 5-11). This effect is attributed to Li filling of the interior space of the chemically etched SWNTs. However, the difference in capacity between samples B and C is not very big despite their difference in length. So, it seems that etching for more than 10 hours has no additional value.

The voltage hysteresis was  $0.5\text{ V}$  lower in sample C compared with sample A. This indicates a shorter diffusion path or diffusion barrier in the etched samples, which is consistent with the observation of smaller bundle diameter and length in sample C. It is clear that etching for more than 10 hours gives a better effect in this case.

It can be concluded that processed SWNTs have a better reversible capacity concerning lithium intercalation with regard to simple purified SWNTs. So, SWNT bundles seem to be attractive host materials for energy storage.

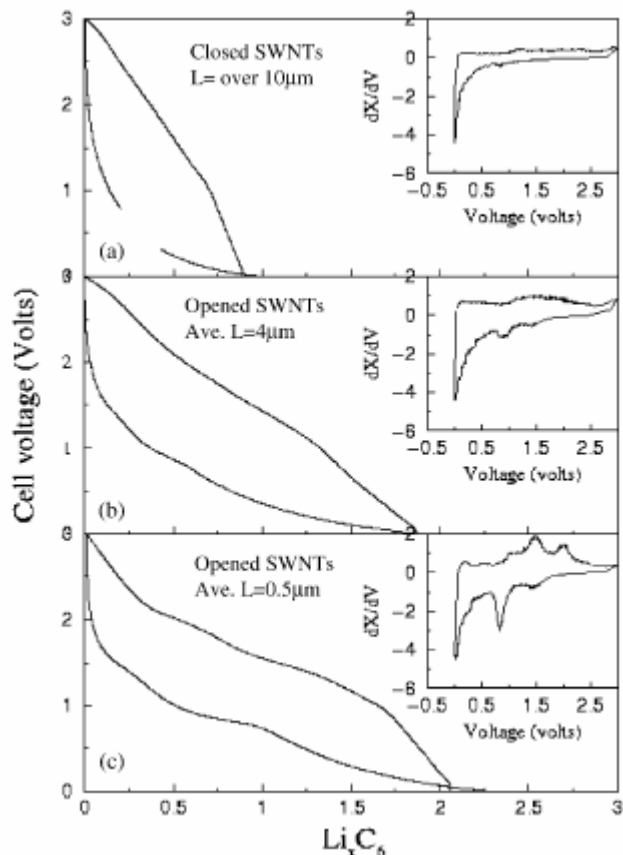


Figure 5-11: Second cycle intercalation (discharge) and deintercalation (charge) data collected from the purified and etched SWNTs.<sup>95</sup>

MWNTs could also be low-cost, high-performance anode materials for rechargeable lithium-ion batteries since they show an excellent reversible capacity and cycle ability during lithium insertion and extraction.<sup>96</sup>

## 5.2.2 Modelling<sup>97,98</sup>

As stated earlier CNTs could be used in Li ion batteries. Lithium can intercalate in CNTs but it is not always clear how lithium ions get inside the SWNTs or SWNT bundles and if the inside or outside of the tubes is preferable for lithium. These questions can be answered by theoretical calculations. This is what we call modelling.

Because of the large size of CNTs *ab initio* theoretical calculations of the full system are impractical. For that reason it is possible to use a good model with fewer atoms, which mimics the system quite well. With nanotubes the insertion of lithium takes place through the hexagonal rings in the tube wall. In a model, this can be simplified by considering only a benzene molecule. Insertion of the Li ions takes place through the centre of this benzene ring. However, not only hexagons (6R) are considered, but also pentagons (5R), heptagons (7R) and octagons (8R), which are common defects within CNTs.

The initial calculations on these simple models have been carried out using HF, MP2 and DFT-B3LYP methods using a wide range of basis sets from minimal to extended. For the reliability of the models, lithium ion intercalation into two different zigzag nanotubes with different length has been studied. The electronic binding energies of Li and the benzene ring at different levels of theory are summarised

in Table 5-2. Geometries are optimised at each level of theory. Energy values obtained from the highest level of calculations (6-311++G\*\* basis sets) are in good agreement with the experimental binding energy of 1.70 eV.

methods	$\Delta E^a$ , eV	R(LiX), Å
HF/STO-3G	-3.69	1.713
HF/3-21G	-1.90	1.949
HF/6-31G*	-1.76	1.942
MP2/STO-3G	-3.97	1.697
MP2/3-21G	-1.95	1.928
MP2/6-31G*	-1.90	1.921
DFT-B3LYP/STO-3G	-3.42	1.732
DFT-B3LYP/3-21G	-2.02	1.883
DFT-B3LYP/6-31G*	-1.84	1.880
HF/6-311++G**	-1.66	1.885
MP2/6-311++G**	-1.67	1.868
DFT-B3LYP/6-311++G**	-1.67	1.841

$$^a \Delta E = E(\text{Li}^+ @ 6R) - E(6R) - E(\text{Li}^+).$$

Table 5-2: Binding energies and equilibrium distances between  $\text{Li}^+$  and the centre of the benzene ring.<sup>98</sup>

From studies on Li-intercalated carbon nanotube ropes it was found that little deformation of the structure is present as a result of intercalation. So, in our model the C-C distances are kept fixed at the normal 1.4 Å for nanotubes. Then the energy associated with moving the lithium ion along an axis perpendicular to the benzene ring is measured. This energy is showed for the different models in Figure 5-18. It can be seen that there is a minimum at 1.8 Å from the centre of the hexagon. This is the equilibrium distance. At the centre of the ring, the energy is at a maximum. The lithium ion would have to cross a high energy barrier to enter the nanotube.

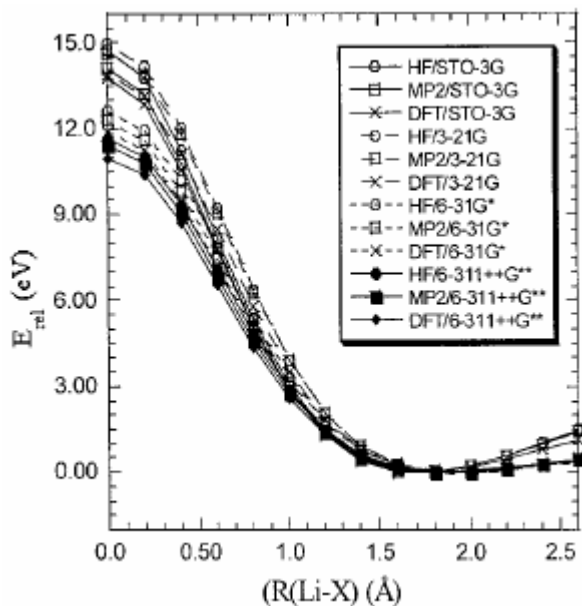


Figure 5-12: Variation of energies by moving  $\text{Li}^+$  from 2.6 Å to the centre of the benzene ring.<sup>98</sup>

The same can be done with the other three rings. The intercalation energy is lowered drastically from 24 eV to 2 eV as the ring size increases from pentagon to octagon. This is showed in Figure 5-13. It is now supposed that intercalation of lithium in nanotubes becomes easier when the structural defects are more present, because of the greater ring sizes and thus lower energy barriers. The equilibrium distance of 1.8 Å seems independent of the ring size.

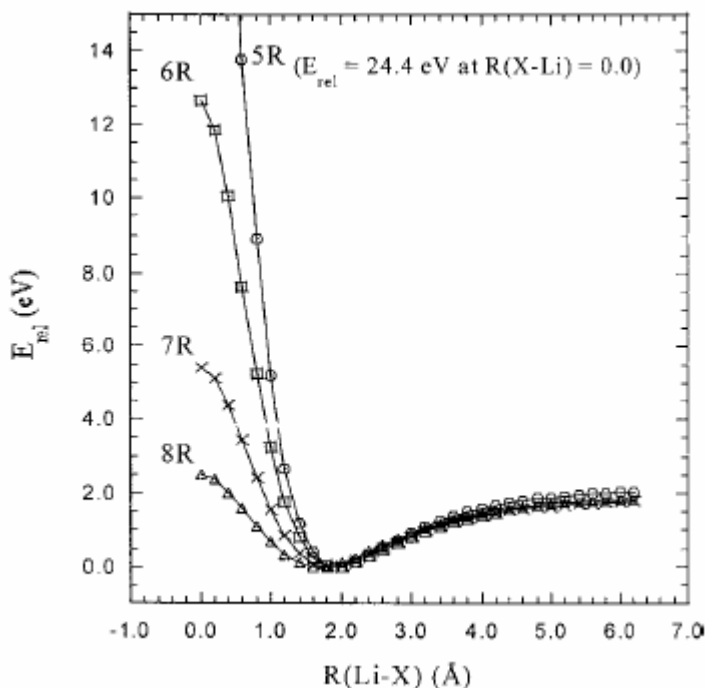


Figure 5-13: Variation of MP2/6-31G\* energies by moving  $\text{Li}^+$  to the centre of the 5-, 6-, 7- and 8-rings.<sup>98</sup>

Additional calculations have been performed on ring geometries that are allowed to expand. In this case the energy barriers are significantly lower, especially for the smaller rings. So, allowing the rings to deform facilitates the passage.

However, one single ring is only an approximation for the potential experienced by the ion outside of the nanotube. For an approximation inside the tube, two 6-membered rings with a lithium ion in between could be considered. This can be seen in Figure 5-14a. The distance  $L$  gives the diameter of the tube or the interlayer distance in a bundle of nanotubes. With  $L = 4 \text{ \AA}$ , all three methods indicate a situation in which the ion prefers its equilibrium position in the centre of the tube. At longer  $L$ , the lithium ion crosses two minima around  $2 \text{ \AA}$  from each ring. A small barrier is encountered in the middle of the two rings. This barrier height increases with the distance  $L$  (Figure 5-14b). The difficulty of moving the lithium ion within the tubes seems to depend strongly on the diameters of the tubes.

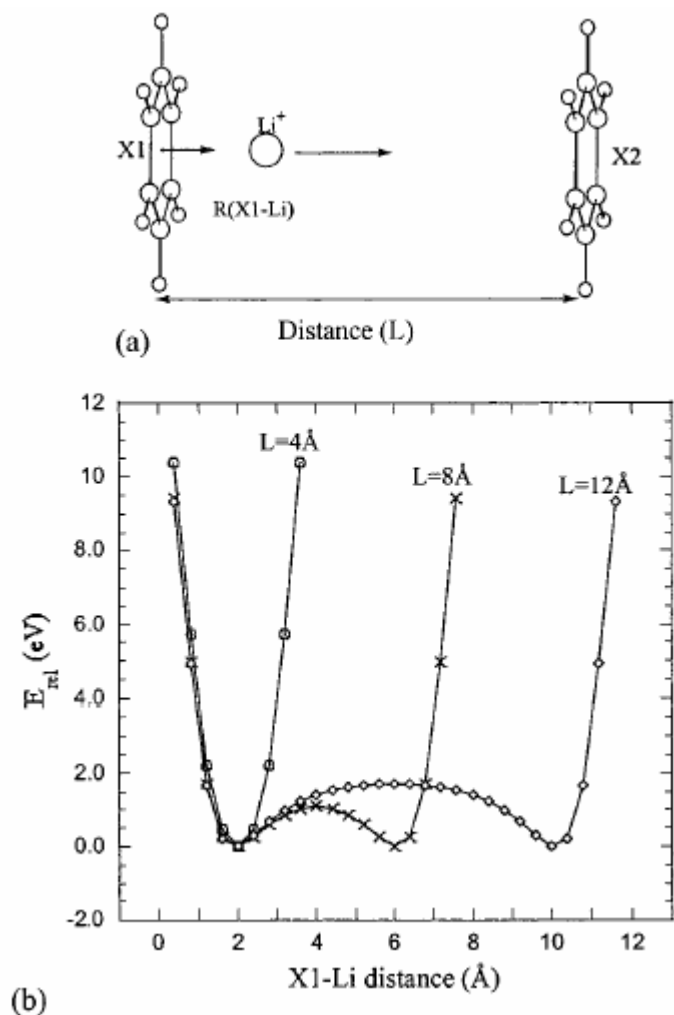


Figure 5-14: (a) A hexagon model where  $L$  is the distance between 2 benzene rings. (b) Variation of energies (MP2/6-31G\*) by moving  $\text{Li}^+$  between two benzene rings<sup>98</sup>.

The length of the tube is not expected to be an important factor. Comparing two tubes with different lengths but same diameter can test this assumption. For this test two zigzag nanotubes of different length are taken. For the two different tubes there are nearly no differences in energy with approach and intercalation of the lithium ion. However, the height of the energy barrier inside the tube depends on the length of the tube. The longest tube has the lowest energy barrier inside the tube.

From the model and the actual calculations it is suggested that the lithium ion prefers positions as well inside as outside the tube. It is possible now to look at the several combinations of inside and outside positions for two lithium ions in a nanotube. The electronic binding energy of the two ions strongly depends on the positions of those ions. The least stable state is found when both ions are inside the tube. The  $\Delta E$  value then is  $-1.80$  eV and the distance from the wall is  $1.934$  Å. The stability increases if one ion is moved outside the tube. The most stable state is the situation in which both ions are outside the tube with a  $\Delta E$  value of  $-2.96$  eV. This state is even more stable than the single ion system. The different possible states with their binding energies are given in Figure 5-15.

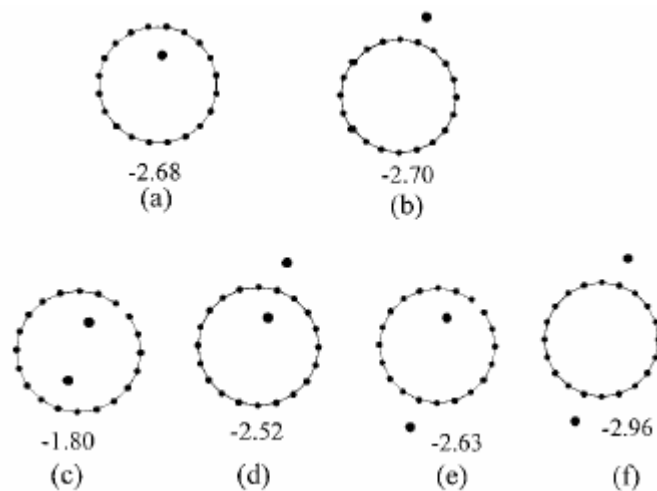


Figure 5-15: HF/3-21G optimised structures and binding energies (in eV) of different isomers of one  $\text{Li}^+$  (a and b) and two  $\text{Li}^+$  ions at a nanotube.<sup>98</sup>

Another situation that can be modelled is the situation of multiple lithium ions in MWNTs. This can be seen in Figure 5-16a. In Figure 5-16b the energy of moving Li1 to the centre of the middle ring and the position of Li2 compared to X2 are shown. What happens is that Li1 has its equilibrium state at 2 Å from X1. If we move Li1 towards X2 the energy increases. Li2 is at that moment in its equilibrium state compared to X2. When Li1 approaches X2 further, Li2 shifts sharply to its second preferred position at about 2 Å from X3. The energy obtained by moving Li1 towards X2 now decreases suddenly but increases to a maximum by moving further towards X2. The barrier height for Li1 is 2.3 eV and this is double that of the two benzene rings and one lithium ion model.

The last case that could be modelled is that of an opened tube. There are three possible paths for insertion: along the central axis of the tube or at 2 Å from the tube wall inside or outside the tube. The barrier height for the path along the central axis is significantly lower than for the other pathways. So, it seems that the lithium ions enter the tube through the central axis and then may spread inside the tube close to 2 Å from the tube wall.

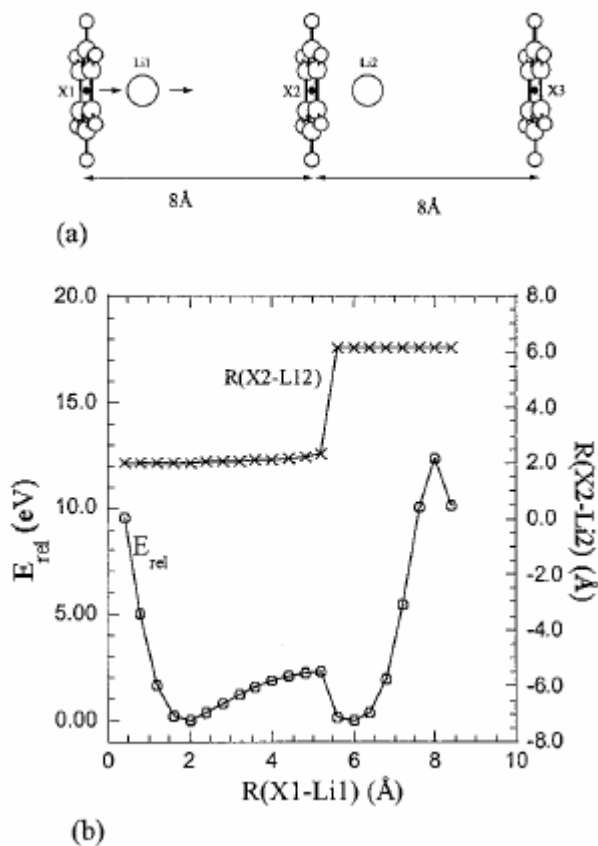


Figure 5-16: (a) Three benzene rings and two  $Li^+$  ions model. (b) Variation of energies (HF/6-31G\*) and distance between Li2 and X2 by moving Li1 from the centre of the leftmost ring (X1).<sup>98</sup>

For the application of CNTs in Li-rechargeable batteries it can be concluded that the barrier height of the intercalation process is a crucial factor in battery activity. Insertion of lithium ions through the sidewall of the nanotubes seems energetically unfavourable unless there are structural defects. Release of the ion during discharge process has to cross a very high barrier. This depends on the size of the rings. The electronic binding energies of the lithium ion at its equilibrium distance also decrease as the ring size increases. Thus, it seems that ions outside the tubes may more easily take part in battery activities. For the situation of two lithium ions, the binding energy strongly depends on the position of the lithium ions compared to each other. The most stable configuration is the one where both the ions are outside the tube.

## 5.3 Gas phase intercalation of hydrogen

### 5.3.1 Experimental studies

Gas phase intercalation of hydrogen in CNTs concerns the adsorption of  $H_2$ , called physisorption instead of chemisorption (involving  $H^+$  and chemical bonds). This adsorption of  $H_2$  (other gases are possible too) on the surface of CNTs is a consequence of the field force at the surface of the solid, called the adsorbent, which attracts the molecules of the gas or vapour, called adsorbate. The forces of attraction emanating from a solid can be either physical (Van der Waals) or chemical (thus chemisorption, involving the electrochemical storage of hydrogen). This section is about the storage due to the physical forces.

Carbon nanotubes have attracted considerable interest due to several reports of high hydrogen storage capacities at room temperatures, even higher than the goals set for vehicular storage by the Department Of Energy (being an  $H_2$ -storage capacity of 6.5 wt% and 62 kg  $H_2/m^3$ ). However, conflicting reports indicate that room temperature storage capacities do not exceed  $\sim 0$  wt%. Reporting capacities range from 0 to 60 wt%. Several reports on hydrogen storage exist, which can be divided according to their results. The most important results found are:

1. Hydrogen storage with a H/C ratio larger than 2, thought to be incorrect ( $> 14$  wt%). For example, a storage capacity of 67 wt% in GNFs (see Table 5-1) is reported, but this seems highly irrational because this corresponds to an average of about 24 hydrogen atoms for each carbon atom;
2. Hydrogen storage consistent with expectations based on findings for activated and other, conventional high-surface area carbons (0 -2 wt%);
3. Hydrogen storage results are in the intermediate range and are not obviously incorrect (2-14 wt%).<sup>99</sup>

There are several possibilities for the hydrogen to be stored in the CNT samples. For hydrogen storage in closed CNTs the structure has two possible sites: inside the tubes and in the interstitial sites between the tube array (Figure 5-17). In case of a long SWCNT closed with fullerene-like end caps, the hydrogen can only get access to the tube interior via the hexagons of the graphite-like tube wall. An opened tube with removed caps gives an easier access for the hydrogen molecules to the tube. Typically, the tubes are very long and therefore a good diffusivity of the hydrogen inside the tube will be required in order to fill the whole tube volume. Cutting the rope in shorter pieces may therefore help to improve hydrogen storage and its kinetics.<sup>100</sup>

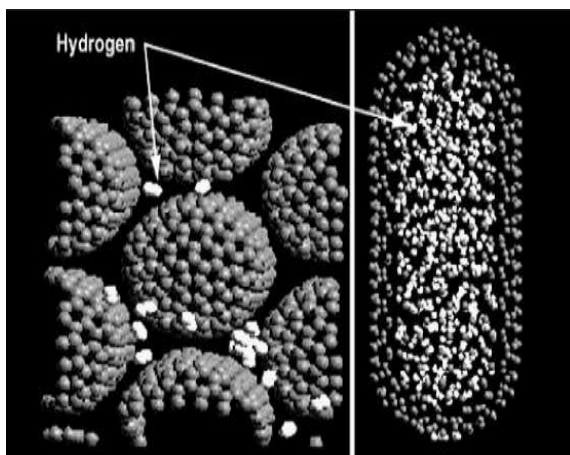


Figure 5-17: Schematic representation showing potential sites for hydrogen adsorption within a nanotubes - bundle: (left) hydrogen atoms occupying the interstitial spaces between the tubes, and (right) hydrogen atoms inside the tube interior.<sup>101</sup>

Mainly, three different techniques are applied to study the hydrogen storage in solids: (1) the volumetric method, (2) the gravimetric method and (3) thermal desorption spectroscopy.

(1) The volumetric method measures the pressure drop owing to hydrogen adsorption after applying a hydrogen pressure to the specimen, contained in a constant volume. Similarly the pressure increase due to desorption can be measured. For good accuracy and reliable results, this method requires typically specimen masses of 500 mg or higher. Leakage or temperature instability of the apparatus may give rise to large experimental errors. The advantage of this technique is that both adsorption and desorption can be measured.

(2) The gravimetric method measures the weight change of the specimen due to absorption or desorption of hydrogen. A high accuracy can be achieved even at sample masses of 10 mg. However, this technique is sensitive to all gasses adsorbed or desorbed since it is only based on weighing.

(3) Thermal desorption spectroscopy (TDS) measures only the hydrogen desorption in high vacuum utilising mass spectrometry. This method is selective and highly sensitive, which can be improved by using deuterium-loaded specimens. In this case no disturbing background from water or other hydrogen containing adsorbents occurs.<sup>100</sup>

Table 5-3 shows some of the reported storage capacities, up to 2002:

Material	Density wt%	Temp (K)	Pressure (MPa)	Reference	Year
GNFs (herring bone)	67.55	RT	11.35	Chambers	1998
GNFs (platelet)	53.68	RT	11.35	Chambers	1998
Li-MWNTs	20	~473-673	0.1	Chen	1999
K-MWNTs	14	< 313	0.1	Chen	1999
GNFs (tubular)	11.26	RT	11.35	Chambers	1998
CNFs	~10	RT	10.1	Fan	1999
Li/K-GNTs (SWNT)	~10	RT	8-12	Gupta	2000
GNFs	~10	RT	8-12	Gupta	2000
SWNT (lo purity)	5-10	273	0.04	Dillon	1997
SWNT (hi purity)	8.25	80	7.18	Ye	1999
CN nanobells	8	573	0.1	Bai	2001
Nano graphite	7.4	RT	1	Orimo	2000
SWNT (hi purity + Ti alloy)	6-7	~300-700	0.07	Dillon	2000
GNFs	6.5	RT	~12	Browning	2000
CNFs	~5	RT	10.1	Cheng	2000
MWNTs	~5	RT	~10	Zhu	2000
SWNT (hi purity + Ti alloy)	3.5-4.5	~300-600	0.07	Dillon	1999
SWNT (50% purity)	4.2	RT	10.1	Liu	1999
Li-MWNTs	~2.5	~473-673	0.1	Yang	2000
SWNT (50% purity)	~2	RT	echem	Nutzenadel	1999
K-MWNTs	~1.8	< 313	0.1	Yang	2000
(9,9) array	1.8	77	10	Wang	1999
MWNTs	< 1	RT	echem	Beguín	2000
CNF	0.1-0.7	RT	0.1-10.5	Poirier	2001
(9,9) array	0.5	RT	10	Wang	1999
SWNTs	~0.1	300-520	0.1	Hirscher	2000
Various	< 0.1	RT	3.5	Tibbets	2001
SWNT (+ Ti alloy)	0	RT	0.08	Hirscher	2001

Table 5-3: Overview of reported storage capacities of hydrogen in carbon nanotubes, up to 2002, of which most at room temperature.<sup>99</sup>

None of these experimental results have been confirmed by independent research groups. Obtaining activated CNT hydrogen storage materials with highly reproducible adsorption capacities has not yet been achieved. A possible reason is that hydrogen storage is only optimised for a very specific and narrow distribution of CNTs of distinct types and diameters. Although theoretical calculations predict that a range of 4-14 wt% hydrogen adsorption in carbon nanotubes is possible, they do not clearly distinguish between chemisorption and physisorption. Chemisorption (the covalent bonding of hydrogen) would require a high temperature and high activation energy for hydrogen release, whereas any practical fuel cell application would require low adsorption and desorption energies.<sup>101</sup>

Work by *Liu et al.* indicates that SWNTs are highly promising for H<sub>2</sub> adsorption, even at room temperature. They measured the H<sub>2</sub> storage capacity of SWNTs synthesised by a hydrogen arc-discharge method, with a relatively large sample quantity (about 500 mg) at ambient temperature under a modestly high pressure, which was soaked in hydrochloric acid and then heat-treated in vacuum. A H<sub>2</sub> uptake of 4.2 wt%, which corresponds to a H/C atom ratio of 0.52, was obtained by these SWNTs with an estimated purity of 50 to 60 wt%. Also, 78.3 % of the adsorbed hydrogen (3.3 wt%) could be released under ambient pressure at room temperature, while the release of the residual stored hydrogen (0.9 wt%) required some heating of the sample. Furthermore, they found that after four cycles of adsorption/desorption, the H<sub>2</sub> uptake capacity of the SWNTs remained unchanged and that less than 1 wt% could be stored at pressures lower than 5 MPa. The researchers argued that this relatively high H<sub>2</sub> adsorption capacity of their SWNTs could be related to their larger mean diameter of  $1.85 \pm 0.05$  nm, while typical SWNT diameters are in the range of 1.2 to 1.4 nm.<sup>102</sup>

Careful work at NREL (National Renewable Energy Laboratory) by *Dillon et al.* indicates a maximum capacity for adsorption of hydrogen on SWNTs is  $\sim 8$  wt%. Samples displaying this maximum value were prepared by sonicating purified SWNTs in a dilute nitric acid solution with a high-energy probe. In this process SWNTs are cut into shorter segments and this introduces a Ti<sub>6</sub>Al<sub>4</sub>V alloy due to the disintegration of the ultrasonic probe. The hydrogen adsorption on many of the NREL samples can be explained fully by adsorption on the incorporated alloy. However, one-half of the samples show capacities that are too high to be explained by the presence of the alloy alone. Assuming that the alloy in the SWNT sample behaved like the pure probe-generated alloy sample of Ti-6Al-4V, the hydrogen uptake on the SWNT fraction still reached  $\sim 8$  wt%. Cross-calibration of the experimental apparatuses with three different standards establish the validity of the measurements, and repeated measurements on a given sample yield reproducible results, but nominally similar sample preparation procedures do not repeatedly produce samples that exhibit the same hydrogen storage capacities. A possible explanation is that the degree of tube cutting, and how, where and in what form the metal particles are incorporated can vary dramatically even if identical sonication parameters are employed. Earlier, in 1997, they found that the desorption of hydrogen fitted first order kinetics and the activation energy for desorption was measured to be 19.6 kJ/mol. Also, adsorption measurements on samples having differing distributions indicate a link between SWNT size and type and hydrogen capacity. More recently, they developed a controlled dry cutting technique that does not employ ultrasonication (and so does not simultaneously incorporate a metal hydride alloy). Transmission electron microscopy analyses and Raman spectroscopy showed that significant cutting occurred without extensive damage to the SWNTs.<sup>99</sup>

### 5.3.2 Modelling

Gas phase intercalation of hydrogen in CNTs is mainly being analysed by grand canonical ensemble Monte Carlo simulations (GCEMC) and molecular mechanics (MM) classical algorithms, in which only nonbonding interactions, mostly being described by the Lennard-Jones potential, are included in the potential functions.<sup>103</sup> In a simulation loop, the motion of hydrogen molecules in a given pore volume for a fixed temperature  $T$  and a chemical potential  $\mu$  is calculated. The carbon pore is built up by  $M$  carbon atoms being located at the surface of any desired pore geometry. The most commonly used potentials  $U(r)$  for the hydrogen-hydrogen and hydrogen-carbon interaction energy are described below. The total potential energy of a particular hydrogen molecule is then given by summing up all interaction energies between neighbouring hydrogen molecules and pore wall carbon atoms.

During the simulation, the particle number  $N$  within the pore fluctuates owing to particle displacement, creation and destruction steps, which are executed with equal frequency. In a creation step, the position of the new particle is chosen randomly within pore volume  $V$  and its potential energy  $U$  is calculated. This creation step is accepted with the probability<sup>104</sup>:

$$P = \exp\left(-\frac{U - \mu}{k_B T}\right) \frac{V}{N + 1} \quad (1.7)$$

Analogous destruction, respectively displacement steps are accepted with the probability:

$$P = \exp\left(-\frac{U - \mu}{k_B T}\right) \frac{V}{N} \quad (1.8)$$

$$P = \exp\left(-\frac{U_{H-H} - U_{H-C}}{k_B T}\right) \quad (1.9)$$

A simple and ideal model of nanotube materials consists of parallel SWNTs with equal diameters  $D$  on a two-dimensional triangular lattice where the minimal distance between the nanotube walls is equal to  $d$ . In the cylindrical wall obtained by rolling up a basal graphite plane, the carbon atoms form a two-dimensional hexagonal lattice where each carbon atom has three nearest neighbours at a distance  $c \approx 1.42 \text{ \AA}$ . The diameter  $D$  of a nanotube is equal to  $D = c = \sqrt{3} / \sin(\pi/n)$  where  $n$  is the number of hexagons along the tube perimeter. The pair wise interaction energy between two hydrogen molecules is mostly calculated by the Lennard-Jones potential (1.3). In addition to this pair potential, the hydrogen molecules interact by a quadrupole-quadrupole interaction which is taken into account by the Coulomb interactions of effective electric charges: two charge  $q = 0.4829e$  located on the protons and one charge  $-2q$  at the centre of mass. The interaction between hydrogen molecules and carbon atoms in the walls commonly uses the Lennard-Jones potential too.

Due to the small mass of hydrogen and the confinement of the molecules inside the nanotubes and the interstitial space between the tubes, the quantum effects are expected to contribute significantly to the adsorption process. Some investigators take these effects into account in simulations by the path-integral Monte Carlo method. But in the domain of temperature above 70 K considered in most studies, the use of a Feynman-Hibbs effective potential which estimates the quantum effects exactly to the order of  $\hbar^2$  is sufficient (the dimensionless parameter giving the magnitude of the quantum effects,  $\hbar^2 / (m_r \sigma_{H-H}^2 k_B T)$  with  $m_r$  the reduced mass of a pair of hydrogen molecules and  $k_B$  the Boltzmann constant, is equal to  $\sim 0.07$  at  $T = 70 \text{ K}$ ). The expression for the Feynman-Hibbs effective potential is<sup>105</sup>:

$$U_{FH}(r) = U_{LJ}(r) + \frac{\hbar^2}{24m_r k_B T} \left( \frac{\partial^2 U_{LJ}(r)}{\partial r^2} + \frac{2}{r} \frac{\partial U_{LJ}(r)}{\partial r} \right) \quad (1.10)$$

with  $U_{LJ}(r)$  given by (1.3).

The potentials described above are not the only potentials that are used to model the  $H_2$ - $H_2$  and  $H_2$ -C interaction energy. An alternative potential for the  $H_2$ - $H_2$  interaction energy is the Silvera-Goldman potential, which is a semi-empirical pair potential  $U_P(r)$  that includes a pair-wise effective three-body term. This potential is given by<sup>106</sup>:

$$\begin{aligned} U_P(r) &= U_{rep}(r) + U_{att}(r) \\ &= \exp(\alpha - \beta r - \gamma r^2) - \left( \frac{C_6}{r^6} + \frac{C_8}{r^8} + \frac{C_{10}}{r^{10}} \right) f_C(r) \end{aligned} \quad (1.11)$$

$$\begin{aligned} \text{with: } f_C(r) &= \exp\left[-\left(\frac{1.28r_m}{r} - 1\right)^2\right], \quad r < 1.28r_m \\ &= 1.0, \quad r > 1.28r_m \end{aligned} \quad (1.12)$$

and  $r_m$  being the position of the minimum of  $U_P(r)$ .

An alternative potential for the hydrogen-nanotube interaction is a model by the Crowell-Brown potential for hydrogen interacting with carbon atoms in an oriented graphitic sheet. This hydrogen-carbon potential is given by<sup>107</sup>:

$$U(r, \phi) = \frac{E_H E_C P_H P_{\parallel} (1 + P_{\perp} / 2P_{\parallel}) \sigma_{C-H}^6}{(E_C + E_H) r^{12}} - \frac{E_H E_C P_H [3(P_{\parallel} - P_{\perp}) \cos^2 \phi + (P_{\parallel} + 5P_{\perp})]}{4(E_H + E_C) r^6} \quad (1.13)$$

where  $r$  is the distance from a carbon atom in the tube, to the hydrogen molecule (which could be either inside or outside the tube), and  $\phi$  is the angle between the axis normal to the tube surface and a line connecting the hydrogen and carbon atom.  $E_H$  and  $E_C$  are the atomic energies for hydrogen and carbon respectively,  $P_{\parallel}$  and  $P_{\perp}$  are atomic polarisabilities, where the subscripts denote orientations parallel to and perpendicular to the graphite  $c$  axis and  $P_H$  is the polarisability of hydrogen.<sup>107</sup> A thorough description of these potentials can be found in the referred articles.

Apart from the hydrogen-hydrogen and hydrogen-carbon interaction energy, several other features can be modelled in different ways, leading to differences of adsorption amounts in published articles. These differences are mainly attributed to different models/values for:

- single- or multi-walled carbon nanotubes;
- open or closed tubes, which are important for the adsorption phenomenon (open tubes enable gas adsorption both inside and outside the tubes whereas closed tubes do not);
- the reactive surface of the adsorbent material considered. This value is dependent on the distance considered between consecutive tubes, the so-called inter-tube spacing;
- the sampling method used in simulations;
- the gas thermodynamic conditions (in particular, the adsorption is temperature-dependent due to the high attractive forces at 80 K and high thermal effects occurring at room temperature at which the hydrogen molecules dispose an important kinetic energy);
- the adsorbent configurations (including the values of the tube diameters, the tube lengths and the inter-tube spacing) that permit the hydrogen gas either to move in a large adsorption volume or just to be confined in the interstitial pores;<sup>108</sup>

In spite of the use of different calculation methods, the following conclusions could be reached:

- adsorption of hydrogen does possibly occur in sites of different binding energy in SWNTs. It is suggested that the outer surface of SWNT ropes in the simulation of physisorption is important, not only for geometrical reasons (high surface area), but also for energetic reasons;
- the inner-tube cavity has high adsorption potential for hydrogen, compared with the planar surface and slit-pores of similar size;
- interstitial adsorption constitutes a significant fraction of the total amount adsorbed hydrogen for a tube of larger diameter such as the (18, 18) tube array (2.44 nm). By comparison, in the smaller interstices of the (9,9) tube array, adsorption is negligible due to the quantum effect. Interstitial adsorption accounts for at most 14 % of the total adsorption for the (18, 18) tube array at 77 K;<sup>107</sup>
- the packing geometry of the SWNTs plays an important role in hydrogen adsorption;

Most of the performed simulations do not confirm the high hydrogen uptake capacity obtained experimentally for similar systems of SWNTs. However, *Williams et al.* reported the results of Monte Carlo simulations for the physisorption of H<sub>2</sub> in finite-diameter ropes of parallel SWNTs is consistent with the experimental results obtained by *Ye et al.* at 77 K. Their results show that the maximum gravimetric adsorption capacity of hydrogen onto an isolated (10, 10) nanotube can reach 9.6 wt% under cryogenic temperatures (77K) and a pressure of 10 MPa. However, their results cannot explain the hydrogen adsorption at room temperature.<sup>109,110</sup>

*Levesque et al.* have studied hydrogen storage in CNTs by Monte Carlo simulations in the pressure domain from 0.1 to 20 MPa at temperatures of 77, 150 and 293 K. The hydrogen-hydrogen and hydrogen-carbon interaction energies were both described by with (1.3)  $\epsilon_{H-H} = 36.7$  K,  $\sigma_{H-H} = 2.958$  Å and  $\epsilon_{H-C} = 32.05$  K,  $\sigma_{H-C} = 3.18$  Å respectively. The quantum effects are modelled by (1.10).

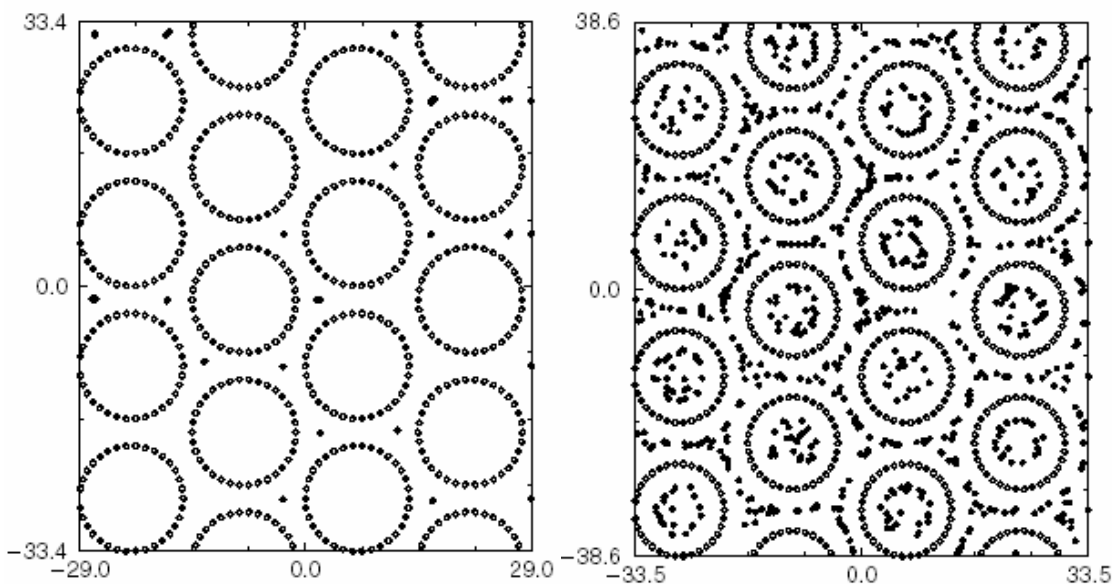


Figure 5-18: Projection on the  $xz$ -plane of adsorbed hydrogen molecules at 10 MPa and 293K in a triangular lattice of closed and opened nanotubes respectively with diameter  $D = 13.3 \text{ \AA}$  with  $d = 3.4 \text{ \AA}$  (left) and  $D = d = 6 \text{ \AA}$  (right). The open circles give the locations of nanotube walls, the black dots those of hydrogen molecules. The lengths of the sides of the simulation cell are in angstroms.<sup>105</sup>

Figure 5-18 presents the projections of typical configurations of adsorbed hydrogen molecules on the  $xz$ -plane. Figure 5-18(left) shows the small extension of the domain where the molecules can be inserted when the nanotubes have closed ends and are close packed; Figure 5-18(right) shows that the contribution of the interstitial space and external surface of nanotubes to the adsorption process is similar to that due to the internal volumes and surfaces of nanotubes, from which it can be concluded that the opening of CNTs is essential for hydrogen adsorption. In the domain of temperatures and pressures considered, the values  $D = 13.3 \text{ \AA}$  and  $d = 6 \text{ \AA}$  correspond to adsorption close to the best possible properties. By contrast, for  $d = 3.4 \text{ \AA}$ , the adsorption capacity of the nanotube material is low, but it is useful to notice that this value of the distance between nanotube walls could be that existing in the ropes of synthesised nanotubes. Furthermore, the adsorption at temperatures 150 and 293 K was several times less than the observed uptake at 77 K.<sup>105</sup>

*Dodziuk et al.* have carried out molecular mechanics calculations and molecular dynamics simulations for systems consisting of (5, 5) armchair, (9, 0) zigzag and (7, 3) chiral nanotubes. Contrary to many other calculations in which the condition of the nanotubes rigidity is imposed and hydrogen molecules are treated as spheres, they used both CVFF (consistent valence force field) parameterisations and ESFF (extensible systematic force field) parameterisations, which uses a rule based algorithm to determine a potential parameter set for a given system. These force fields do not imply such limitations. These calculations indicate that there is no essential difference among armchair, zigzag and chiral nanotubes as concerns their ability to host hydrogen molecules inside them. Furthermore, it is concluded that the total amount of hydrogen inside the nanotubes is very small and  $H_2$  molecules are not being adsorbed at higher temperatures. This result agrees with several other reports. From this, it is concluded that the literature reports on the very high hydrogen uptake cannot be obtained by physisorption process only.<sup>103</sup>

## 5.4 Supercapacitors

### 5.4.1 Introduction

In the future, supercapacitors might become an excellent means of certain kinds of energy storage. These electrochemical capacitors have a long durability (over  $10^6$  cycles), don't suffer from short circuit conditions, have a complete discharge and possess a high power density. Loading of a supercap can be performed at high current densities, which decreases the loading time needed. However, their energy density is lower than for conventional batteries, which is a possible drawback for possible applications. Typical electrochemical accumulators, in which compounds only take place in redox reactions, cannot fulfil these good characteristics that electrochemical capacitors have. Supercapacitors have already been applied in small-scale energy storage devices, such as in memory backup devices. Now the capability of supercapacitors with a high power density is increasing, potential applications extend to hybrid battery/supercapacitor systems.<sup>111</sup>

Carbon in general, and especially nanotubes, form an attractive material for electrochemical applications as they have a large active surface area. In addition, carbon is a relatively cheap, low density, environmentally friendly and highly polarisable material which makes application even more attractive.<sup>112</sup>

At first this section deals with basic processes in supercapacitors. Then, the determination of supercapacitor properties is explained briefly. Thereafter, supercapacitors based on CNTs are investigated after which attention is given to the modification of CNTs in supercapacitors to improve their properties.

### 5.4.2 Basic principles of supercapacitors

The basic principle of energy storage in a supercapacitor is based on creating a charge-separated state in an electrochemical double layer. In this case, energy storage is based on the separation of charges in the double layer across the electrode/electrolyte interface. The positive electrode is electron deficient whereas the negative electrode contains a surplus of electrons. The energy (W) stored in a capacitor as a function of the voltage applied (U) and the capacity (C) is equal to:  $W = \frac{CU^2}{2}$ .

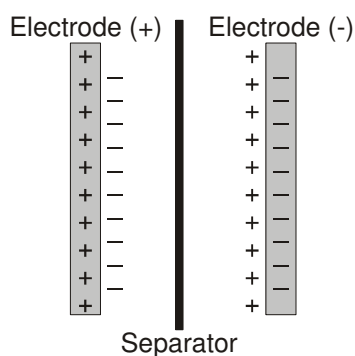


Figure 5-19: Scheme of an electrochemical capacitor.

The electrodes of a supercapacitor must be electrochemically stable, which is the case for chemically unmodified carbon. The decomposition voltage of the electrolyte determines the maximum operating voltage of a supercapacitor. For the generation of high voltages, aprotic electrolytes with a decomposition range between 3 and 5 V should be used. However, these liquids only have a fraction of the conductivity that water has. In addition, the use of an aprotic electrolyte has technological,

economical and safety barriers.<sup>112</sup> The final electrolyte choice depends on the demanded specific power and energy values.

Electrochemical capacitors based on carbon are of two different types depending on the type of energy storage. The first type is the electrical double layer capacitor (EDLC) where only a pure electrostatic attraction between ions and the charged surface of an electrode takes place. The second type is a supercapacitor (SC), which is additionally based on faradaic supercapacitance reactions. The total capacitance  $C$  is determined by the series capacitances of the anode ( $C_A$ ) and cathode ( $C_C$ ) according

to the equation<sup>112</sup>:

$$\frac{1}{C} = \frac{1}{C_A} + \frac{1}{C_C}.$$

In the EDLC, the contact between the electrode surface and the electrolyte plays an important role and determines the amount of charge stored. The capacitance  $C$  is proportional to the surface area  $S$  and the permittivity  $\epsilon$  of the electrolyte and reciprocally dependent on the distance of charge separation:

$C = \frac{S\epsilon}{d}$ . In practice, the surface area determined by gas adsorption differs from the active surface area

available for charged species. When ions are solvated by water molecules, their mean diameter is approximately 15Å. This explains the need for a relatively large pore size of the electrode material for good interaction of ions with the electrode. Thermal treatment of the electrodes results in significant alteration of the pore size distribution and thus to enhanced interaction.<sup>1</sup> Increasing the capacitance values 10 to 100 times is possible by using pseudocapacitance effects. These depend on the surface functionality of carbon and/or on the presence of electro-active species.<sup>112</sup>

As said before, in supercapacitors faradaic reactions similar to processes in accumulators occur. Pseudocapacitances arise when the charge  $q$ , required for the progression of an electrode process, is a continuously changing function of potential  $U$ . These pseudocapacitance effects, for example electrosorption of  $H$  or metal ad-atoms and redox reactions of electroactive species, strongly depend on the chemical affinity of carbon materials to the ions sorbed on the electrode surface.<sup>112</sup>

An ideal double layer capacitance results in ideally rectangular shaped cyclovoltammetry diagrams. This phenomenon is ideal if the current density is independent of the potential applied and if this effect is purely electrostatic of nature. Due to redox peaks, pseudocapacitances result in deviations from this ideal shape as is shown in Figure 5-20.

EDCL capacitors can be represented in an equivalent electrical circuit as is shown in Figure 5-21. This circuit consists of a capacitance  $C$ , a parallel resistance  $R_F$  which is responsible for the self-discharge, an inductance  $L$  and an equivalent series resistance  $R_S$  that models the internal resistance. A maximum value of  $C$  and a minimum value of  $R_S$  result in a high value for the power density and energy value.

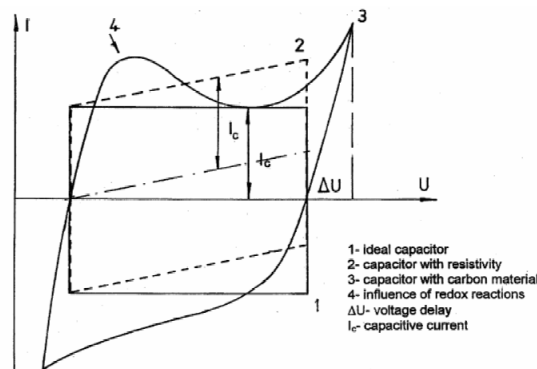


Figure 5-20: Typical charge/discharge voltammetry characteristics of an electrochemical capacitor<sup>112</sup>

The time constant for the charging and discharging cycles is equal to  $R_S C$ , while the self-discharge time constant is equal to  $R_F C$ . In order to minimise self-discharge the value for  $R_F$  should be as large as possible.

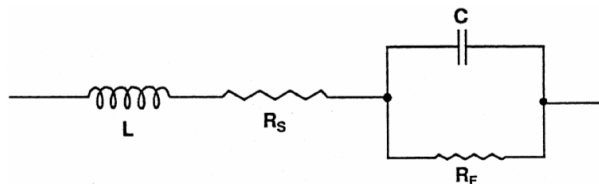


Figure 5-21 Equivalent circuit for a real ECDL capacitor

### 5.4.3 Determination of supercapacitor properties

Key techniques to determine capacities are cyclic voltammetry, galvanostatic charge/discharge, external resistor discharge and impedance spectroscopy. Each technique reveals other specific information about the capacitor performance. Usually, a three-electrode set-up is used for material characterisation. In the resistor discharge method, the time needed to completely discharge through a certain resistor is measured.

The term “impedance spectroscopy” implies the dependence of impedance, or a kind of ‘generalised’ resistance ( $V / I$ ), on a certain frequency. This frequency is that of the power source used. For various reasons, the current might have a phase delay with regard to the voltage. Both this phase difference as the magnitude of the impedance ( $Z$ ) play a key role in determining electrochemical mechanisms and electrode characteristics. In impedance spectroscopy, these parameters are determined as a the logarithm of the angular frequency ( $\log(\omega)$ ).<sup>113</sup>

Periodic processes, such as those in impedance spectroscopy, can be described in terms of real and imaginary parts of the parameters investigated. These complex plots, also called Cole-Cole plots, provide information about key parameters such as internal resistances and the kinetics of different processes.

### 5.4.4 Modification of CNTs

Carbon nanotubes have been proposed as electrodes for supercapacitors. Different values of capacitance mainly depend on the kind and purity of the samples. For purified nanotubes specific capacitance varies from 5 to 80 F/g. Pure carbon nanotubes have a moderate surface area (120 to 400  $m^2/g$ ) because of their highly mesoporous character. The more graphitised nanotubes show smaller values of capacitance. However, presence of defects causes an increase of ability for accumulation of charges.<sup>114</sup>

There is a great difference in capacitance between SWNTs and MWNTs. However, the many different ways of producing the nanotubes also create differences in capacitance values. This can be seen in Table 5-4. Surface groups noticeably enhance the measured capacitance value, as is the case with MWNTsCo/700°C modified by  $HNO_3$ .

	SWNTs Rice	SWNTs Rice 1650°C	MWNTs templ/800°C	MWNTs Co/700°C	MWNTs Co/900°C	MWNTsCo/700°C mod. $HNO_3$
6 mol $l^{-1}$ KOH	40	18	36	80	62	137

Table 5-4: Specific capacitances of differently produced carbon nanotubes in F/g.<sup>115</sup>

To increase the capacitance of nanotubes it is possible to increase the electrode surface area or to increase the pseudocapacitance effects obtained by addition of special oxides or electrically conducting polymers (ECP) like polypyrrole (PPy). The ECPs have the advantage of lower costs compared to oxides. Another advantage is that the pseudocapacitance effects of ECPs are quite stable.<sup>116</sup>

Charging of the electrical double layer proceeds mainly in the micropores. These micropores are just limited present in the pure CNTs. So, we have to modify them to get mesopores as well as micropores. This is possible by activation of the nanotubes by KOH. The exact mechanism of this activation by KOH is not clear yet. Both activation and coating increases the capacitance of the nanotubes.<sup>117,118</sup>

The mesoporous character of as-produced nanotubes essentially determines their electrochemical properties. For charging of the double layer a developed surface area is needed, thus the presence of micropores is necessary. With chemical activation of pure MWNTs by KOH, microporosity is introduced (Figure 5-22).

This KOH activation is performed by *Frackowiak et al.*<sup>117</sup> at 800 °C under argon flow. The KOH:C weight ratio is 4:1 during the entire process. Afterwards, the samples are washed with demineralised water.

Specific surface area is measured by nitrogen adsorption at 77 K after the samples are outgassed at 350 °C for 24 hours until pressure reaches  $10^{-6}$  mbar.

The electrodes are prepared in the form of pellets with 85 wt% nanotubular material, 5 wt% acetylene black and 10 wt% polyvinylidene fluoride. The mass of the electrodes varies from 4 to 8 mg.

Three different types of electrolytic solutions are used: aqueous 6 M KOH, aqueous 1 M H<sub>2</sub>SO<sub>4</sub> and organic 1.4 M TEABF<sub>4</sub> in acetonitrile.

Two different types of MWNTs are used. One type is obtained by decomposition of acetylene at 700 °C on cobalt (12,5 %) supported on silica (A/CoSi700). The other type is prepared by decomposition of acetylene at 600 °C on Co particles from a solid solution of cobalt oxide and magnesium oxide (A/Co<sub>x</sub>Mg<sub>(1-x)</sub>O).

The values of capacitance are estimated by voltammetry, galvanostatic charge/discharge cycling and impedance spectroscopy.

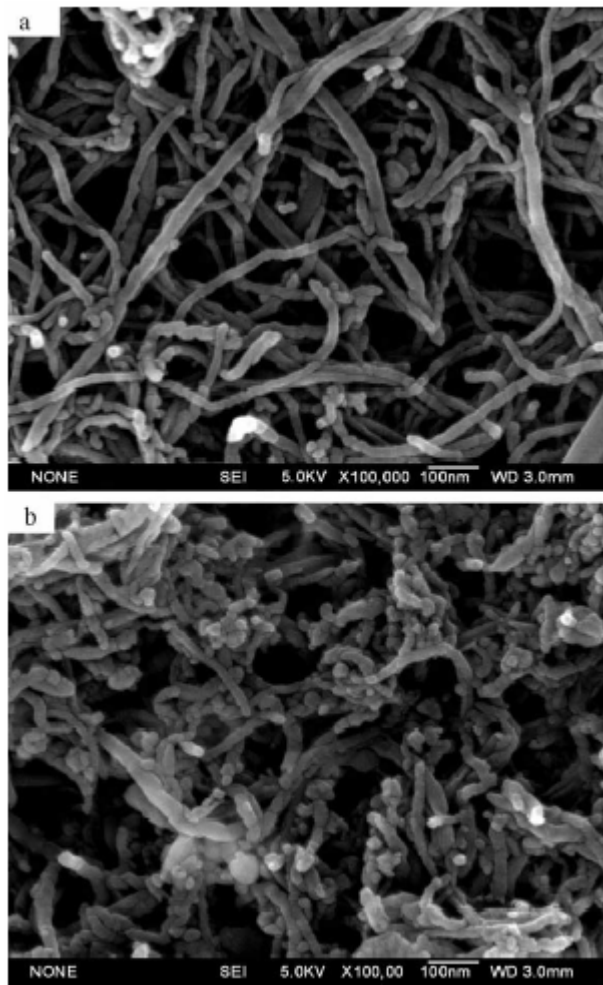


Figure 5-22: SEM images of normal CNTs (a) and activated CNTs (b).<sup>118</sup>

The specific surface of the A/CoSi700 nanotubes increased from 430 to 1035 m<sup>2</sup>/g and the micropore volume changed from nearly zero to 0.47 cm<sup>3</sup>/g after activation. For A/Co<sub>x</sub>Mg<sub>(1-x)</sub>O nanotubes the specific surface area increased from 220 to 885 m<sup>2</sup>/g and the micropore volume increased to 0.40 cm<sup>3</sup>/g from almost zero. These are significant changes. For the latter type an additional effect is that the tips are opened by KOH activation. Microporosity is now enhanced by activation, but the mesoporous character is still present because of the entanglement and presence of a central canal.

The results of the capacitances of the different nanotubes in three different electrolytes are given in Table 5-5. The capacitances for the unactivated nanotubes are between 10 and 15 F/g.

The values of capacitance were estimated by voltammetry with a scan rate of potential from 1 to 10 mV/s and galvanostatic charge/discharge cycling from 0 to 0.6 V or higher voltage limitation until 1.2 V.

electrolyte	A/CoSi700		A/Co <sub>x</sub> Mg <sub>(1-x)</sub> O	
	activated		activated	
1 M H <sub>2</sub> SO <sub>4</sub>	95 F/g		85 F/g	
6 M KOH	---		90 F/g	
1.4 M TEABF <sub>4</sub>	65 F/g		65 F/g	
	not act.	act.	not act.	act.
surface area (m <sup>2</sup> /g)	430	1035	220	885

Table 5-5: Capacitances of the activated MWNTs. The unactivated nanotubes show capacitances between 10 and 15 F/g. The surface area of the activated and unactivated nanotubes is also given.

The modification of carbon material by a specific additive providing quick pseudo-capacitance redox reactions is another way to enhance capacitance. This is possible with metal oxides, but in this case the addition of ECP is used. ECP itself has a capacitance of about 90 F/g. Pseudocapacitance effects of ECP are relatively stable. If we coat a nanotube with, for instance, polypyrrole we take the profit of the good electronic conducting properties and keep the advantage of ionic conductivity in the opened mesoporous network of the nanotube. These are perfect conditions for a supercapacitor.

Jurewicz *et al.*<sup>116</sup> took five nanotube samples, all of them made in a different way and measured the capacitance of them with and without a layer of PPy coated on the surface. The specific surface area of the nanotube materials was measured by nitrogen adsorption at 77 K. The chemical polymerisation of pyrrole on the nanotubes was performed with ammonium persulfate as an oxidant. The thickness of the PPy layer was about 5 nm.

Electrodes were either from bucky paper or pellets of a mixture of MWNTs (85 wt%), acetylene black (5 wt%) and polyvinylidene fluoride (10 wt%). The aqueous electrolyte was 1 M H<sub>2</sub>SO<sub>4</sub>.

The results of capacitance measurements on the different nanotubes are given in Table 5-6. It can be concluded that the nanotubes with electrochemically deposited polypyrrole give much higher values of capacitance than the untreated samples. This proves that the properties of both materials are used in a nice way. In Figure 5-23 the difference in voltammograms of Hyperion with and without coating can be seen.

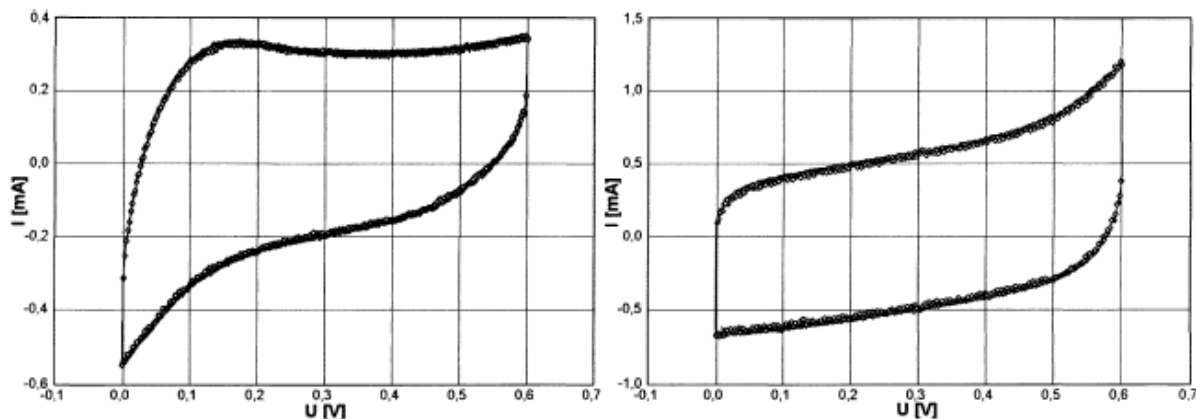


Figure 5-23: Potentiodynamics characteristics (2 mV/s) of a capacitor assembled in 1 M H<sub>2</sub>SO<sub>4</sub> from Hyperion nanotubes without PPy (left) and with PPy (right). Mass of each electrode was 3.5 mg.<sup>115</sup>

Striking is the effect with the coated nanotubes of the type P/800Al. In this case it might be expected that a thin PPy film also covers the inner core which is also accessible for the electrolyte.

A couple of the capacitors have been cycled over 2000 cycles and the charge loss never exceeded 20%. So, coating of the nanotubes with polypyrrole seems a nice way to enhance capacitance and efficiency for a long durability.

Kind of nanotubes	C (F/g) without PPy	C (F/g) with PPy
A/CoSi700	65	141
Hyperion <sup>TM</sup>	78	146
P/800Al	5	123
Pyrograf III	16	130
A/CoNaY600	50	163

Table 5-6: Capacitance values (F/g) of the nanotubular material in acidic medium (1 M H<sub>2</sub>SO<sub>4</sub>) with and without PPy.<sup>116</sup>

## 6. Determination of single nanotube properties

Synthesis and purification methods are still not successful enough to synthesise carbon nanotubes with all similar structures. However, engineering molecular electronics requires a very detailed understanding of physical properties of the molecules. To gain a better understanding, numerous theoretical and practical investigations on electronic, mechanical and molecular properties of carbon nanotubes have been performed until now.

At the moment, insufficient knowledge of handling single nanotubes and performing measurements on them complicates the practical investigation of their physical properties. Therefore, most literature on single nanotube properties focuses on modelling. Though, determination of mechanic properties and electron conductivity has shown to be practically feasible.

For investigation of only a single carbon nanotube, the different nanotubes have to be well separated in the sample. Otherwise, different nanotubes will influence each other's physical properties. It is not straightforward to isolate single walled nanotubes since these try to bundle.

This section starts with growing separated single walled nanotubes on a substrate and handling single carbon nanotubes by AFM (Atomic Force Microscope) techniques. Then, identification of a single walled nanotube structure by Raman spectroscopy and the investigation of conduction and mechanical properties follow. Eventually, theoretical studies on charging and discharging effects of single nanotubes will be treated.

### 6.1 Catalytic growth on a support

Catalytic growth of isolated single walled nanotubes with a diameter from 1 to ~3 nm on a silicium wafer has already been performed. First, a wafer that contains nanometre sized iron particles, that fulfil the role of catalyst, is prepared. Hereafter, CVD is applied and isolated SWNTs are formed on the substrate. Finally, the silicium support is partially oxidised in order to prevent charge transfer from the nanotube to support. Confirmation by AFM and TEM measurements proved that isolated SWNTs were present on the wafer.<sup>119</sup>

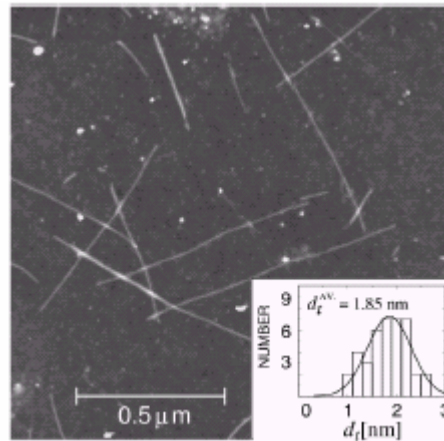


Figure 6-1: Single carbon nanotubes grown on support. The inset shows the diameter distributions that are taken from 40 different nanotubes.

## 6.2 Positioning by AFM techniques

In order to perform measurements on a single nanotube, it must be isolated on a measuring site, which is, most of the times, called a Micro-electromechanical System (MEMS). These systems have predefined sites for placing a nanotube.

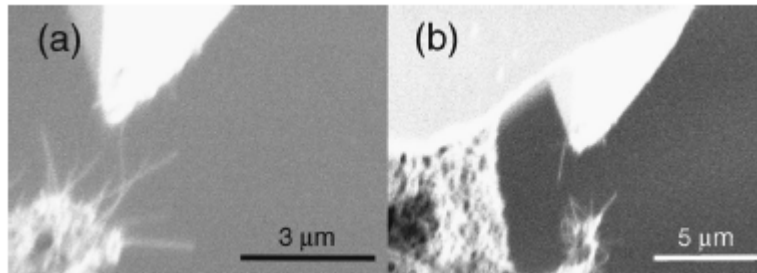


Figure 6-2 a) The AFM tip touches a single CNT in an attempt to pick it up. b) After the CNT sticks to the tip, the tip is moved away from the cartridge towards the MEMS.<sup>120</sup>

First, CNTs are picked up from a cartridge with an AFM tip (Figure 6-2) by attraction due to van der Waals forces. When a single CNT is picked up the AFM tip moves the CNT towards the MEMS. Near the MEMS, the real positioning starts. In four steps (Figure 6-3) the CNT is placed across the gap and is welded to the system by Electron Beam Deposition. This is a technique that uses a focused SEM electron beam to dissociate organic species in a specific area and deposit the residual ionised organic gas molecules on the junction of the CNT with the measuring system. It takes approximately 15 minutes to weld a single side of a CNT.

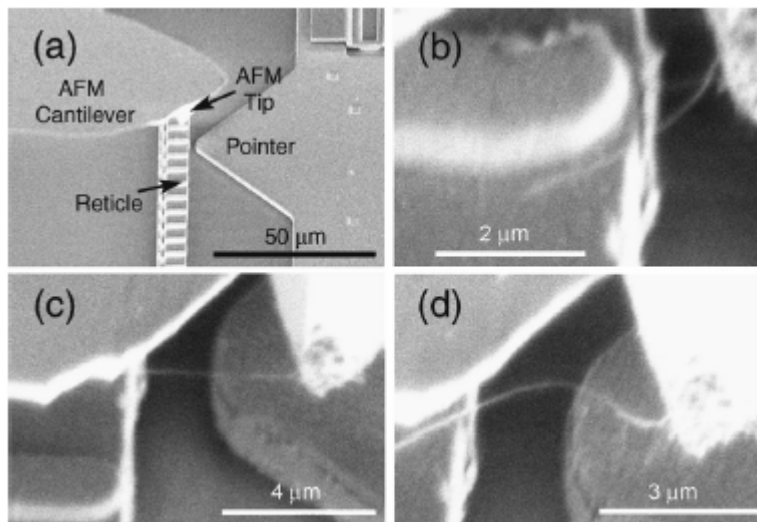


Figure 6-3: A) The MEMS. An AFM tip brings the CNT to its position. b) When the CNT makes contact with the site it is seen by the sudden change in shape of the CNT. Now it can be welded to the site. c) After welding the CNT is stretched. d) The CNT is placed across the gap and also welded to this site.<sup>120</sup>

After positioning and welding, electric and/or mechanic measurements can be carried out. Currents can be measured as well as stress strain relationships using the AFM tip to apply a strain to the CNT. For more information on mechanical properties see the review by Qian *et al.*<sup>121</sup>

### 6.3 Electronic property measurements of single SWNTs

Studying the electronic properties of SWNTs, scientists have been able to calculate models for energy bands and Density of States (DOS) in single walled carbon nanotubes. If these models have to be experimentally confirmed, a way has to be found in which atomic structures and electron densities can be visualised. Scanning Tunnelling Microscopy (STM) can do this job as it can display atomic structures as well as measure the DOS.

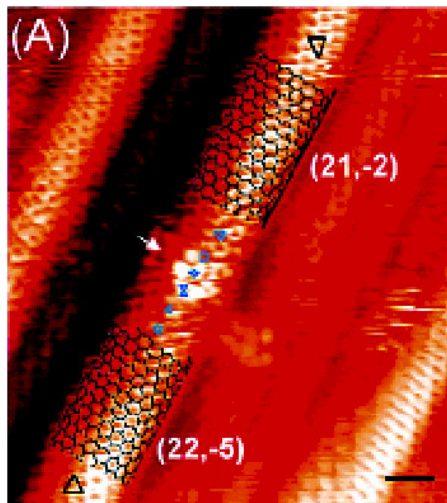


Figure 6-4: STM image of a SWNT. The chirality can be determined easily.

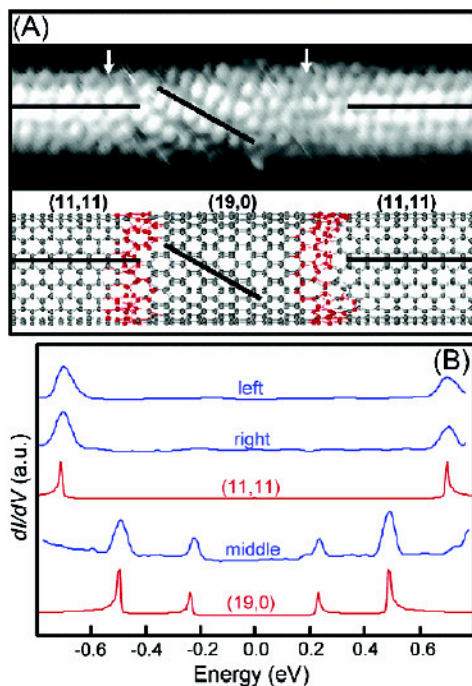


Figure 6-5: A) STM atomic resolved image of Intra Molecular Junction of SWNT. B) STM image measurement representing the Density of States corresponding to lines in A.<sup>122</sup>

As is shown in (Figure 6-4) and (Figure 6-5 A), chirality can clearly be determined from STM measurements. Combining this fact with the ability to measure electronic properties allows studying the effect of nanotube chirality on electronic properties. The spectroscopic image (Figure 6-5 B) shows the density of states as measured by a STM. As these two images show, this technique can also

be used to determine properties of intra-molecular SWNT junctions. In addition, it can also be used for measuring influence of symmetry, defects, doping, electronic contacts and so on.

## 6.4 Measuring charge transfer to single CNTs in electrolytes

Until now, measuring charge transfer from single nanotubes in electrolyte have seemed to be impossible. However, carbon nanotubes have already been applied as anode materials in lithium-ion battery systems at the moment. More information on this topic can be found in the sections on (electro)chemical energy storage in carbon nanotubes.

## 6.5 Identification of single nanotubes by Raman spectroscopy

Determination of the structure of a single carbon nanotube by Raman spectroscopy is possible as the density of electronic states is very large for some energy ranges in single walled carbon nanotubes. The density of states is an indication for the number of energy states,  $\Delta N$ , per energy difference,  $\Delta E$ . Every different nanotube geometry, i.e. a different  $(n,m)$  pair, results in a unique pattern for the density distribution of states which can also be calculated theoretically. If the photon energy is (almost) equal to the energy needed for the valence to conduction band transition, an intense Raman signal is found as a direct result of the strong coupling between the electrons and phonons of a nanotube under resonance conditions.<sup>123</sup>

In the identification of the different tube geometries the radial breathing mode (RBM), which is a certain type of vibration, plays an important role. A inversely linear dependence of the RBM feature intensity on tube diameter exists if one dimensional physical behaviour is assumed.<sup>119</sup> After a theoretical calculation for a certain geometry is performed, the RBM measured can be linked to an individual nanotube geometry. However, small differences in intensity and RBM frequency are caused by difference in nanotube length and incompleteness of the theoretical models used. Additional differences arise for signals with almost the same RBM mode frequency if nanotube chirality is different.

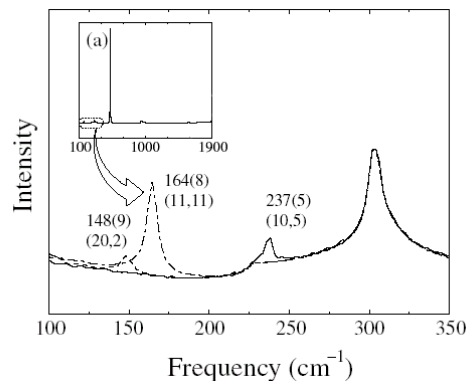


Figure 6-6: Raman spectra for three different spots, showing different RBMs. Each spot is clearly associated with only one RBM and thus a single nanotube. The Raman signal of the Si substrate is visible at  $303 \text{ cm}^{-1}$ .<sup>119</sup>(Picture is edited)

This second way to identify the geometry of a single single-walled carbon nanotube enhances further fundamental research into the dependence of physical properties on nanotube geometry. This is a prerequisite for detailed engineering of molecular electronics based on nanotubes as nanotube structure could be directly linked to physical properties for single nanotubes.

# 7. Molecular electronics

## 7.1 Field Emitting Devices

Directly from the beginning CNTs have been and studied for their good field emitting properties. They are such good field emitters because of their length to diameter ratio and low voltage emission.

Nowadays scientists are trying to find good and cheap techniques for the production of CNT field emitting guns and even entire displays.

Most of the information in this section comes from a review by *Bonard et al.*<sup>124</sup>

### 7.1.1 Fabrication of CNT electron field emitters

Before we go into field emitting properties we have to discuss the different production techniques. Two different kinds of electron sources can be made from CNTs, single and multiple electron beam devices. For example single beam as a electron bundle in an electron microscope and multiple beam in a flat panel display.

#### Single nanotube emitters

- Single MWNT emission source:  
Individual MWNTs can be mounted on an etched wire under an optical microscope with two, independently moving, 3-axis micromanipulators. The individual nanotubes stick to the tip only by van der Waals forces or by applying a bit of conductive adhesive to the tip. Because of the too low resolution of an optical microscope SEM is necessary to observe the single MWNT.
- SWNT emission from raw material:  
It is more difficult to obtain a single SWNT from ropes or unpurified material, so a macroscopic fragment of raw material is picked up with a pair of tweezers and attached to a tungsten tip so you actually have many emitters but for measurements one can use a probe hole in the counter electrode to study the behaviour of only a single SWNT as field emitter. Use of SEM is necessary mandatory.
- SWNT emission from rope of SWNTs:  
A rope is picked out of a mat of SWNT material and detached from it by making electrical contact and applying a voltage difference (~10V) over the SWNT and the mat. Use of SEM is mandatory.
- SWNT emission from purified material:  
Commercially available material with well separated tubes in a solution allows mounting of tubes with very little contaminating material. The disadvantage are the unknown effects of the purification process on the morphology of the CNTs.
- A SWNT attached to an AFM tip:  
By using the electron bundle of a SEM for electron beam irradiation one can weld the SWNT to the AFM tip. The welds are mechanically strong and have a good electronic contact.
- Single SWNT growth on AFM tip:  
Direct growth of a SWNT by CVD on an AFM tip can be done and looks promising.

#### Continuous film emitters

Planar films of emitting nanotubes can be made rather easily:

- Film from MWNTs in a colloidal suspension:  
*De Heer et al.* produced a film by drawing a colloidal suspension of MWNTs through a nanopore alumina filter. Next, the film was transferred by pressing the filter face down on a Teflon or Teflon-coated metal surface. This technique is not restricted to MWNTs but can be used for all types of nanotubes. The same result can be obtained by spraying the suspension on a heated substrate.
- Purified MWNTs dispersed in a matrix:

Collins and Zettl dispersed nanotubes in an epoxy matrix and prepared emitters of  $(50 \times 50) \mu\text{m}^2$  under pressure and with a polishing to obtain a reproducible and macroscopically flat surface.

- Crushed and mixed MWNTs:

Crushed MWNTs are mixed with products to form a paste which can be applied to a metallic cathode and cured.

#### **Patterned films using post deposition techniques**

For many applications it is necessary for the emitting film to have a certain pattern. Different post deposition techniques to obtain patterned films are presented here:

- A nanotube/epoxy paste is pressed into channels etched in a glass substrate. Cathode surface is polished to expose the micro channels.
- Nanotubes mixed in an organic mixture of nitrocellulose, the resulting paste is squeezed onto a metal-patterned sodalime glass through a metal mesh. Subsequently the emitter was heated to remove the organic binder.
- A resist layer is patterned by e-beam lithography on a substrate. After this a nanotube dispersion is applied to the substrate. Nanotubes precipitate in the resist openings and after lift-off a patterned film is obtained.
- It is also possible to position individual nanotubes at specific locations and with specific orientations by applying a nanotube suspension on self-assembled monolayer templates defined by lithography

#### **Patterned films using direct growth on catalyst support**

Predefined catalyst patterns can be used to grow CNTs on specific locations. The patterns are made from i.e. cobalt films that are deposited from laser ablation. The obtained film is etched with single laser pulses using a cylindrical lens, while being exposed to air. The MWNTs only grow on the Co particles along the edges of the eroded tracks.

A second technique is based on standard photolithography or e-beam lithography. Basically a resist is coated on the substrate, exposed and developed. The resist can be used in two ways:

- Resist as mask over the catalyst and CNT growth over resist after which the resist is removed and a pattern is left over
- Resist as protection, unprotected catalyst is evaporated and after removal of resist the CNTs are grown

The techniques to grow the CNTs after making a catalyst pattern also differ and are much alike described in the continuous film production.

One method that is different from the others is the use of a stamp with ink, called microcontact printing. Liquid phase catalyst precursor is dropped on a patterned elastomer stamp. The stamp is then pressed against a substrate and afterwards MWNTs can grown by CVD on the pattern of catalyst. Important is the ability to vary the catalyst precursor concentration, hydrocarbon gas and the temperature. All these parameters can be optimised for the desired MWNT density.

For more information on different techniques see the review of *Bonard et al.*<sup>124</sup>

### **7.1.2 Field emission from CNT films**

Field emission is the emission of electrons from a solid by tunnelling through the surface potential barrier. The emission current depends on the electric field,  $E$ , and the workfunction,  $\phi$ . The Fowler-Nordheim model shows that the dependence of the emitted current on the local electric field and the workfunction is exponential. As a consequence small variations in the shape or surrounding of the emitter have strong impact on the emitted current.

This sensitivity brings along many problems in comparing measurements because of the different shapes of set-ups. There is also a difference between integrated (macroscopic), millimetre, measurements and microscopic, micrometer, measurements.

Most reports on field emission describe the fabrication method and a typical resulting I-V curve. Results from this kind of reports are given in Table 7-1.

Reference	Emitter	$d$ ( $\mu\text{m}$ )	$S$ ( $\text{cm}^{-2}$ )	$E_{\text{to}}$ ( $\text{V}/\mu\text{m}$ )	$E_{\text{thr}}$ ( $\text{V}/\mu\text{m}$ )	$J_{\text{max}}$ ( $\text{A cm}^{-2}$ )	Remarks
[22]	MWNT	10–40	0.002	n.a.	<25*	1	Very dense “tubulene” film
[153]	MWNT	15	0.003	n.a.	~15*	10	Very dense “tubulene” film
[24]	Arc MWNT	20	0.008	n.a.	20*	0.1	
[154]	Arc MWNT	30	0.007	4.0	6.5		
[113]	Arc MWNT	125	0.07	2.6	4.6		
[79]	Arc MWNT	125	0.07	1.1	2.2		Purified sample with closed caps
[124]	Arc MWNT	20–100	$2.5 \times 10^{-5}$	7.5*	10*	0.4	Open tubes dispersed in epoxy
[155]	Arc MWNT	80	0.025	0.9*	4*		O <sub>2</sub> plasma treated tubes dispersed in epoxy
[126]	Arc MWNT	200	0.02	n.a.	1.5		Tubes dispersed in epoxy
[120]	SWNT	125	0.07	1.5	3.9		
[156]	SWNT	10–300	0.002	n.a.	4–7	4	
[157]	SWNT	150	3.1	2.1*	n.a.		
[91]	CVD MWNT	n.a.	0.001	1.7*	n.a.		
[93]	CVD MWNT	70	n.a.	n.a.	4.8–6.1		Aligned MWNTs, 15 emitters
[158]	CVD MWNT	150	3.1	n.a.	2.1*		Large amount of graphitic fragments
[134]	CVD MWNT	n.a.	0.0003	4.8	6.5	0.1–1	
[159]	CVD MWNT	600	0.07	n.a.	$\geq 5$		
[160]	CVD MWNT	150	0.2	3	6.6*		Si substrate
[99]	CVD MWNT	500	0.1	1.6	5*		Steel substrate
[99]	CVD MWNT	500	0.1	3	5.6*		Ni substrate
[161]	CVD MWNT	10–300	0.002	0.75	1.6	1–3	Catalyst supplied in gas phase
[162]	Graphitic fibers	300	1–10	2.1	n.a.	0.2	

$d$  is the interelectrode distance,  $S$  the emission area,  $E_{\text{to}}$  and  $E_{\text{thr}}$  are the turn-on and threshold fields needed to produce an integrated current density of  $10 \mu\text{A}/\text{cm}^2$  and  $10 \text{mA}/\text{cm}^2$ , and  $J_{\text{max}}$  is the maximal current obtained without destruction of the emitter. n.a. means that the value is not indicated or could not be deduced from the figures, and \* indicates that the value was estimated or extrapolated from the presented data.

Table 7-1: The emission characteristics of CNT films.<sup>124</sup>

All types of nanotubes have excellent field emission properties with threshold fields, that produce  $10 \mu\text{A}/\text{cm}^2$ , of only  $1 \text{V}/\mu\text{m}$  and turn on fields, that produce  $10 \text{mA}/\text{cm}^2$ , around  $5 \text{V}/\mu\text{m}$ . Nanotube films are also able to emit a current density up to a few  $\text{A}/\text{cm}^2$  at fields below  $10 \text{V}/\mu\text{m}$ .

Because of the large differences in results for slightly differing parameters *Bonard et al.* also provided a comparison of films under the same experimental conditions.

Influence	Emitter	$d$ ( $\mu\text{m}$ )	$S$ ( $\text{cm}^{-2}$ )	$E_{10}$ ( $\text{V}/\mu\text{m}$ )	$E_{\text{thr}}$ ( $\text{V}/\mu\text{m}$ )	Remarks
Density and geometry	MWNT	25	n.a.	$<2.7^*$	$\sim 4.8^*$	Random alignment
	MWNT	25	n.a.	$\sim 40^*$	n.a.	Short vertical tubes
Geometry	Arc MWNT	125	0.07	2.6	4.6	Average over 15 emitters
	SWNT	125	0.07	2.8	5.2	Average over 12 emitters
	Open MWNT	125	0.07	4.5	30	Average over six emitters
	Graphitic fibers	125	0.07	5.6	14	Average over five emitters
Surface treatment	MWNT ta-c coated	125–400	0.01	1.6	n.a.	
	MWNT (as produced)	125–400	0.01	2.4	n.a.	
Density and geometry	SWNT	10–500	$10^{-5}$	n.a.	2.4	Randomly aligned
	CVD MWNT	10–500	$10^{-5}$	n.a.	3.5	Dense aligned arrays
Density	CVD MWNT	125	0.007	9.8	14.4	Low density, patterned films (Fig. 5(a))
	CVD MWNT	125	0.007	2.2	3.3	Medium density, patterned films (Fig. 5(b))
	CVD MWNT	125	0.007	3.6	5.3	High density, patterned films (Fig. 5(c))

Table 7-2: The emission characteristics of CNT films under the same experimental conditions.<sup>124</sup>

Differences occur due to structural differences and differences in treatment, diameter size, open/closed cap, surface treatment etc.

Density and orientation of the tubes on the film also influences the emission.

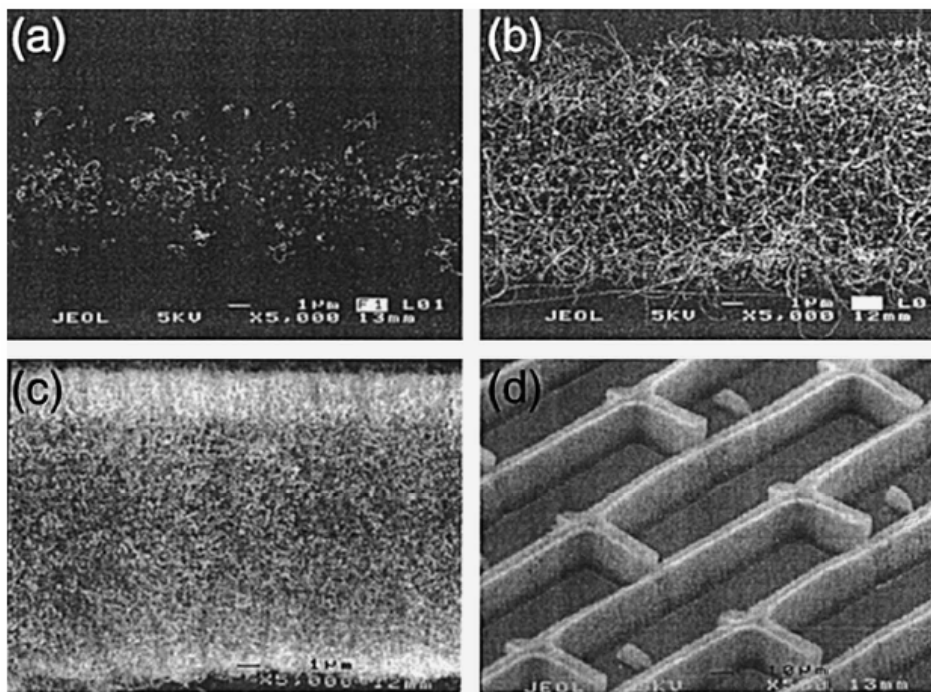


Figure 7-1: SEM micrographs of patterned films of MWNTs prepared by  $\mu$ CP of a catalyst followed by CVD growth. The concentration of catalyst in the ink solution was (a) 1mM, (b) 5mM, (c) 40mM, (d) 50mM.<sup>124</sup>

When comparing samples with different densities as in Figure 7-1 the influence can be seen in the I-V curves see Figure 7-2.

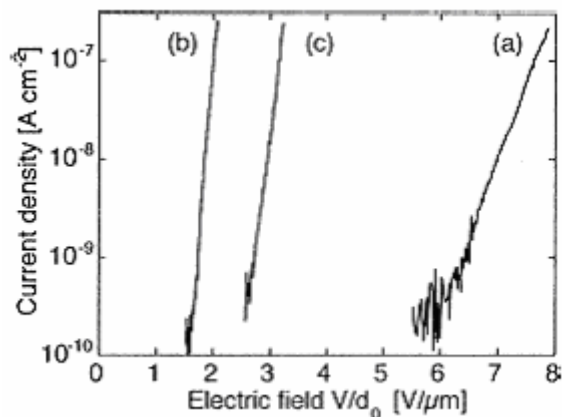


Figure 7-2: I-V curves for different MWNT densities as seen in Figure 7-1. The best result is (b).<sup>124</sup>

Analysis of eleven samples shows that films of medium densities with nanotubes protruding over the film surface show emission at the lowest fields. Which also can be seen in the scanning field emission images, see Figure 7-3.

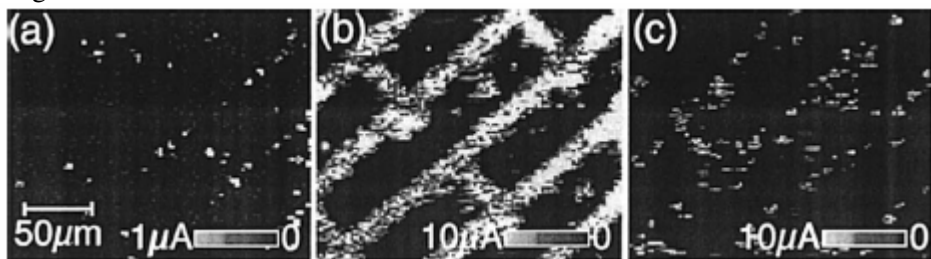


Figure 7-3: Scanning field emission images of MWNT films of different densities acquired at constant voltage and tip height. The greyscale represents current intensity. Images were taken from samples similar to those from Figure 7-1.<sup>124</sup>

Here it is also clear that the medium density film has the highest current density.

### 7.1.3 Degradation of CNT films

Several different processes can lead to degradation of the CNT film, resistive heating, bombardment from gas molecules, arcing electrostatic deflection and mechanical stresses etc. Also chemical degradation phenomena such as adsorption and desorption of molecules on the emitter surface can occur.

Stable emissions over more than 20 h have been observed and even an emission of 8000 h of  $10\text{mA}/\text{cm}^2$  with an 11% field increase has been possible. The origin of degradation is not clear but it seems that residual gasses have a significant influence as well as the emitted current density. In addition the intrinsic properties of the CNTs have an importance. Tests have shown that degradation of SWNTs was much faster than of MWNTs.

### 7.1.4 Field emission from single CNTs

Experiments on single nanotube emitters give a reliable way to investigate the emission mechanism and workfunction. First measurements were reported by *Rinzler et al.* who studied an arc produced MWNT mounted on a carbon fibre. It was shown that the emission followed roughly a Fowler-Nordheim behaviour. The currents emitted were about 100nA at 0.12 V/ $\mu\text{m}$  field strength.

Other studies show Fowler-Nordheim behaviour up to 5-20 nA for closed and open tubes. As the current increased, saturation effects were observed. It was noted that all emitters were able to emit over an incredible current range up to 0.1 mA or for some even 0.2 mA per tube. It was also noticed that open tubes needed twice the voltage to start emitting. But there are contradictory results from *Saito et al.*<sup>125</sup> They found that open MWNTs started emitting electrons at the lowest fields, followed by MWNTs produced in a hydrogen atmosphere and finally the closed arc discharge MWNTs started emitting electrons at the higher fields. The differences observed are probably due to different measurement set-ups, growing methods, purity and emitter geometry.

#### a) Emitter stability and failure

As seen in section 6.3 FEM measurements on single SWNTs showed two regions in the I-V curve. Step like fluctuations at low emitted currents with a switching frequency that increased with the current and became maximal at the onset of saturation, followed at higher currents by stable emission with flicker noise. Explanations for this behaviour are given in section 6.3.

Failure of single nanotubes is in almost all cases abrupt. For a single closed MWNT stable emission was observed at 2  $\mu\text{A}$  for more than 90 h at  $10^7$  mbar. Failure occurred on most emitters in a catastrophic irreversible way in less than 10 ms.

However *Fransen et al.* measured one MWNT during more than two months at 0.4  $\mu\text{A}$  at  $10^{-9}$  mbar without any observable degradation. The mechanism that leads to catastrophic failure is not yet completely understood but it appears that the failure occurs at a very short time scale (<1ms) at currents above 0.1 mA and that it involves an irreversible damage to the tube, in all cases the failure occurs on the defects of the nanotube. It still is unclear whether the degradation in CNT films is abrupt or gradual.

## 7.2 Transistors

Smaller silicon based integrated circuits result in both a higher speed and device density.<sup>126</sup> As a result, downscaling of these devices has been very important since their first implementation. However, at the moment it is generally accepted that silicon devices will reach fundamental scaling limits within a decade or so. This limit is caused by the minimum wavelength of light used in lithographic techniques used for integrated circuit production nowadays. For this reason a quest for alternative, integrated circuits with smaller dimensions has started. A major step in downscaling would be the application of

single molecules in electronic devices.<sup>127</sup> Carbon nanotubes have already shown promising results in single molecular transistors.

For successful implementation of molecular transistors in a large and complex logic systems, they must show signal amplification. Signal amplification makes it possible to reference separate signals along a chain of logical operations. In addition, noise caused by thermal fluctuations and environmental disturbances is also reduced.<sup>127</sup> Three terminal nanotransistors, in special, field-effect-transistors show amplifying behaviour and have recently been investigated for this reason.

CNT based transistors can be divided into two main categories: CNT field-effect-transistor (CNTFET) and CNT single-electron-transistor (CNTSET). CNTFET behaviour and performance is also compared with conventional the Metal-Oxide-Semiconductor (MOS) Field Effect Transistor (FET). In this section, an overview is given of their production techniques, basic principles and advantages.

### 7.2.1 Principles of the MOSFET and CNTFET

A basic MOSFET involves two main electrodes, designated as “source” and “drain”, connected by a semi-conducting channel. In conventional devices this channel is made of silicon. In CNTFETs the channel is formed by a single, semi-conducting CNT. A third electrode, the “gate” is separated from the channel by a thin insulator film and can also be placed on top of the nanotube.

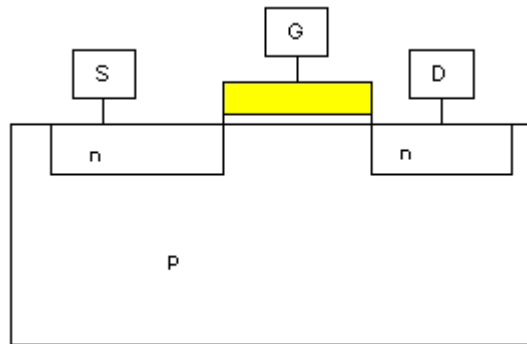


Figure 7-4: Set-up of a MOSFET

If no charge is present on the gate, the channel is not conducting. The channel of a p-type (hole-conducting) MOSFET becomes conductive when a negative charge is placed on the gate and a certain threshold voltage is exceeded. This is the very basic principle of this type of transistor. Almost the same accounts for n-type MOSFETs in which a positive charge must be put on the gate. A CNTFET works in a slightly different way as will be explained further on.

### 7.2.2 Manufacturing of a CNTFET

In 1998 Semi-conducting SWNTs<sup>128</sup> and MWNTs<sup>129</sup> were used in CNTFETs for the first time. Due to the basic principles of a CNTFET a metallic CNT cannot be used since it is always conducting. An example of the manufacturing of one of the first CNTFETs is given below.

As grown CNTs are purified by sonication in a  $\text{H}_2\text{SO}_4/\text{H}_2\text{O}_2$  to remove catalyst particles. The purified nanotubes are dispersed in dichloroethane and spread over a silicon substrate, which is covered with siliconoxide, an insulating compound. On top of this layer, predefined electrode areas are created by conventional lithographic techniques. The nanotubes are randomly spread over the surface this way and in some cases a nanotube connects two electrodes.<sup>129</sup> A slightly different approach is to spincoat the CNTs on a substrate first, after which the electrodes are deposited with electron beam lithography. The latter methodology can also be used to create top gated CNTFETs, which is schematically shown in Figure 7-5.<sup>130</sup>

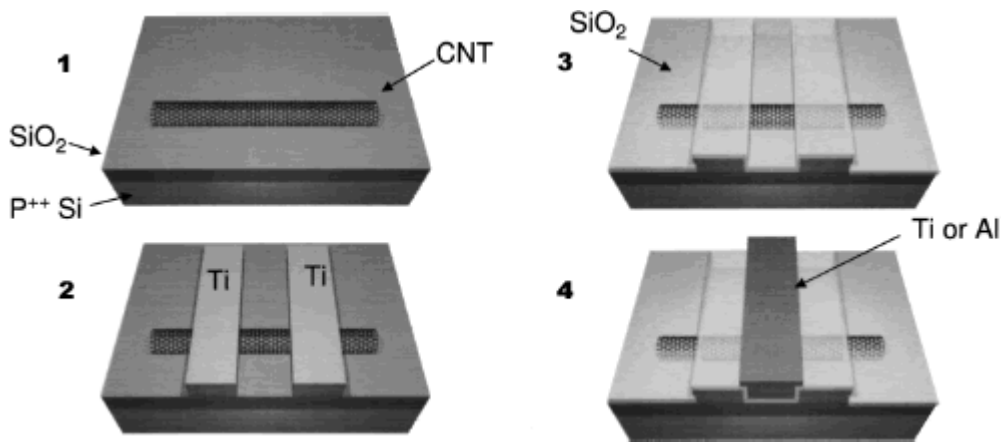


Figure 7-5: Fabrication of a top gate CNTFET

It is also possible to position a nanotube at a certain position with AFM-like techniques. Semi-conducting and metallic nanotubes in a single rope can be separated by ‘constructive destruction’. A current is put through the nanotube rope and the metallic tubes break down selectively, leaving the semi-conducting nanotubes over. The high stability of metallic nanotubes is maintained as long as moving electrons have insufficient energy to excite optical phonons.<sup>8</sup> Furthermore, the environment also plays an important role as adsorbed gasses influence the nanotubes behaviour. So adsorption of gasses should be prevented as much as possible.

## 7.2.3 CNTFET physics

### a) Conductivity in CNTs

To develop a better understanding of the switching process, a detailed model of charge transport in the channel must be set up. Electron transport in metallic CNTs is ballistic of nature, which means that electrons move with a much higher speed than expected on the ground of thermal equilibrium. Ballistic transport can only occur in strictly confined semi-conductor regions and is totally determined by material properties. Electron transport in semi-conducting CNTs is far more complicated due to interband scattering, influences of charges at the electrode interface and adsorbed gasses. Therefore, conductivity in semi-conducting CNTs is usually described in classic physical laws of diffusivity.<sup>8</sup> Diffusive charge transport means that electron motion can be described with an effective mobility  $\mu$ . In case of ballistic transport, the average free path  $l$  of an electron is relatively short ( $\sim 2$  nm.) compared with the ballistic transport situation ( $l \sim 10$   $\mu$ m).<sup>131</sup>

### b) Doping of CNTs

Classical semi-conductor physics is mainly based on two types of charge transport: either by negative or positive charge carriers. In the first case the material is n-type semi-conducting while in the latter case is spoken of a p-type semi-conductor. Some times it is even possible to have nanotube conductivity in a transistor either by n-type or p-type charge carriers, dependent on the gate-source voltage applied.<sup>127</sup> This behaviour is called *ambi-polar*.

As grown, single walled CNTs show p-type semi-conducting behaviour which is explained by several theories. The most commonly accepted theory states that the p-type conducting behaviour is caused by charge transfer from the nanotube to the electrode material with a relatively low Fermi level. Another explanation for the p-type behaviour is doping of the nanotubes by foreign atoms during synthesis or purification or the absorption of gasses.<sup>128,130</sup> However, adsorption of oxygen is not true doping for several reasons.

The large charge carrier density, which is approximately one hole per 250 Carbon atoms, in semi-conducting nanotubes is remarkable.<sup>129</sup> CNTs can be (partially) doped to an n-type semi-conductor in several ways. p-Type nanotubes can be exposed to electron donating compounds such as alkali metals

to form n-type semi-conductors.<sup>132</sup> An easier way to perform the p-n transformation is by partially heating the nanotube, which transformation has shown to be reversible of nature<sup>133</sup>. However, doping of NTs by potassium and adsorption of oxygen resulted in different behaviour which indicated a different doping mechanism.<sup>134,133</sup>

#### **7.2.4 Switching mechanism of a MOSFET and CNTFET**

A MOSFET is indeed a field effect transistor. Directly after the discovery of the CNTFET, mechanisms for the functioning of this type of devices were developed. A link to the MOSFET mechanism was made rapidly which meant that influence on the channel was considered of key importance for this type of devices.

Later investigations into CNTFETS have shown the partial incorrectness of this mechanism. It became clear that the transistor functioning is mainly based on the Schottky barriers (SB) present at the metal / semi-conducting CNT junctions<sup>127,133</sup>. This type of transistor is very uncommon in conventional semiconductor physics. Switching occurs rather by modulation of the contact resistance than by altering the channel resistivity. SB transistors can have very small dimensions which possibly allows downscaling of silicon devices.<sup>135</sup> For very small Schottky barriers the device functions as a conventional channel limited field-effect-transistor. Adsorption of gasses results in other properties of the CNT transistors by changing the electrode properties.

The Schottky barrier present at the metal /semiconductor interface prevents charges from being transported through this interface. At low voltages there is substantial charge density in the channel, but these are blocked by the Schottky barriers. Applying a larger gate-source voltage results in a stronger electric field at the electrodes and as a result the Schottky barrier becomes smaller. Now, the charge carriers can tunnel in a thermally assisted way and the transistor becomes conductive.<sup>134</sup>

For a more detailed theoretical examination of CNT based SB transistors is referred to *Guo et. al.*<sup>136</sup> Articles of *Ph. Avouris et. al.* also explain the functioning of the SB-CNTFET in more detail.

#### **7.2.5 Characteristics of a CNTFET**

Even at their first investigations, CNT based transistors had excellent properties that were comparable with silicon based MOSFET transistors. The high stability and conductivity of single carbon nanotubes result in excellent transistor behaviour. High current densities for the 'on'state (2100  $\mu\text{A}/\mu\text{m}$ ) were achieved together with excellent on/off ratios of approximately  $10^5$ . In a similar MOSFET the maximum current density is only 650  $\mu\text{A}/\mu\text{m}$  under the same bias conditions.

Channel length of CNTFETs can be reduced to 5 nm, before tunnelling at room temperature results in unacceptable leakage currents. This means that very high device densities could be achieved.

Top gate devices even show better performance than transistors in which the substrate is the gate electrode. Switching in top gated CNTFET happens at much lower gate voltages. Another advantage of top gate transistors is the ability to switch different transistor individually. On / off ratios as high as  $10^6$  can be achieved with top gate CNTFETs.

#### **7.2.6 Optimisation of CNTFETs**

CNTFET devices can be improved in several ways, some of which will be described here. The contact resistivity can be reduced by annealing the sample at a high temperature in an inert atmosphere. This will improve the device characteristics enormously. The geometry of the electrodes is also very important, a needle-like electrode results in a stronger electric field at the electrode/nanotube interface and thus in smaller Schottky barriers which improves the performance of the transistor.

Only a single CNT FET does not make a completely functional electronic circuit. Several transistors can be combined with each other to form different logic operators. With these operators, fully functional devices can be created with much faster transistors. But in our opinion, new technologies for accurate placement of nanotubes should be developed just as methods for smaller electrode contacts. Else the size limit of molecular transistors is still determined by the contact dimensions.

### 7.3 Single electron transistor

Due to the ability to define nano-scale regions of p or n material on a SWNT scientist have been able to make such a small quantum dot (QD). The properties of such a small doped region are influenced by the quantum mechanical effects of a single electron. The Coulomb force of a single electron can prevent the entrance of a second electron and tunnelling effects also play a role in the process. The energy for one electron to move into the system is:

$$E_c = \frac{e^2}{2C} \quad (1.14)$$

$E_c$  is called the Coulomb blockade energy, which is the repelling energy of the previous electron to the next electron. So charging and discharging becomes a discontinuous process, electrons have to move through the system one by one. If two QDs are joined at a point and form a channel, it is possible for an electron to pass from one dot to the other over the energy barrier, this phenomenon is called tunnelling. In order to overcome the Coulomb blockade energy  $E_c$ , the applied voltage over the QDs should be

$$V > \frac{e}{C} \quad (1.15)$$

In order to observe Coulomb blockade and tunnelling, the energy of the electron must be higher than the thermal scattering energy,

$$\frac{e^2}{2C} > k_B T \quad (1.16)$$

If these QDs are connected to other conductive materials (metal wires, polymers, CNTs) a SET is formed.

#### 7.3.1

#### Construction of SET on SWNT

##### a) Chemical profiling

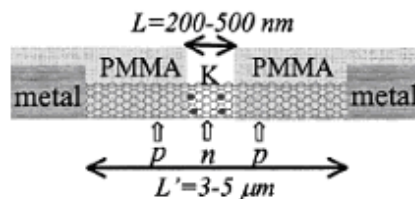


Figure 7-6: Schematic p-n-p nanotube device

As with normal CNT transistors the CNTs are doped in an uncovered region with K to make it n-type, the neighbouring regions are covered with PMMA to keep them p-doped. This p-n-p nanotube system behaves as a single QD, investigations showed that the QD are confined in the n region with the two p-n junctions as barriers for the dots. Chemical profiling a single SWNT can lead to on-tube QDs much smaller than the lengths of the nanotubes between metal electrodes ( $3-5 \mu\text{m}$ ). In order to function properly the system has to be cooled to  $<100\text{K}$ . This technique is explained more in detail by Kong *et al.*<sup>137</sup>

### b) Bending CNTs

Another technique found earlier by *Cees Dekker et al.*<sup>138</sup> showed the fabrication of a room temperature SET (RTSET). They were able to produce a region between two tunnelling barriers formed by bending a metallic SWNT with an AFM. The nanotube is placed between Au electrodes on a Si/SiO<sub>2</sub> substrate. In Figure 7-7 A and B are the bending steps with an AFM and C and D show the results.

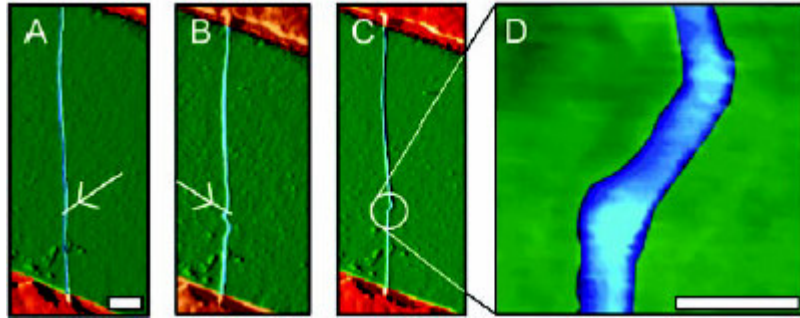


Figure 7-7: Fabrication of a room-temperature SET using AFM. Step A and B: bending with AFM. C and D is the resulting RTSET.<sup>138</sup>

### 7.3.2 Working mechanism of a SET

A set consists out of a conducting island that is connected by tunnelling barriers to two metallic leads. For temperatures and bias voltages that are low relative to a characteristic energy required to add an electron to the island, electrical transport through the device is blocked. Conduction is possible however by tuning a voltage on a close-by gate, this makes the device into a three terminal transistor.

For specific characteristics and I-V curves see the works referred to in this section.<sup>137,138</sup>  
Further research is absolutely necessary.

## Conclusion

Lack of commercially feasible synthesis and purification methods is the main reason that carbon nanotubes are still not widely used nowadays. At the moment, nanotubes are too expensive and cannot be produced selectively. Some of the already known and upcoming techniques look promising for economically feasible production of purified carbon nanotubes. Insight into the carbon nanotube world is increasing rapidly as can be seen from the large quantity of recent literature and patents found. Most of the properties needed for an increase of insight can be measured either on single tubes or on bigger samples. Only discharge measurements on a single tube have not yet been reported.

At this moment, laser ablation produces the cleanest material, but the costs are still rather high. Arc discharge can produce grams of low purity nanotubes. The CVD technique is still under development but preliminary results look promising, as do prospects of large scale CVD.

The main purification techniques are: oxidation, acidic treatment, annealing, sonication, filtration and functionalisation techniques. These techniques have shown to be economically feasible and are ready to be applied at larger scale. However, other more exotic techniques also look promising. These can be focused in detail on the application, and thus will give the exactly needed carbon nanotubes.

Possibilities for nanotube-based applications are numerous and will be a step forward in technology. Most of these applications have shown to function in laboratories, but even less applications are sufficiently developed for production. From the applications this report focusses on, carbon nanotube displays and other field emitting devices are expected to be available in the near future. Molecular integrated circuits are still a rather big step away, although single molecular transistors can be made with the use of nanotubes. More accurate placement techniques and smaller electrodes are needed for better device functioning, because large transistor densities are necessary if carbon nanotube transistors want to compete with conventional transistors. Energy storage in carbon nanotubes is even a bit further away from application because storage capacities are not yet satisfactory. Electrochemical lithium intercalation looks the most promising of the energy storage techniques described. Fortunately, insight in modelling aspects and characteristics of these processes are increasing rapidly. Though, modelling can still not explain all the experimental data.

Some future applications of carbon nanotubes look very promising. All we need are better production techniques for large amounts of purified nanotubes that have to be found in the near future. In our opinion, nanotubes promises to open up a way to new applications that might be cheaper, lower in weight and have a better efficiency.

## Appendix A: List of abbreviations

AAS	Atomic adsorption spectroscopy
ACCVD	Alcohol catalytic chemical vapour deposition
ACD	Anode to cathode distance
ATM	Atomic force microscope
CNH	Carbon nanohorn
CNS	Carbon nanostructures
CNT	Carbon nanotube
CNTFET	Carbon nanotube field-effect-transistor
CNTSET	Carbon nanotube single-electron-transistor
CVD	Chemical vapour deposition
CVFF	Consistent valence force field
DFT	Density functional theory
DOS	Density of states
DSC	Differential scanning calorimetry
DTA	Differential thermal analysis
DTG	Differential thermogravimetry
ECP	Electrically conducting polymers
EDLC	Electrical double layer capacitor
ESFF	Extensible systematic force field
ESR	Electron spin resonance
FED	Field emitting device
FEL method	Free electron laser method
FET	Field-effect-transistor
GCEMC	Grand canonical ensemble Monte Carlo
GNF	Graphite nanofibre
GPC	Gel permeation chromatography
HF	Hartree-Fock
HiPco process	High pressure CO disproportionation process
HPLC	High performance liquid chromatography
HPLC-SEC	High performance liquid chromatography - size exclusion chromatography
HRTEM	High resolution tunnelling electron microscope
IR	Infrared
LCVD	Laser-assisted thermal chemical vapour deposition
MEMS	Micro-electromechanical system
MM	Molecular mechanics
MO	Molecular orbital
MOS	Metal-oxide-semiconductor
MOSFET	Metal-oxide-semiconductor field effect transistor
MWNT	Multi walled nanotube
NIR	Near infrared
NREL	National renewable energy laboratory
NT	Nanotube
PPV	Poly-p-phenylenevinylene
PPy	Polypyrrole
PTFE	Poly-(tetrafluoroethylene)
QM/MM	Quantum mechanics

RBM	Radial breathing mode
SB	Schottky barriers
SC	Supercapacitor
SEC	Size exclusion chromatography
SEM	Scanning electron microscope
STM	Scanning tunnelling microscopy
SWNT	Single walled nanotubes
TEM	Tunnelling electron microscope
TDS	Thermal desorption spectroscopy
TG	Thermogravimetry
TGA	Thermo graphic analysis
UFF	Universal force field
UV	Ultra-violet
VGCF	Vapour grown carbon fibre

# Appendix B: Overview of purification techniques

## B.1 Method for purifying single wall carbon nanotubes<sup>54</sup>

Patent on a method for purifying SWNTs. SWNTs, produced with arc discharge, Ni:Y:Ti:graphite = 2:2:2:94, are purified with two oxidation steps.

First oxidation step:

1. Thermal oxidation: heating from 350 – 600 °C.  
Metal catalyst acts as oxidation catalyst for the graphite carbon layers.
2. Wet oxidation: reflux in hydrogen peroxide solution between 60-120 °C.  
Metal catalyst surface is cleared, so the metal can be solvated in acid, the SWNTs remain suspended.
3. Wet oxidation: reflux in nitric acid.  
The metal catalyst is exposed to acid and solvated; the SWNTs remain suspended.

Second oxidation step:

4. Wet oxidation: reflux in hydrogen peroxide solution  
Metal catalyst acts as oxidation catalyst; both SWNT and carbon oxidise. Because there is only a small amount of catalyst left, this step does not affect the yield very much.
5. Wet oxidation: reflux in hydrochloric acid.  
The metal catalyst is exposed to acid and solvated; the SWNTs remain suspended.

A sonication step was performed between all steps. Smaller catalyst diameter and thinner carbon layers are beneficial for the method. No records of characteristic measurements, yield or purity are given.

## B.2 Reduced diameter distribution of SWNTs by selective oxidation<sup>55</sup>

Both a chemical treatment in HNO<sub>3</sub> and oxidation in a reduced O<sub>2</sub> atmosphere lead to a selective burning of the narrower SWNTs in bulk samples and to a diameter distribution which is smaller by a factor two.

Reduced oxygen atmosphere

1. The sample is annealed in high vacuum ( $5 \times 10^{-6}$  mbar) at 873 K in a quartz tube to remove the remaining fullerene particles and amorphous carbon.
2. Into the same quartz tube, pure oxygen is fed with a partial pressure of  $1.5 - 5 \times 10^{-6}$  mbar, within a temperature range of 723 – 873 K. Total annealing time is 70 h. This step selectively burns SWNTs with smaller diameter.
3. The sample is annealed in high vacuum ( $1 \times 10^{-7}$  mbar) at 1023 K to remove the oxygen.

In this method there is still metal catalyst in the sample.

Chemical oxidation

1. The sample is annealed in high vacuum ( $5 \times 10^{-6}$  mbar) at 873 K to remove the remaining fullerene particles and amorphous carbon.
2. The material is then refluxed in 2 M HNO<sub>3</sub> for 43 h at room temperature. This selectively oxidises the narrower SWNTs and also removes the metal catalyst.
3. The solution is neutralised and filtrated 6 h using crossflow filtration.
4. The sample is annealed in high vacuum at 873 K for 0.5 h to remove the remaining solvent and acid.
5. The sample is annealed in high vacuum at 1073 K for 0.5 h to remove the remaining solvent and acid.

Regarding the metal content a purity of 99.9 % is reached.

The samples are checked with AAS (atomic absorption spectroscopy) and TEM pictures. This shows that the metal content in the samples is reduced from 31 wt% to 0.1 wt% and that the diameter distribution is narrowed. A narrower size distribution is created, with a larger average diameter.

### **B.3 Plasma etching for purification and controlled opening of aligned carbon nanotubes<sup>56</sup>**

For the usage of aligned MWNTs in FED display industry, a thin layer (ca. 0.1 – 0.5  $\mu\text{m}$ ) of amorphous carbon film has to be removed. Most of the techniques known are tedious, have low yields and damage the vertical alignment.

The unique layered structure of the amorphous carbon film formed on top of the aligned MWNTs, makes the radio frequency glow-discharge plasma etching<sup>139</sup> a good method for purification.

1. The substrate is exposed to a water-plasma under vapour pressure in the range of 0.3 – 0.5 Torr. (80 min)
2. The power needed for the plasma is supplied by a radio frequency of 250 kHz
3. The plasma leads to a high concentration of atomic oxygen.
4. This oxygen will controllably oxidise a thin carbon layer on top of the vertically aligned tubes.
5. As a result purified aligned one-end opened nanotubes are obtained.

The result is confirmed by SEM and TEM images, which clearly show that the end-caps with the metal catalyst have been removed.

### **B.4 Purification and characterisation of SWNTs<sup>57</sup>**

This method has been developed for the removal of metal catalyst and carbon impurities from the laser grown SWNTs and initially cleaned with nitric acid. It describes two studies of a relatively high temperature gas phase oxidation process.

The first study:

1. Water reflux for removing aromatic carboxyl acids produced by the cleaning with nitric acid.
2. The sample was heated in a 5 % O<sub>2</sub>/Ar, 1 atm mixture for 1 h. The temperature was varied from 300 – 500 °C in four steps.
3. After each heating step, a sonication in concentrated HCl followed
4. Best steps were the oxidations at 300 and 500 °C.

The second study was done with a two-step oxidation to produce the best results for metal removal with minimum loss of nanotubes:

1. Water reflux for removing aromatic carboxyl acids produced by the cleaning with nitric acid.
2. The sample was heated at 300 °C in a 5 % O<sub>2</sub>/Ar, 1 atm mixture for 1 h.
3. After this heating step a sonication in concentrated HCl was performed.
4. The sample was heated at 500 °C in a 5 % O<sub>2</sub>/Ar, 1 atm mixture for 1 h.
5. Another sonication step in concentrated HCl.
6. The final metal content in 0.1 % relative to the carbon content. The last step, the oxidation is metal catalysed.
7. Finally, annealing at 900 °C follows.

The samples were checked with SEM and TEM images. TGA indicated that the samples that were heated showed the best temperature resistance. Also the effect of more metals was checked with TGA. From the Raman spectra, it can be seen that the annealing step increased the intensity of the SWNT

peak. Looking at the van Hove peaks gained with *UV-vis-near-IR*, it can be concluded that this oxidation removes smaller diameter SWNT preferentially. Also the intensities of the van Hove peaks increased.

## B.5 Purification of SWNTs by selective microwave heating of catalyst particles<sup>58</sup>

Steps:

1. *Microwave treatment at 500 °C for 20 min.*  
The sample (100 mg of arc-discharge SWNTs) was placed in a quartz tube that passed through a cavity. The microwaves couple to the residual metal catalyst, raising significantly the local temperature, leading to both the oxidation and rupturing of the carbon passivation layer over the catalyst particles.
2. *Mild acid treatment*  
With this protective carbon coating weakened or removed, a mild acid treatment (4 M HCl reflux for 6 h) is then sufficient to remove most of the metal in the sample, leaving the nanotubes in tact.

*Optimal conditions:*

*Flow (dry air) = 100 sccm*  
*Frequency = 2,45 GHz*  
*Power = 150 W*  
*Temperature = 500 °C*

The entire process was monitored by *TEM* and *HRTEM* pictures. *TGA* showed that a apparent three differential peak structure was obtained, which indicated that the metal catalyst partially oxidised the tubes, to form amorphous carbon and multi shell carbons. *Raman* spectrometry indicated that the microwave process gave a small broadening of the SWNT peak, the HCl treatment hardly damaged the SWNT and the HNO<sub>3</sub> reflux step gave a significant peak broadening.

Using microwave processing and a mild acid treatment it is possible to remove residual metal to a level lower than 0,2 wt%. The total yield for the two-step purification procedure is about 35 wt%.

## B.6 Length sorting cut SWNTs by high performance liquid chromatography<sup>59</sup>

Previously cut SWNTs by an acid base process are sorted by length by HPLC based, size exclusion chromatography (SEC). The SWNTs were grown by pulsed laser vaporisation.

Purifying and cutting SWNTs

1. Wet oxidation with reflux in HNO<sub>3</sub>
2. Crossflow filtration
3. First cutting was affected by 24 h ultrasonication in a 3:1 mixture of HNO<sub>3</sub>:H<sub>2</sub>SO<sub>4</sub> at 45 °C.
4. Next to further shorten the tubes and to consume sidewall defects, the SWNT reacted in a 4:1 mixture of H<sub>2</sub>SO<sub>4</sub>:H<sub>2</sub>O<sub>2</sub> for 10 min.

HPLC

1. The cut SWNTs are run over a SEC-HPLC.
2. The biggest SWNTs leave the HPLC first (after ± 20 min).
3. At the end, when all the SWNTs have already past, the C<sub>60</sub>, C<sub>70</sub> etc, come out (after ± 30 min).

The results above could be concluded from *AFM* (atomic force microscopy) pictures and the *UV-vis* measurements from the HPLC.

## B.7 Purification of SWNTs synthesised by the hydrogen arc-discharge method<sup>60</sup>

SWNTs synthesised with the hydrogen arc-discharge method have been purified with ultrasonication in alcohol, oxidation in fixed air and soaking in hydrochloric acid. The yield of the method is ~ 41% of the as-produced soot which contained ~55% SWNTs. The obtained purity is 96%.

1. Ultrasonication in alcohol for 30 min to cleave off impurities from the SWNTs.
2. Dried to air at room temperature.
3. The sample is oxidised in fixed air at 540-550 °C for 40 min, which oxidises the carbon impurities.
4. The product is then soaked in hydrochloric acid.
5. Afterwards, the sample is washed with de-ionised water and dried in an oven at 150 °C.

The *TEM* pictures showed that almost no visible impurities remained in the sample. This was confirmed by *TGA* (thermo graphic analysis), which included *TG* (thermogravimetry), *DTG* (differential thermogravimetry) and *DTA* (differential thermal analysis). *Raman* spectrometry showed the removal of the carbon impurities peak and sharpening of the SWNT-peak.

Further is stated that the carbon impurities start to combust at 528 °C and the SWNTs start to combust at 600 °C. This is why a temperature of 550 °C is chosen.

## B.8 High-quality SWNTs from arc-produced soot<sup>61</sup>

A three-step process, for purifying the raw soot, which contained 33 % metal and 67 % carbon.

Steps:

1. *Soft oxidation.* The as-produced soot (150 mg) was subjected to 120 °C reflux in a 2,8 N  $\text{HNO}_3$  solution (200 ml) for 6, 12 or 24 hours. The solution was filtered and washed with distilled water several times, followed by drying at 100 °C for more than 10 hours. In this first step an oxide layer was formed on the surface of the metal catalyst and damage to the amorphous carbon occurred.
2. *Air oxidation.* The dried sample was heated in air at 550 °C for ten min to remove the amorphous carbon.
3. *High-temperature vacuum treatment.* The sample was heat-treated at 1600 °C at a pressure of  $10^{-3}$  Pa for three hours. In this final step the graphitic carbon and metals are removed, the oxide layer decomposes and the rearrangement of SWNT walls occurred.

After the final step, about 20 % of the weight of the initial raw soot remained and the final product contained less than 1 % metal.

*TEM* images are analysed. *TGA* samples of the different steps have been made, which show the loss in metal and carbon. *Raman* spectra give information on the diameter size (RBM peaks) and the SWNT content (*G/D* values) by comparing peaks.

## B.9 High-yield purification process of SWNTs<sup>62</sup>

A two step process for the purification of as-produced SWNTs from the catalytic arc discharge process (Ni/Co/FeS=1:1:1). The process involves rotating thermal oxidation in air and an acid treatment.

1. The as-produced SWNTs were grinded and heated at 470°C for 50 min while rotated at 30 rpm. This step removes the carbonaceous particles, weight was reduced to 40 wt% of the initial sample.
2. The oxidised powder was immersed and filtered in 6 M HCl to dissolve the metal catalyst. The yield was 70 wt%.
3. To unbundle the SWNTs, the sample was refluxed in 30 %  $\text{HNO}_3$  for 4-6 hours.

4. The obtained suspension was filtered with a PTFE (poly-(tetrafluoroethylene)) membrane in de-ionised water.

The final yield was 25-30 wt% with a purity of ~ 96 %, containing 1 % metal atoms (initially 8%).

*SEM* and *TEM* images, *Raman* spectra and *TGA* of the process samples were taken. The *Raman* spectra clearly show that the samples purity and defects content are improved by the various processes. The ratio of the peaks at 1600  $\text{cm}^{-1}$  and 1300  $\text{cm}^{-1}$  increases.

## **B.10 Purification and characterisation of SWNTs obtained from the gas-phase decomposition of CO (HiPco process)<sup>63</sup>**

Steps:

1. Raw HiPco tubes compressed onto a dry filter paper (vacuum).
2. SWNTs are placed in a quartz tube furnace.
3. Mixture of  $\text{O}_2$  in Ar is passed through a water bubbler and run over the sample.
4. Nanotubes and a continuous flow of wet Ar and  $\text{O}_2$  are heated at 225 °C for 18 h. This heating step oxidises the metal. This metaloxide has a lower density, which causes the carbon shells to break open and exposes the metal. This could also be done at 325 °C (1,5 h) or 425 °C (1 h).
5. Sonication (15 min.) or prolonged stirring in concentrated HCl solution (overnight).
6. Filtered onto a 47 mm (1  $\mu\text{m}$  pore size) Teflon membrane.
7. Washed several times with de-ionised water and methanol
8. Dried in a vacuum oven at 100 °C (minimum of 2 h).
9. Annealing at 800 °C in Ar for 1 h.

From the *TGA* measurements it can be seen that the samples first gain weight, because of oxidation of the metal and then loose weight because of the (catalysed) carbon removal. *UV-vis-near-IR* indicate the preferential loss of smaller diameter during the cleaning process and give insight in the van Hove features during the process. With *Raman* spectra the loss of intensity due to the process and recovery due to annealing is shown. *SEM* en *TEM* images show the raw and the purified SWNTs. A large reduction of impurities can be seen. Also a comparison is made with laser-grown SWNTs by comparing the *UV-vis-near-IR* and *Raman* spectra.

The reference shows the different outcomes for the different temperatures. This method oxidises the metal and the carbon impurities. SWNTs with smaller diameters are oxidised preferentially.

## **B.11 Ultrasonic reflux system for one-step purification of carbon nanostructures<sup>64</sup>**

Patent for one-step purification of SWNTs. Soot containing amorphous carbon, metal catalyst and carbon nanostructures is purified in one system.

First step:

1. Sonication, to solve soot in the first flask.
2. Solvated soot is run over a filtering membrane and removed from the sonication area, non-solvated soot remains in flask.

Second step:

3. Solvated soot is further purified in second flask with a reflux column.
4. Oxidising gas is inserted to oxidise the amorphous carbon.
5. In the second flask acid removes metal catalyst.

No records of characteristic measurements, yield or purity are given.

## B.12 Purification of SWNTs by microfiltration<sup>65</sup>

This technique allows us to separate the as-prepared SWNT mats into three separate fractions without the use of acid, heat, or oxidative treatment.

Steps:

1. The sample (SWNTs prepared by pulsed laser ablation) is soaked into CS<sub>2</sub>.
2. The CS<sub>2</sub> insolubles are then trapped in a filter.
3. Sonication of the insoluble solids in aqueous solution (0,1 % surfactant).
4. Micro filtration. Most of the carbon nano spheres (CNS, C<sub>60</sub> and C<sub>70</sub>) and metal nanoparticles are passing through the filter, while the SWNTs and a small amount of residual CNS and metal nanoparticles are trapped. The microfiltration process is repeated for three cycles to minimise the amount of residual CNS and metal nanoparticles trapped between the ropes of the SWNTs.

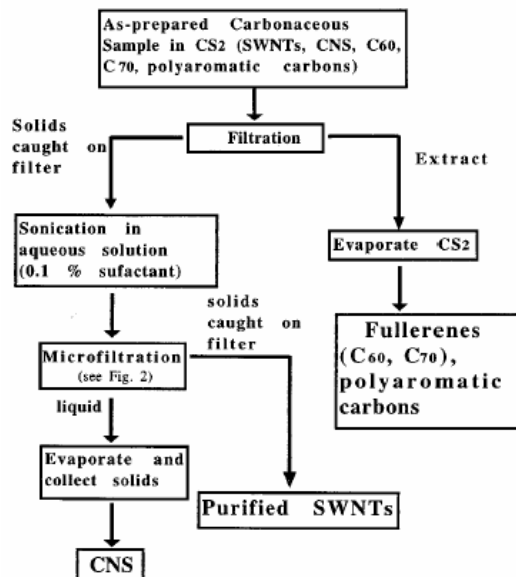


Figure 7-8: Scheme of the purification process.<sup>65</sup>

HRSEM and TEM pictures gave proof of that what is stated above. The Raman spectra of the CS<sub>2</sub> extracts, the as-produced and the purified SWNTs show that C<sub>60</sub> and C<sub>70</sub> are removed.

The individual weight percentages of the separated fractions are 6, 10 and 84 wt% for the CS<sub>2</sub> extract, CNS and SWNTs respectively.

## B.13 Purification of HiPco carbon nanotubes via organic functionalisation<sup>66</sup>

Steps

1. Organic functionalisation of the as-produced nanotubes (p-SWNTs) based on 1,3-dipolar cycloaddition of azomethine ylides in DMF suspension.
2. Purification of the soluble functionalised nanotubes (f-SWNTs). The purification is based on the improved solubility of the nanotubes and the insolubility of the metal particles. To further purify f-SWNTs, basically removing the amorphous carbon particles, a slow precipitation process is employed, occurring when diethyl ether is added to a chloroform solution of f-SWNTs (85 mg in 300 ml).

3. Removal of the functional groups and recovery of the purified nanotubes (r-SWNTs) by thermal treatment at 350 °C, followed by annealing to 900 °C.
4. The metal content was reduced from 26 % to 0.4 %.

*TEM* images of the purified and as-produced nanotubes were taken. *DSC* (differential scanning calorimetry) showed that the purification process had few impact on the structure of the SWNTs, as the curves were almost the same. The *DSC* curve of the f-SWNTs were quite different. *NIR* (near-infrared) showed that functionalisation altered the electronic properties of the tubes. Further could be seen that some peaks after purification became less intense, due to the fact that more SWNTs with smaller diameter were oxidised. The same result was found with *Raman*. From the *AAS* measurement could be seen that the metal content was reduced from 26 % to 0.4 %.

## B.14 Purification of SWNTs by ultrasonically assisted filtration<sup>67</sup>

This process generates material with a purity of more than 90% and yields of 30-70%. Ultrasonically assisted filtration technique allowed us to purify up to 150 mg SWNT soot in 3-6 h.

Steps

1. The soot was suspended in toluene and the suspension was filtered to extract soluble fullerenes. The toluene-insoluble fraction was then re-suspended in methanol. A typical concentration of the raw material in the suspension was 1 g/l.
2. The suspension was then transferred into a 47 filtration funnel. A 25,4 mm ultrasonic horn was inserted into the funnel and was placed about 1 cm above the surface of the filter membrane.
  - *Pore size membrane: 0,8 μm*
  - *Amplitude horn tip vibrations: 33μm*
  - *Power diss. by horn: 12 W/cm<sup>2</sup>*
  - *Temperature funnel: 0 °C*
  - *Pressure: 50 Torr*

Ultrasonication applied to the samples during filtration maintains the material in suspension. It also prevents formation of a cake of the material on the filter surface. Methanol was continuously added to the filtration funnel to maintain a constant filtration volume.

3. After filtration, the material was washed with 6 M sulphuric acid to remove traces of metal, introduced into the sample by the ultrasonic horn.

*TEM* and *SEM* images of the purified samples have been made. Next to that they were characterised by *Raman* spectroscopy. The method substantially decreased the amorphous carbon peak. *TGA* showed that the purified SWNTs had more defects. The 50 % oxidation point is reached 30 °C earlier as for purification.

## B.15 Mechanical purification of SWNT bundles from catalytic particles<sup>68</sup>

The basic principle of the purification method is like a snooker game, where we use the energy of elastic impact between encapsulated catalysts and small hard inorganic particles to eject the metal kernels and trap them with a strong magnet.

Steps:

1. SWNTs are first suspended either in soap solution or in toluene and then are dispersed in various solvents such as toluene, N,N-dimethylformamide or 30 % nitric acid.
2. A powder of nanoparticles (ZrO<sub>2</sub>, NH<sub>4</sub>Cl, CaCO<sub>3</sub> or diamond), that is not soluble in the given medium, was then added to the suspension. This slurry was sonicated typically for 24 hours. The ultrasonic bath mechanically removes the ferromagnetic particles from their graphitic shells.

3. The magnetic particles are trapped with permanent magnetic poles and with a subsequent chemical treatment A high purity SWNT material is obtained.

The samples were checked with *ESR* (electron spin resonance) and *TEM* images, which proved that the main part of the metal catalyst was removed. This method is typically developed for lab-sized purifications.

### **B.16 Cutting SWNTs by fluorination<sup>69</sup>**

This process describes the fluorination of purified HiPco SWNTs (~1.0 nm, no amorphous carbon, no metal), followed by pyrolysis of the partially fluorinated tubes ( $CF_x$ ,  $x < 0.2$ ). This gives short tubes with average lengths of  $< 50$  nm. The initial length was ~1  $\mu$ m.

1. Purified SWNTs are fluorinated for 2 hours to a stoichiometry of  $CF_x$ , ( $x < 0.2$ ).
2. The partially fluorinated SWNTs are pyrolysed up to 1000 °C (TGA control, 10 C/min) in an argon atmosphere.
3. In this step the fluorine is driven off the sidewall of the tubes to form  $CF_4$  or  $COF_2$ .
4. This leaves behind chemically cut SWNTs in a yield of 55 %, with average lengths of ~ 40 nm. The yield is based on the amount of SWNTs.

The length of the tubes was measured by *AFM* imaging. *TGA*, *elemental analysis* and *IR* show that during pyrolysis the fluorine is completely driven off the nanotube. The elements that appear due to pyrolysis are also shown in a derivative weight percentage. *Raman* spectra of the purified, fluorinated and cut SWNTs indicate that the defects in the carbonaceous species increase.

### **B.17 Enhanced saturation lithium composition in ball-milled single-walled carbon nanotubes<sup>70</sup>**

The nanotubes are grinded for several minutes up to 20 min, what will induce breaking and disordering the carbon nanotubes. This process is highly time dependent, as longer ball-milling will eventually tear down all the SWNT structures.

The results of ball-milling have been monitored with *TEM* and *SEM* images and with *Raman* spectra. The tubes are shortened and *Raman* spectra indicate that more disordered carbon is produced.

### **B.18 Chromatographic purification of soluble SWNTs<sup>71</sup>**

SWNTs (1.4 nm and lengths of 100 – 300 nm) produced by arc-discharge, after several purification steps, are dissolved and run over a gel permeation chromatographic column:

1. Short SWNTs are functionalised with octadecylamine and solvated in THF.
2. The solution is run over a gel permeation chromatographic column, styragel HMW7.
3. Two main fractions are obtained.
4. The first fraction gives semi-conducting SWNTs.
5. The second fraction does not contain SWNTs, but contains nanoparticles and amorphous carbon.

*AFM* images have been made of the different fractions. The three HPLC fractions were analysed with continuous *UV-vis* measuring and a complete spectrum of each fraction was made. *NIR* spectra suggest that fraction 1 hardly contains metallic tubes. The yield was estimated with *NIR*. The *Raman spectra*, *AFM* and *NIR* show the purity of the fractions.

This method claims to separate and purify semi-conducting and metallic SWNTs. Finally, an estimate of 50% of the initial amount of SWNTs in the soot is recovered, with a high purity.

## B.19 Chromatographic purification and properties of soluble SWNTs<sup>72</sup>

SWNTs (1.4 nm and lengths of 100 – 300 nm) produced by arc-discharge, after several purification steps, are dissolved and are run over a gel permeation chromatographic column:

1. Short SWNTs are functionalised with octadecylamine and solvated in THF.
2. The solution is run over a gel permeation chromatographic column, PLgel MIXED-A.
3. Three main fractions have been obtained.
4. The first fraction gives semi-conducting SWNTs.
5. The second fraction gives traces of SWNTs and nanoparticles.
6. The third fraction gives amorphous carbon.

*AFM* images were made from the different fractions. The three fractions were seen with continuous *UV-vis* measuring and a complete spectrum of each fraction was made. The yield was estimated with *NIR*. The *Raman spectra*, *AFM* and *NIR* show the purity of the fractions. The *fluorescence* en *NIR* spectra suggest that fraction 1 hardly contains metallic tubes.

This method also claims to separate and purify semi- and metal-conducting SWNTs. The estimated yield is a lot higher than with the technique above. This one recovers 74 % of the initial amount of SWNTs in the soot with high purity.

## Reference List

1. D.A.Bochvar and E.G.Gal'pern, Dokl.Akad.Nauk.USSR, **209**, (610, 1973
2. I.V.Stankevich, M.V.Nikerov, and D.A.Bochvar, Russ.Chem.Rev., **53**, (640, 1984
3. H.W.Kroto, J.R.Heath, S.C.O'Brien, R.F.Curl, and R.E.Smalley, Nature, **318**, (162, 1985
4. Iijima, Sumio, Nature (London, United Kingdom), 354, (6348), 1991
5. Dresselhaus, M. S., Dresselhaus, G., and Eklund, P. C., 1996
6. Ajayan, P. M. and Ebbesen, T. W., Rep.Prog.Phys., **60**, (1025-1065, 2003
7. Niyogi, S., Hamon, M. A., Hu, H., Zhao, B., Bhowmik, P., Sen, R., Itkis, M. E., and Haddon, R. C., Accounts of Chemical Research, 35, (12), 2002
8. Avouris, P., Chemical Physics, **281**, (2-3), 429-445, 2002
9. Tans, Sander J., Devoret, Michel H., Dal, Hongjie, Thess, Andreas, Smalley, Richard E., Geerligs, L. J., and Dekker, Cees, Nature (London), 386, (6624), 1997
10. Ajayan, P. M. and Zhou, O. Z., Carbon Nanotubes, **80**, (391-425, 2001
11. Damnjanovic, M., Milosevic, I., Vukovic, T., and Sredanovic, R., Physical Review B, **60**, (4), 2728-2739, 1999
12. Yasuda, Ayumu, Kawase, Noboru, and Mizutani, Wataru, Journal of Physical Chemistry B, 106, (51), 2002
13. Sinnott, S. B., Andrews, R., Qian, D., Rao, A. M., Mao, Z., Dickey, E. C., and Derbyshire, F., Chem.Phys.Lett., **315**, (25-30, 1999
14. Jung, S. H., Kim, M. R., Jeong, S. H., Kim, S. U., Lee, O. J., Lee, K. H., Suh, J. H., and Park, C. K., Applied Physics A-Materials Science & Processing, **76**, (2), 285-286, 2003
15. Ebbesen, T. W. and Ajayan, P. M., Nature, **358**, (220-222, 1992
16. Journet, C. and Bernier, P., Applied Physics A-Materials Science & Processing, **67**, (1), 1-9, 1998
17. Farhat, S., La Chapelle, M. L., Loiseau, A., Scott, C. D., Lefrant, S., Journet, C., and Bernier, P., Journal of Chemical Physics, **115**, (14), 6752-6759, 2001
18. Farhat, S., Hinkov, I., Chapelle, D. I., Fan, S. S., Li, G. H., and Scott, C. D., NASA Conference Publication, 2001
19. Costa, Pedro, Xu, Cigang, Coleman, Karl, Sloan, Jeremy, and Green, Malcolm L H, 2002
20. Huang, H. J., Marie, J., Kajiura, H., and Ata, M., Nano Letters, **2**, (10), 1117-1119, 2002
21. Takikawa, Hirofumi, Tao, Yoshitaka, Hibi, Yoshihiko, Miyano, Ryuichi, Sakakibara, Tateki, Ando, Yoshinori, Ito, Shigeo, Hirahara, Kaori, and Iijima, Sumio, AIP Conference Proceedings, 590, (Nanonetwork Materials), 2001
22. Takikawa, H., Ikeda, M., Hirahara, K., Hibi, Y., Tao, Y., Ruiz, P. A., Sakakibara, T., Itoh, S., and Iijima, S., Physica B: Condensed Matter (Amsterdam, Netherlands), 323, (1-4), 2002
23. Anazawa, Kazunori, Shimotani, Kei, Manabe, Chikara, Watanabe, Hiroyuki, and Shimizu, Masaaki, Applied Physics Letters, 81, (4), 2002
24. Lee, Seung Jong, Baik, Hong Koo, Yoo, Jae eun, and Han, Jong hoon, Diamond and Related Materials, 11, (3-6), 2002
25. Guo, T., Nikolaev, P., Thess, A., Colbert, D. T., and Smalley, R. E., Chemical Physics Letters, 243, (1,2), 1995
26. Yudasaka, M., Yamada, R., Sensui, N., Wilkins, T., Ichihashi, T., and Iijima, S., Journal of Physical Chemistry B, 103, (30), 1999
27. Eklund, P. C., Pradhan, B. K., Kim, U. J., Xiong, Q., Fischer, J. E., Friedman, A. D., Holloway, B. C., Jordan, K., and Smith, M. W., Nano Letters, 2, (6), 2002
28. Maser, W. K., Munoz, E., Benito, A. M., Martinez, M. T., de la Fuente, G. F., Maniette, Y., Anglaret, E., and Sauvajol, J. L., Chemical Physics Letters, 292, (4,5,6), 1998
29. Bolshakov, A. P., Uglov, S. A., Saveliev, A. V., Konov, V. I., Gorbunov, A. A., Pompe, W., and Graff, A., Diamond and Related Materials, 11, (3-6), 2002
30. Scott, C. D., Arepalli, S., Nikolaev, P., and Smalley, R. E., Applied Physics A: Materials Science & Processing, 72, (5), 2001
31. Ren, Z. F., Huang, Z. P., Xu, J. W., Wang, J. H., Bush, P., Siegel, M. P., and Provencio, P. N., Science (Washington, D.C.), 282, (5391), 1998
32. Ren, Z. F., Huang, Z. P., Wang, D. Z., Wen, J. G., Xu, J. W., Wang, J. H., Calvet, L. E., Chen, J., Klemic, J. F., and Reed, M. A., Applied Physics Letters, 75, (8), 1999
33. Yudasaka, Masako, Kikuchi, Rie, Matsui, Takeo, Ohki, Yoshimasa, Yoshimura, Susumu, and Ota, Etsuro, Applied Physics Letters, 67, (17), 1995

34. Yudasaka, Masako, Kikuchi, Rie, Ohki, Yoshimasa, Ota, Etsuro, and Yoshimura, Susumu, *Applied Physics Letters*, **70**, (14), 1997
35. Chen, M., Chen, C. M., and Chen, C. F., *Journal of Materials Science*, **37**, (17), 3561-3567, 2002
36. Huang, Z. P., Wang, D. Z., Wen, J. G., Sennett, M., Gibson, H., and Ren, Z. F., *Applied Physics A-Materials Science & Processing*, **74**, (3), 387-391, 2002
37. Park, J. B., Choi, G. S., Cho, Y. S., Hong, S. Y., Kim, D., Choi, S. Y., Lee, J. H., and Cho, K. I., *Journal of Crystal Growth*, **244**, (2), 211-217, 2002
38. Maruyama, S., Chiashi, S., and Miyauchi, Y., *Thermal Engineering Joint Conference*, **6**, (2003)
39. Lee, Cheol Jin, Lyu, Seung Chul, Kim, Hyoun Woo, Park, Chong Yun, and Yang, Cheol Woong, *Chemical Physics Letters*, **359**, (1,2), 2002
40. Ge, M. and Sattler, K., *Applied Physics Letters*, **64**, (6), 710-711, 1994
41. Su, M., Zheng, B., and Liu, J., *Chemical Physics Letters*, **322**, (5), 2000
42. Zheng, B., Li, Y., and Liu, J., *Applied Physics A: Materials Science & Processing*, **74**, (3), 2002
43. Alexandrescu, R., Crunteanu, A., Morjan, R. E., Morjan, I., Rohmund, F., Falk, L. K. L., Ledoux, G., and Huisken, F., *Infrared Physics & Technology*, **44**, (1), 2003
44. <http://www.ou.edu/engineering/nanotube>, 2003
45. Herrera, J., Balzano, L., Pompeo, F., and Resasco, D., [http://www.cmp-cientifica.com/cientifica/frameworks/generic/public\\_users/TNT02/files/Abstract\\_Herrera.pdf](http://www.cmp-cientifica.com/cientifica/frameworks/generic/public_users/TNT02/files/Abstract_Herrera.pdf), 2003
46. <http://www.ou.edu/engineering/nanotube/NT2001Production.PDF>, 2003
47. Nikolaev, Pavel, Bronikowski, Michael J., Bradley, R. Kelley, Rohmund, Frank, Colbert, Daniel T., Smith, K. A., and Smalley, Richard E., *Chemical Physics Letters*, **313**, (1,2), 1999
48. Smalley, Richard E. and Yakobson, Boris I., *Solid State Communications*, **107**, (11), 1998
49. Bronikowski, Michael J., Willis, Peter A., Colbert, Daniel T., Smith, K. A., and Smalley, Richard E., *Journal of Vacuum Science & Technology, A: Vacuum, Surfaces, and Films*, **19**, (4, Pt. 2), 2001
50. Vander Wal, Randall L., Hall, Lee J., and Berger, Gordon M., *Journal of Physical Chemistry B*, **106**, (51), 2002
51. Vander Wal, Randall L. and Ticich, Thomas M., *Journal of Physical Chemistry B*, **105**, (42), 2001
52. Wal, R. L. V., Berger, G. M., and Hall, L. J., *Journal of Physical Chemistry B*, **106**, (14), 3564-3567, 2002
53. Endo, Morinobu, Takeuchi, Kenji, Igarashi, Susumu, Kobori, Kiyoharu, Shiraishi, Minoru, and Kroto, Harold W., *Journal of Physics and Chemistry of Solids*, **54**, (12), 1993
54. Goto, Hajime, Furuta, Terumi, Fujiwara, Yoshiya, and Ohashi, Toshiyuki., 2002-166386, (2003007924),
55. Borowiak-Palen, E., Pichler, T., Liu, X., Knupfer, M., Graff, A., Jost, O., Pompe, W., Kalenczuk, R. J., and Fink, J., *Chemical Physics Letters*, **363**, (5-6), 567-572, 2002
56. Huang, S. M. and Dai, L. M., *Journal of Physical Chemistry B*, **106**, (14), 3543-3545, 2002
57. Chiang, I. W., Brinson, B. E., Smalley, R. E., Margrave, J. L., and Hauge, R. H., *Journal of Physical Chemistry B*, **105**, (6), 1157-1161, 2001
58. Harutyunyan, A. R., Pradhan, B. K., Chang, J. P., Chen, G. G., and Eklund, P. C., *Journal of Physical Chemistry B*, **106**, (34), 8671-8675, 2002
59. Farkas, E., Anderson, M. E., Chen, Z. H., and Rinzler, A. G., *Chemical Physics Letters*, **363**, (1-2), 111-116, 2002
60. Hou, Peng Xiang, Liu, C., Tong, Y, Liu, M., and Cheng, H. M., *Journal of Materials Research*, **16**, (9), 2526-2529, 2001
61. Kajiura, H., Tsutsui, S., Huang, H. J., and Murakami, Y., *Chemical Physics Letters*, **364**, (5-6), 586-592, 2002
62. Moon, J. M., An, K. H., Lee, Y. H., Park, Y. S., Bae, D. J., and Park, G. S., *Journal of Physical Chemistry B*, **105**, (24), 5677-5681, 2001
63. Chiang, I. W., Brinson, B. E., Huang, A. Y., Willis, P. A., Bronikowski, M. J., Margrave, J. L., Smalley, R. E., and Hauge, R. H., *Journal of Physical Chemistry B*, **105**, (35), 8297-8301, 2001
64. Huang, Houjin, Shiraishi, Masashi, Yamada, Atsuo, Kajiura, Hisashi, and Ata, Masafumi., 2001-JP10713, (0245812),
65. Bando, Shunji, Rao, A. M., Williams, K. A., Thess, A., Smalley, R. E., and Eklund, P. C., *Journal of Physical Chemistry B*, **101**, (44), 1997
66. Georgakilas, Vasilios, Voulgaris, Dimitrios, Vazquez, Ester, Prato, Maurizio, Guldi, Dirk M., Kukovec, Akos, and Kuzmany, Hans, *Journal of the American Chemical Society*, **124**, (48), 2002
67. Shelimov, K. B., Esenaliev, R. O., Rinzler, A. G., Huffman, C. B., and Smalley, R. E., *Chem.Phys.Lett.*, **282**, (429-434), 1998
68. Thien-Nga, L., Hernadi, K., Ljubovic, E., Garaj, S., and Forro, L., *Nano Letters*, **2**, (12), 1349-1352, 2002

69. Gu, Z., Peng, H., Hauge, R. H., Smalley, R. E., and Margrave, J. L., *Nano Letters*, **2**, (9), 1009-1013, 2002
70. Gao, B., Bower, C., Lorentzen, J. D., Fleming, L., Kleinhammes, A., Tang, X. P., Mcneil, L. E., Wu, Y., and Zhou, O., *Chemical Physics Letters*, **327**, (1-2), 69-75, 2000
71. Niyogi, S., Hu, H., Hamon, M. A., Bhowmik, P., Zhao, B., Rozenzhak, S. M., Chen, J., Itkis, M. E., Meier, M. S., and Haddon, R. C., *Journal of the American Chemical Society*, **123**, (4), 733-734, 2001
72. Zhao, B., Hu, H., Niyogi, S., Itkis, M. E., Hamon, M. A., Bhowmik, P., Meier, M. S., and Haddon, R. C., *Journal of the American Chemical Society*, **123**, (47), 11673-11677, 2001
73. Baughman, R. H., Zakhidov, A. A., and de Heer, W. A., *Science*, **297**, (5582), 787-792, 2002
74. D.Rotman, *Natuur & Techniek*, **70**, (6), 30-37, 2002
75. Zuttel, A., Nutzenadel, C., Sudan, P., Mauron, P., Emmenegger, C., Rentsch, S., Schlapbach, L., Weidenkaff, A., and Kiyobayashi, T., *Journal of Alloys and Compounds*, **330**, (676-682), 2002
76. Lee, S. M., Park, K. S., Choi, Y. C., Park, Y. S., Bok, J. M., Bae, D. J., Nahm, K. S., Choi, Y. G., Yu, S. C., Kim, N. G., Frauenheim, T., and Lee, Y. H., *Synthetic Metals*, **113**, (3), 209-216, 2000
77. Zuttel, A., Sudan, P., Mauron, P., Kiyobayashi, T., Emmenegger, C., and Schlapbach, L., *International Journal of Hydrogen Energy*, **27**, (2), 203-212, 2002
78. Gao, X. P., Lan, Y., Pan, G. L., Wu, F., Qu, J. Q., Song, D. Y., and Shen, P. W., *Electrochemical and Solid State Letters*, **4**, (10), A173-A175, 2001
79. Qin, X., Gao, X. P., Liu, H., Yuan, H. T., Yan, D. Y., Gong, W. L., and Song, D. Y., *Electrochemical and Solid State Letters*, **3**, (12), 532-535, 2000
80. Rajalakshmi, N., Dhathathreyan, K. S., Govindaraj, A., and Satishkumar, B. C., *Electrochimica Acta*, **45**, (27), 4511-4515, 2000
81. Nutzenadel, C., Zuttel, A., Chartouni, D., and Schlapbach, L., *Electrochemical and Solid State Letters*, **2**, (1), 30-32, 1999
82. Dai, G. P., Liu, C., Liu, M., Wang, M. Z., and Cheng, H. M., *Nano Letters*, **2**, (5), 503-506, 2002
83. Kibria, A. K. M. F., Mo, Y. H., Park, K. S., Nahm, K. S., and Yun, M. H., *International Journal of Hydrogen Energy*, **26**, (8), 823-829, 2001
84. Frackowiak, E. and Beguin, F., *Carbon*, **40**, (10), 1775-1787, 2002
85. Froudakis, G. E., *Journal of Physics-Condensed Matter*, **14**, (17), R453-R465, 2002
86. Jeloica, L. and Sidis, V., *Chemical Physics Letters*, **300**, (1-2), 157-162, 1999
87. Cracknell, R. F., *Molecular Physics*, **100**, (13), 2079-2086, 2002
88. Froudakis, George E., *Nano Letters*, **1**, (4), 2001
89. Yang, F. H. and Yang, R. T., *Carbon*, **40**, (3), 437-444, 2002
90. Bauschlicher, Charles W., Jr., *Nano Letters*, **1**, (5), 2001
91. Lee, H. H., Wan, C. C., and Wang, Y. Y., *Journal of Power Sources*, **Article in press**, (1-7), 2003
92. Gao, B., Kleinhammes, A., Tang, X. P., Bower, C., Fleming, L., Wu, Y., and Zhou, O., *Chemical Physics Letters*, **307**, (3-4), 153-157, 1999
93. Fischer, J. E., *Chemical Innovation*, **30**, (10), 21-27, 2000
94. Yang, Z. and Wu, H., *Materials Chemistry and Physics*, **71**, (1), 2001
95. Shimoda, H., Gao, B., Tang, X. P., Kleinhammes, A., Fleming, L., Wu, Y., and Zhou, O., *Physical Review Letters*, **8801**, (1), art-015502, 2002
96. Shin, H. C., Liu, M. L., Sadanadan, B., and Rao, A. M., *Journal of Power Sources*, **112**, (1), 216-221, 2002
97. Dubot, P. and Cenedese, P., *Physical Review B*, **6324**, (24), art-241402, 2001
98. Kar, T., Pattanayak, J., and Scheiner, S., *Journal of Physical Chemistry A*, **105**, (45), 10397-10403, 2001
99. Dillon, A. C., Gilbet, K. E. H., Parilla, P. A., Alleman, J. L., Hornyak, G. L., Jones, K. M., and Heben, M. J., *C0 80401-3393*, 2002
100. Hirscher, M., Becher, M., Haluska, M., Quintel, A., Skakalova, V., Choi, Y. M., Dettlaff-Weglikowska, U., Roth, S., Stepanek, I., Bernier, P., Leonhardt, A., and Fink, J., *Journal of Alloys and Compounds*, **330**, (654-658), 2002
101. Atkinson, K., Roth, S., Hirsher, M., and Grunwald, W., *Fuel Cells Bulletin*, **38**, 9-12, 2002
102. Liu, C., Fan, Y. Y., Liu, M., Cong, H. T., Cheng, H. M., and Dresselhaus, M. S., *Science*, **286**, (5442), 1127-1129, 1999
103. Dodziuk, H. and Dolgonos, G., *Chemical Physics Letters*, **356**, (1-2), 79-83, 2002
104. Rzepka, M., Lamp, P., and Casa-Lillo, M. A., *Journal of Physical Chemistry B*, **102**, (52), 1998
105. Levesque, D., Gicquel, A., Darkrim, F. L., and Kayiran, S. B., *Journal of Physics-Condensed Matter*, **14**, (40), 9285-9293, 2002
106. Silvera, Isaac F. and Goldman, Victor V., *Journal of Chemical Physics*, **69**, (9), 1978
107. Wang, Qinyu and Johnson, J. Karl, *Journal of Chemical Physics*, **110**, (1), 1999

108. Darkrim, F. L., Malbrunot, P., and Tartaglia, G. P., *International Journal of Hydrogen Energy*, **27**, (2), 193-202, 2002
109. Williams, K. A. and Eklund, P. C., *Chemical Physics Letters*, **320**, (3-4), 352-358, 2000
110. Cheng, H. M., Yang, Q. H., and Liu, C., *Carbon*, **39**, (10), 1447-1454, 2001
111. An, K. H., Kim, W. S., Park, Y. S., Choi, Y. C., Lee, S. M., Chung, D. C., Bae, D. J., Lim, S. C., and Lee, Y. H., *Journal of Korean Physical Society*, **39**, (511-517), 2001
112. Frackowiak, E. and Beguin, F., *Carbon*, **39**, (6), 937-950, 2001
113. Bockris, John M., Reddy, Amalya K. N., and Gamboa-Aldeco, Maria, **2**, (7), 2000
114. Frackowiak, E., Jurewicz, K., Szostak, K., Delpeux, S., and Beguin, F., *Fuel Processing Technology*, **77**, (213-219), 2002
115. Frackowiak, E., Jurewicz, K., Delpeux, S., and Beguin, F., *Journal of Power Sources*, **97-8**, (822-825), 2001
116. Jurewicz, K., Delpeux, S., Bertagna, V., Beguin, F., and Frackowiak, E., *Chemical Physics Letters*, **347**, (1-3), 36-40, 2001
117. Frackowiak, E., Delpeux, S., Jurewicz, K., Szostak, K., Cazorla-Amoros, D., and Beguin, F., *Chemical Physics Letters*, **361**, (1-2), 35-41, 2002
118. Jiang, Q., Qu, M. Z., Zhou, G. M., Zhang, B. L., and Yu, Z. L., *Materials Letters*, **57**, (4), 988-991, 2002
119. Jorio, A., Hafner, J. H., Lieber, C. M., Hunter, M., McClure, T., Dresselhaus, G., and Dresselhaus, M. S., *Physical Review Letters*, **86**, (6), 1118-1121, 2001
120. Williams, P. A., Papadakis, S. J., Falvo, M. R., Patel, A. M., Sinclair, M., Seeger, A., Helser, A., Taylor, R. M., Washburn, S., and Superfine, R., *Applied Physics Letters*, **80**, (14), 2574-2576, 2002
121. Qian, D., Wagner, G. J., and Liu, W. K., *Appl Mech Rev*, **55**, (6), 495-533, 2002
122. Ouyang, M., Huang, J. L., and Lieber, C. M., *Accounts of Chemical Research*, **35**, (12), 1018-1025, 2002
123. Dresselhaus, M. S., Dresselhaus, G., Jorio, A., Souza Filho, A. G., Pimenta, M. A., and Saito, R., *Accounts of Chemical Research*, **35**, (1070-1078), 2002
124. Bonard, J. M., Kind, H., Stockli, T., and Nilsson, L. A., *Solid-State Electronics*, **45**, (6), 893-914, 2001
125. Saito, Y. and Uemura, S., *Carbon*, **38**, (2), 169-182, 2000
126. Taur, Y and Ning, T. H., 1998
127. Avouris, Phaedon, *Accounts of Chemical Research*, **35**, (12), 2002
128. Tans, S. J., Verschueren, A. R. M., and Dekker, C., *Nature*, **393**, (6680), 49-52, 1998
129. Martel, R., Schmidt, T., Shea, H. R., Hertel, T., and Avouris, Ph, *Applied Physics Letters*, **73**, (17), 2447-2449, 1998
130. Wind, S. J., Appenzeller, J., Martel, R., Derycke, V., and Avouris, Ph, *Journal of Vacuum Science Technology B*, **20**, (6), 2798-2801, 2002
131. Mceuen, P. L., Bockrath, M., Cobden, D. H., Yoon, Y. G., and Louie, S. G., *Physical Review Letters*, **83**, (24), 5098-5101, 1999
132. Bockrath, M. and et.al., *Physical Review B*, R10606-R10608, 2000
133. Derycke, V., Martel, R., Appenzeller, J., and Avouris, Ph, *Applied Physics Letters*, **80**, (15), 2773-2775, 2002
134. Heinze, S., Tersoff, J., Martel, R., Derycke, V., Appenzeller, J., and Avouris, Ph, *Physical Review Letters*, **89**, (10), 106801-1-106801-4, 2002
135. Tucker, J. R., Wang, C., and Carney, P. S., *Applied Physics Letters*, **65**, (618), 1994
136. Guo, Jing, Goasguen, Sebastien, Lundstrom, Mark, and Datta, Supriyo, Unkown, **PACS numbers: 61.46.+w, 85.35.Kt, 71.24.+q, 73.40.Qv**, (2002)
137. Kong, J., Cao, J., Dai, H. J., and Anderson, E., *Applied Physics Letters*, **80**, (1), 73-75, 2002
138. Postma, H. W. C., Teepen, T., Yao, Z., Grifoni, M., and Dekker, C., *Science*, **293**, (5527), 76-79, 2001
139. Dai, Liming, Griesser, Hans J., and Mau, Albert W. H., *Journal of Physical Chemistry B*, **101**, (46), 1997